國立交通大學

電子工程學系 電子研究所

博士論文

自組式砷化銦量子點/環及其紅外線偵測器之研究

Studies of Self-assembled InAs Quantum Dots/Rings and their Infrared Photodetectors

研 究 生：凌鴻緒

指導教授：李建平 教授

共同指導：王祥宇 博士

中 華 民 國 九 十 八 年 三 月

自組式砷化銦量子點/環及其紅外線偵測器之研究

Studies of Self-assembled InAs Quantum Dots/Rings and their Infrared Photodetectors

研 究 生：凌鴻緒　　Student：Hong-Shi Ling

指導教授：李建平 博士　　Advisor：Dr. Chien-Ping Lee

王祥宇 博士　　Dr. Shiang-Yu Wang

國 立 交 通 大 學

電子工程學系 電子研究所

博 士 論 文

A Dissertation
Submitted to Department of Electronics Engineering and
Institute of Electronics
College of Electrical and Computer Engineering
National Chiao Tung University
in partial Fulfillment of the Requirements
for the Degree of
Doctor of Philosophy
in Electronics Engineering

March 2009
Hsinchu, Taiwan, Republic of China

中華民國九十八年三月

自組式砷化銦量子點/環及其紅外線偵測器之研究

學生：凌鴻緒　　　　指導教授：李建平博士

王祥宇博士

國立交通大學

電子工程學系電子研究所

摘要

本篇博士論文的目的是希望對自組式砷化銦量子點及量子環的磊晶及電子能態特性做一個通盤的瞭解，以便實現長波長量子結構紅外線偵測器並提升其元件特性。

我們研究如何利用分子束磊晶技術來控制砷化銦量子點的面密度及幾何形狀。藉由調變長晶條件及程序，我們已能成長大範圍之不同面密度的量子點，並且控制量子點的形狀變化以獲得其演變至量子環之各種不同形狀的量子結構。對於藉由部分覆蓋及熱退火技術所成長的量子環，我們也探討了造就其形變的機制。再者，透過模擬，我們發現量子環其環狀分佈的位能井迫使電子波函數遠離環心，以致於抬高了電子能階的分佈並縮小其能差。

我們也利用調變激發能量之螢光頻譜來研究量子點的能譜。分析量子點放射光譜隨激發能量改變的情形，我們區分出三個具有不同物理意義的特徵區域。隨激發能量由高至低，它們分別為：連續能態吸收區，離散電子態激發區，以及多聲子共振區。透過自組式量子點特有之沾濕層(wetting layer)與量子點耦合之準連續態，電子之釋能獲得幫助，上述豐富的能譜結果也得以解釋。

我們還研究藉由調變量子點能障結構的方式來調變量子點紅外線偵測器之偵測波段及極化吸收特性。此研究的結果顯示，透過量子點能障結構的設計，我們能有效操控量

子點偵測器之元件特性以符合不同的需求。由此觀念出發，我們設計了一種新的”侷限增強型量子點在井中(confinement-enhanced Dots-in-a-well, CE-DWELL)”之結構，有效加強了 DWELL 量子點本身在側向上較弱的能障侷限。利用這個新的設計，我們成功製作出高度正向吸收並具 8-12 微米波段之量子點紅外線偵測器。更重要的是，元件之量子效率及偵測度獲得大幅度的提升。

我們更進一步研究不同 CE-DWELL 結構之量子點紅外線偵測器。我們發現，用以增強侷限之砷化鋁鎵層的厚度及含鋁成分，對於偵測器元件不論是吸收特性或傳輸特性都有顯著的影響。調整適當之 CE-DWELL 元件參數，我們成功製作出操作溫度高於 200K 的 8-12 微米波段量子點紅外線偵測器。

最後，我們也研究了砷化銦量子環之紅外線偵測器。量子環在側向上較廣的波函數分佈與其較高卻較密的能階分佈造就了量子環偵測器不同於量子點偵測器的特色，例如：寬頻之光電流頻譜、隨溫度變化較為穩定之光響應度、較低之暗電流活化能。藉由一高能障砷化鋁鎵電流阻擋層，量子環本質上較低的載子活化能得以提升，量子環紅外線偵測器的操作溫度也因而提升。

Studies of Self-assembled InAs Quantum Dots/Rings and their Infrared Photodetectors

Student : Hong-Shi Ling Advisor : Dr. Chien-Ping Lee

Dr. Shiang-Yu Wang

Department of Electronics Engineering & Institute of Electronics
National Chiao Tung University

Abstract

The purpose of this dissertation is to get a comprehensive understanding of the epitaxy growth and electronic properties of the self-assembled InAs quantum dots (QDs) and quantum rings (QRs) to realize long-wavelength quantum structure infrared photodetectors with improved device characteristics.

The manipulation of the sheet density and geometry of InAs QDs via fully *in situ* molecular beam epitaxy growth control were investigated. A wide range of dot densities and the control over the geometric change from QDs, through volcano-shaped structures, to QRs, were achieved. The mechanism of such QR growth by the partial-capping & annealing technique was studied. Moreover, from simulation, it is found the ring-like potential well depletes the wavefunctions out of the ring center and thereby raises the state energies and also narrows the energy separations.

The energy spectra of QDs were investigated using the selective excitation photoluminescence technique. Three distinct regions in the emission spectra can be identified as associated with changes in the excitation energy. They can be categorized from high energy to low energy, as continuum absorption, electronic state excitation, and multi-phonon resonance.

The special joint density of state tail of the QD that extends from the wetting layer bandedge facilitates carrier relaxation and explains these spectral results.

InAs QDs with different confinement barrier schemes were used in quantum-dot infrared photodetectors (QDIPs) for the detection wavelength and polarization absorption tuning. The results show that one can effectively change the device characteristics of QDIPs to fit different application requirement by tailoring the QD confinement schemes. We design a new confinement-enhanced dots-in-a-well (CE-DWELL) structure to enhance the wavefunction confinement of QDs especially in the lateral direction. With this new design, QDIPs with 8-12 μm detection and high normal-incident absorption are achieved. More importantly, the device quantum efficiency and detectivity are greatly improved.

QDIPs with different CE-DWELL structures were further investigated. The thickness and Al content of the AlGaAs confinement enhancing layers are found of crucial influence on not only the absorption property but also the transport property of the device. With appropriate device parameters of CE-DWELL, we present 8-12 μm QDIPs with operation temperatures higher than 200K.

Finally, InAs quantum-ring infrared photodetectors (QRIPs) were also studied. The higher but closer electronic state energies as well as the extended wavefunctions of QRs in the lateral directions induce the specific features of QRIPs, such as wider photocurrent spectra, more stable responsivity with temperature change, and lower dark current activation energy. With an $Al_{0.27}Ga_{0.73}As$ current blocking layer, the inherently smaller activation energy of carriers in QRs is effectively compensated and the operating temperature of QRIPs is improved.

致　謝

完成這本論文，最要感謝的是指導老師李建平教授和王祥宇博士。李教授提供了一個優質的研究環境，讓我在研究資源的需求上無後顧之憂，並以潛移默化的方式培養我獨立研究的能力，更時常激勵大家維持對學問的熱情，細細品味研究學問所能帶來的樂趣和成就感。李教授嚴謹的治學態度、豐厚的學養與待人處世的風範，以身教的方式讓我瞭解成為一個優質學者所該具備的條件。王祥宇博士是對我在紅外線偵測方面的研究幫助最大的推手，其精闢的見解與論文指導使我獲益良多。王博士敏銳的思考，清晰的邏輯，以及在工作上嚴謹認真的態度和優秀能力，再再是我學習的榜樣。

還要感謝林聖迪教授，林教授廣泛靈活的思維與見解也屢屢拓展了我在研究上的視野。在實驗方面，曾經在 MBE 系統上共同奮鬥付出心力的學長及學弟：李秉奇博士、林志昌博士、王興燁博士、羅明城學長、林大鈞學弟、潘建宏學弟，你們是實驗能夠順利進行的最重要份子。尤其是羅明城學長，你是我在實驗室共事最久，在實驗方面也學習最多的學長；近幾年在你認真負責的帶領之下，我們的 MBE 系統得以順利運作，實驗室的研究也才能順利進行，謝謝你！實驗室其他曾經共事的學長、同學，以及學弟妹們的陪伴，也讓我在這將近六年的研究生活中多采多姿，溫馨愉快。能夠身為本實驗室的一份子，在這個環境學習成長，是多麼幸運的一件事。

此外，我要感謝在背後支持我的女友曉蓮，在我後期緊湊艱辛的研究生活中，妳的關心和陪伴是我能堅持到最後的動力之一。

最後，由衷地感謝我的家人在我求學過程中的支持與包容。妹妹義不容辭幫我負起陪伴父母的責任，令我感激萬分。從小到大父母對我的養育之恩，我沒齒難忘。這幾年來我積極向學，有很大的動力來自於不願辜負父母對我的期望。我要將這份博士畢業的喜悅與榮耀獻給我的父母，如果說我有什麼一絲一毫的成就，都要歸功於你們對我無怨無悔的付出，謝謝你們，我愛你們！

謹將此論文獻給所有關心我支持我的師長朋友，謝謝你們。

Contents

Abstract (Chinese) i

Abstract (English) iii

Acknowledgement (Chinese) v

Contents vi

Table Captions ix

Figure Captions x

Chapter 1 Introduction 1

1.1 Zero-dimensional Quantum Structures 1

1.2 Infrared Detection with Quantum Structure Infrared Photodetectors 3

1.3 Organization of this Dissertation 6

Chapter 2 Experimental Techniques 8

2.1 Molecular Beam Epitaxy Growth 8

2.2 Material Characterization 14

2.3 Device Fabrication Process 18

2.4 Device Characterization 19

Chapter 3 Manipulation of the Geometry and Sheet Density of InAs Quantum Dots/Rings by Self-assembly Methods 26

3.1 Introduction to Self-assembled Quantum Dots and Quantum Rings 26

3.2 Growth of Self-assembled InAs/GaAs Quantum Dots 28

3.3 Manipulation of the Sheet Density of InAs Quantum Dots 29

3.4 Manipulation of Geometry: Evolution of Self-assembled InAs Quantum Ring Formation 34
3.5 High Density Quantum Rings with Strong Photoluminescence Emission at Room Temperature 50
3.6 Summary 53

Chapter 4 Energy-dependent Carrier Relaxation in Self-assembled InAs Quantum Dots 54
4.1 Introduction to the Selective Excitation Photoluminescence Spectroscopic Studies on Carrier Relaxations 54
4.2 Sample Growth and Basic Characterization 56
4.3 Discussion for Large Quantum Dots: Electronic State Relaxation and Optic-phonon Filtered Relaxation 59
4.4 Discussion for Small Quantum Dots: Electronic State Relaxation with No Optic-phonon Filtering Effect 64
4.5 Summary 68

Chapter 5 Manipulation of Detection Wavelength and Device Performance in InAs Quantum Dot Detectors by Tailoring the Confinement Schemes 69
5.1 Introduction to the Confinement Dependency of the Polarization Intraband Transitions in Self-assembled Quantum Dots 70
5.2 Tuning of the Detection Wavelength and Polarization Response in InAs Quantum Dot Infrared Photodetectors 72
5.3 Comparison between the LWIR Quantum Dots-in-a-well detectors with and without Thin AlGaAs Layers 80
5.4 Summary 88

Chapter 6 Confinement-enhanced Quantum Dots-in-a-well Infrared Photodetectors 90

6.1 Introduction 91

6.2 Detailed Device Characterization for CE-DWELL QDIPs 92

6.3 Comparison between the CE-DWELL detectors with thin and thick $Al_{0.3}Ga_{0.7}As$ CE-layers 97

6.4 Comparison between the CE-DWELL detectors with $Al_{0.2}Ga_{0.8}As$ and with $Al_{0.3}Ga_{0.7}As$ CE-layers 103

6.5 Summary 109

Chapter 7 InAs/GaAs Quantum Ring Infrared Photodetectors 110

7.1 Introduction 110

7.2 Basic characteristics of the sample 111

7.3 Investigation of the Device Characteristics 113

7.4 Summary 120

Chapter 8 Conclusions and Future Work 121

8.1 Conclusions of the Present Studies 121

8.2 Future Work 123

Reference 126

Vita 133

Publication List 134

Table Captions

Table 3.1 InAs QDs growth parameters and characterization results. ………………………30

Figure Captions

Fig. 1.1 Density of states for charge carriers in structures with different dimensionalities [ref. 1.3]. ……………………………………………………………………………2
Fig. 1.2 (a) The blackbody exitance spectrum at near room temperatures. (b) Atmospheric transmission windows in the infrared range of the optical spectrum. This example of the spectrum is for transmission through 300 m of humid air at sea level [ref. 1.5]. ….4

Fig. 2.1 Sketch of the Varian Gen II MBE system in our lab. …………………………………10
Fig. 2.2 The RHEED patterns that generated by (a) a 2-D surface construction and (b) a 3-D surface construction. ……………………………………………………………………12
Fig. 2.3 Real space representation of the formation of the first complete monolayer of (001) GaAs with respect to RHEED intensity oscillations. θ is the fractional layer coverage [ref. 2.2]. ……………………………………………………………………………...13
Fig. 2.4 One of the measured RHEED oscillations for GaAs in our MBE system. …………...14
Fig. 2.5 Schematic illustration of an atomic force microscope. ………………………………15
Fig. 2.6 The instrument setup for PL, PLE and micro-PL measurements in our lab. …………16
Fig. 2.7 The top view of a single device for infrared detectors on the wafer. …………………19
Fig. 2.8 The responsivity spectrum measurement setup. …………………………………....21
Fig. 2.9 The measurement setup for obtaining absolute responsivity using blackbody. ………21
Fig. 2.10 The setup for noise spectrum measurement (top side) and dark current measurement (bottom side). ……………………………………………………………………..23
Fig. 2.11 The typical noise current spectrum of QSIPs. ………………………………………24
Fig. 2.12 Schematic photon detection mechanism in QSIPs: (a) photo-electron generation (including absorbing photons and escaping to become free carriers for electrons) followed by (b) current replenishment from electrodes (the behavior of gain establishing). ……………………………………………………………………...25

Fig. 3.1 The 1x1 μm^2 AFM images and the low power (~1 W/cm^2) PL spectra at 13K of the samples. ………………………………………………………………………………31
Fig. 3.2 The 1x1 μm^2 AFM images and the low power (~1 W/cm^2) PL spectra at 13K of the samples. ………………………………………………………………………………33
Fig. 3.3 Schematic for the growth process of self-assembled InAs QRs. ……………………..35

Fig. 3.4 The 1x1 μm^2 AFM images of (a) LM4594 (quantum dots), (b) LM4593 (quantum volcanos), and (c) LM4592 (quantum rings), and the representative surface profile of individual structure in each sample. ……………………………………………………37

Fig. 3.5 The PL spectra of LM4594 (no annealing), LM4593 (anneal at 450 ^{o}C), and LM4592 (anneal at 470 ^{o}C) under low excitation power (~1 W/cm^2) at 13K. …………………38

Fig. 3.6 The 1x1 μm^2 AFM images of (a) LM4641 (quantum dots), (b) LM4602 (quantum volcanos), (c) LM4601 (quantum rings), and (d) LM4600 (quantum rings), and the representative surface profile of individual structure in each sample. ………………41

Fig. 3.7 The plan view TEM image of the imbedded QRs. ……………………………………42

Fig. 3.8 The PL spectra of LM4641 (continuous capping), LM4602 (5.5 nm cap layer), LM4601 (4 nm cap layer), and LM4600 (2.5 nm cap layer) under low excitation power (~1 W/cm^2) at 13K. ……………………………………………………………………..42

Fig. 3.9 Scenarios of a lens-shaped InAs island partially covered by (a) a thicker GaAs layer and (b) a thinner GaAs layer respectively. The three arrows indicate different interfacial tensions acting at the borders between GaAs, InAs, and As vapor. ………43

Fig. 3.10 (a) The AFM image and (b) the PL spectra with different excitation power at 13K of LM4599. The inset in (a) shows the surface profile of the InAs dot pointed by the arrow. ……………………………………………………………………………………..45

Fig. 3.11 (a) Half of the side-view cross-section of the volcano-like structure illustrating the evolution from QD to QR and the formulation for the time-independent eigenstate wavefunctions. (b) The calculated electron energies of the low-lying states as functions of volcano's center height, h. (c) 2-D plots of some electron wavefunctions of the QD (h = 9 nm) and the QR (h = 0.65 nm). …………………………………...47

Fig. 3.12 The PL spectra of the QD sample at 1.5K in magnetic field perpendicular to the sample surface. ……………………………………………………………………...49

Fig. 3.13 (a),(b) The 1x1 μm^2 AFM images and (c) the PL spectra at 13K of the QRs with different annealing duration for ring formation. ……………………………………51

Fig. 3.14 The power-dependent PL spectra with normalized ground-state peak intensity of (a) QDs and (b) QRs. Also illustrated in the inset is the representative surface profile of a single structure. At the right hand side are the 3-D AFM images of (a') QDs and (b') QRs. ……………………………………………………………………………………52

Fig. 4.1 The 1x1 μm^2 AFM image and the surface profile of large QDs (sample A). ………...58

Fig. 4.2 The 0.25x0.25 μm^2 AFM image and the surface profile of small QDs (sample B). ….58
Fig. 4.3 SEPL spectra of large QDs (sample A) obtained at 13K. The cross on the right-hand side of each spectrum indicates the excitation energy. The inset shows the high-power PL spectrum. ……………………………………………………………………………59
Fig. 4.4 SEPL spectra of sample A with the intensity normalized, exhibited as a function of relaxation energy (E_{ex} – E_{det}). The three regions I, II, and III correspond to different excitation and relaxation mechanisms. ……………………………………………………60
Fig. 4.5 Schematic excitation and relaxation processes for (a) region I, (b) region II, and (c) region III in Fig. 4.4. …………………………………………………………………62
Fig. 4.6 SEPL spectra of small QDs (sample B) obtained at 13K. The x-axis refers to E_{ex} –E_{det} and the intensity of each spectrum is normalized for clarity. The inset displays the PLE spectrum detected at 1.269 eV. ……………………………………………………………65
Fig. 4.7 Relaxation energy as a function of ground state energy plotted for the two resonant peaks in Fig. 4.6. The dash-line curve is the PL spectrum of the sample showing the size distribution of the QDs. The band diagram in the inset is constructed for the most populated QDs. …………………………………………………………………………66

Fig. 5.1 1x1 μm^2 AFM images of the QDs grown on (a) the GaAs surface and (b) the InGaAs strained layer. ……………………………………………………………………………73
Fig. 5.2 Responsivity spectra of the five QDIP samples with negative bias at around 40K. Each active-layer structure is illustrated on the right hand side respectively. The QD layers are all grown with InAs materials. ………………………………………………………...74
Fig. 5.3 Cross-sectional TEM image of the confinement-enhanced DWELL structure with a thin AlGaAs layer. …………………………………………………………………………77
Fig. 5.4 Polarization dependence of the integrated responsivity of the five QDIPs measured under the 45° edge- coupling configuration illustrated in the inset. Also added on to the figure is the data (empty circles) of a GaAs- AlGaAs QWIP with B-B type transition, demonstrating the polarization selection rule predicted for QWIPs. ………………...78
Fig. 5.5 0° polarized and 90° polarized photocurrent spectra of the CE-DWELL QDIP at different temperatures ((a), (b)) and different bias polarities ((b), (c)). ……………...79
Fig. 5.6 0° polarized and 90° polarized photocurrent spectra of the CE-DWELL QDIP with multi-color detection. ………………………………………………………………...80
Fig. 5.7 PL spectra of the three QDIP samples under high power excitations at 77K. ………..81

Fig. 5.8 Comparison of the voltage dependence of (a) the dark current, (b) the peak responsivity, (c) the current gain and (d) the quantum efficiency for the three samples at 77K. …..83
Fig. 5.9 Contour plots for the excited state wavefunctions calculated for (a) the conventional DWELL structure and (b) the CE-DWELL structure. ………………………………..85
Fig. 5.10 Comparison of the voltage dependence of (a) the noise current density at 1 kHz and (b) the specific detectivity for the three samples at 77K. ………………………………86
Fig. 5.11 Responsivity spectra at different bias polarities of the asymmetric CE-DWELL QDIPs. ………………………………………………………………………………88

Fig. 6.1 (a) The schematic diagram of the CE-DWELL QDIP and (b) the 3-D AFM image of the sample. …………………………………………………………………………93
Fig. 6.2 (a) The PL spectra with different excitation powers and (b) the photocurrent spectra of the sample. …………………………………………………………………………93
Fig. 6.3 Photocurrent spectra of the sample at different temperatures. ………………………..94
Fig. 6.4 Voltage dependence of responsivity of the sample at different temperatures. ………..94
Fig. 6.5 Voltage dependence of (a) current gain and (b) quantum efficiency of the sample at different temperatures. ……………………………………………………………..95
Fig. 6.6 Voltage dependence of specific detectivity of the sample at different temperatures. ...96
Fig. 6.7 Schematic diagram of the CE-DWELL structures with thin and thick AlGaAs CE-layers. ……………………………………………………………………………97
Fig. 6.8 Cross-sectional TEM image of the sample with 3 nm AlGaAs layer on the QDs. …...97
Fig. 6.9 High power PL spectra of the two samples at 77K. ………………………………..98
Fig. 6.10 The voltage dependence of the peak responsivity of the two samples at 77K and 200K. The inset shows the responsivity spectra of the two samples at -1.35V and 77K. …...99
Fig. 6.11 The photocurrent spectra of the thick AlGaAs sample under positive bias and negative bias at 77K. ……………………………………………………………………99
Fig. 6.12 The current gain curves of the two samples at 77K and 200K. ……………………100
Fig. 6.13 The polarization-dependent photocurrent spectra of (a) the thin AlGaAs sample and (b) the thick AlGaAs sample at 40K under the 45° facet-coupled configuration. ……..101
Fig. 6.14 The specific detectivity curves of the two samples at 77K, 120K, 160K and 220K. 102
Fig. 6.15 The PL spectra of the samples with different Al content in the AlGaAs confinement enhancing layer. The PL spectrum of the conventional DWELL structure is also included. ……………………………………………………………………...104

Fig. 6.16 (a) Schematic diagram of the CE-DWELL QDIPs and (b) the 3-D AFM image of the sample RN0615. …………………………………………………………………...104
Fig. 6.17 (a) The high power PL spectrum and (b) the photocurrent spectra with different bias polarities of the sample RN0615. ……………………………………………………105
Fig. 6.18 The voltage dependence of responsivity of the two samples at different temperatures. ………………………………………………………………………………106
Fig. 6.19 The voltage dependence of (a) quantum efficiency, current gain and (b) detectivity of the two samples. …………………………………………………………………...106
Fig. 6.20 The voltage dependence of responsivity of the sample at 77K, 140K and 170K. The photocurrent spectrum is also included in the insert. ……………………………...107
Fig. 6.21 The voltage-dependent specific detectivity of the sample at different temperatures. ………………………………………………………………………………108

Fig. 7.1 (a) 1 × 0.5 μm^2 AFM image of the surface QRs. (b)(c) The cross-sectional TEM images of the imbedded QR layers and a single imbedded QR. ……………………………112
Fig. 7.2 The PL spectra of the sample at 77K with different excitation powers. The excited state peaks are indicated in the high excitation spectrum. ………………………………..113
Fig. 7.3 The photocurrent spectra of the sample at 30K and 77K. The insert shows the transitions associated with the response peaks. ……………………………………..114
Fig. 7.4 Polarization-dependent photocurrent spectra of the sample at 22K under 45° facet-coupled configuration. ………………………………………………………...114
Fig. 7.5 The voltage dependence of the peak responsivity of the sample at different temperatures. ……………………………………………………………………...117
Fig. 7.6 Temperature dependent FWHM of the PL spectra of single-layer QRs (solid symbol) and single-layer QDs (unfilled symbol). The insert shows their spectra at 20K. …...118
Fig. 7.7 The voltage dependence of the dark current of the sample with different temperatures and the dark current activation energies (Ea) at different bias voltages. ……………119
Fig. 7.8 The voltage dependence of specific detectivity of the sample at different temperatures. …………………………………………………………………………...120

Chapter 1

Introduction

The advance in technology of III-V semiconductor heterostructures has realized various optoelectronic devices which are ubiquitous in our modern life. For example, light emitting diodes, laser diodes, photodetectors and modulators, have been applied in optical display, optical communication, optical storage/readout, optical interconnect, and image detection/display [1.1-1.2]. With the advanced growth techniques such as molecular beam epitaxy (MBE) and metal organic chemical vapor deposition (MOCVD), the epitaxy of nanometer scaled semiconductor heterostructures becomes mature and therefore the fascinating quantum confinement effect can be applied to these devices to manipulate their characteristics and also drastically enhance their performances. In particular, defect-free, self-assembled, zero-dimensional quantum structures have made it possible to observe and even exploit the atom-like physical phenomena in these structures. In this dissertation, studies of the growth and analysis of self-assembled InAs quantum dots/rings and their applications on infrared photodetectors especially for the long-wavelength infrared (LWIR, 8-12 μm) detection were executed.

1.1 Zero-dimensional Quantum Structures

Zero-dimensional (0-D) quantum structures are structures with ultimate quantum confinement so that the confined carriers are constrained in all directions. In such structures, the quantization for all three dimensions generates the δ-function like density of states, i.e. forms a discrete density of states (Fig. 1.1). With the discrete nature of energy states, semiconductor 0-D quantum structures mimic the fundamental characteristics of an atom but provide suitable physical properties allowing the practical application of atomic physics to the field of semiconductor devices. Furthermore, as Fig. 1.1 shows, sequentially extending the

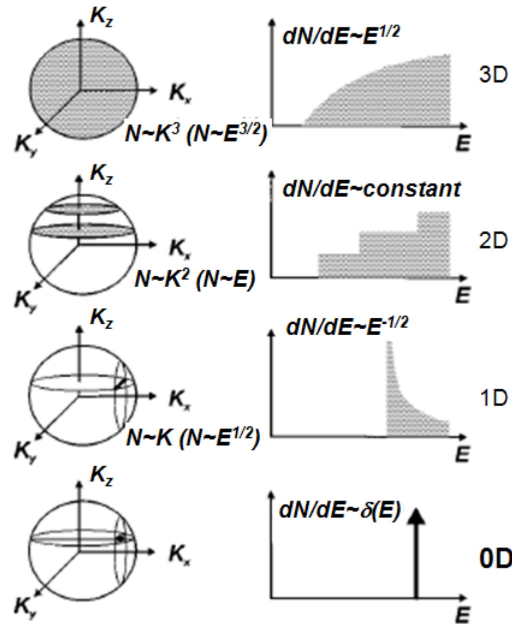

Fig. 1.1 Density of states for charge carriers in structures with different dimensionalities [ref. 1.3].

confinement to all three dimensions also sequentially raises the lowest allowed state energy in the structures with the absolute energy level depending critically on the size and depth of confining potential. Thus, the electronic and optoelectronic properties of the 0-D quantum structures can be flexibly manipulated via the confinement engineering.

It is important to appreciate how small a structure must be to form effective 0-D quantum structures. In fact, the spacial shrinkage of the potential well in all directions modifies not only the single-particle density of states (Fig. 1.1) but also the electron-hole Coulomb interaction. However, while the single-particle energy levels scale as $1 / L^2$, where L is the confinement length for each direction, the Coulomb interaction energy scales as only $1 / L$. When L shrinks down to the scale of the bulk exciton radius (~10 nm for GaAs and ~30 nm for InAs), the correlated motion of the electron-hole pair becomes no longer allowed. The Coulomb-induced electron-hole correlations become very weak but the quantum confinement effects become dominant, compelling the electron-hole pair to occupy the lowest-energy pair of single-particle levels without any level mixing [1.4]. Furthermore, in this regime, the quantum confinement reduces the electron-hole separation, enhances the exciton oscillator strength, and

thereby enhances the optoelectronic properties.

Similar arguments can be made about the effects of temperature. For quantum effects to remain important for the operation of 0-D quantum structures, the splitting between the quantized levels should be substantially greater than k_BT to ensure that thermal effects do not distribute electrons and holes over multiple levels and dilute the concentration of the density of states provided by the confinement. The actual confinement length required to provide this splitting depends on the effective mass of electron or hole and the details of the confining potential. At room temperature, k_BT is about 26 meV. As a useful rule of thumb for room temperature operation of semiconductor quantum devices, the energy splittings are large enough for the L of around 10 nm.

In short, when the size of confinement structures is reduced in all directions to the scale of the bulk exciton radius in material, 0-D quantum structures are formed. The strong quantum effects generate effective energy quantization/splitting which is not screened by the thermal fluctuations in structures and govern many fundamental properties of the structures. As a consequence, the size, shape and potential depth of such 0-D quantum structures can be used to quantum engineer their optical response by tailoring the desired transition energies, transition strengths, and polarization dependence, etc. It is the reason why 0-D quantum structures are so fascinating and are envisioned as the key for next-generation optoelectronic technologies.

1.2 Infrared Detection with Quantum Structure Infrared Photodetectors

From the basic radiation theory, every object with non zero temperature radiates electromagnetic waves. The temperature-dependent radiation spectrum is well known and follows the Planck's theory. The projected spectral density of the power emitted by a blackbody per unit area (into the entire hemisphere) is expressed by

$$M = \frac{2\pi hc^2}{\lambda^5}\frac{1}{e^{hc/\lambda kT}-1}\left(\frac{\mathrm{W}}{\mathrm{cm}^2\cdot\mu\mathrm{m}}\right) \tag{1.1}$$

where M is the spectral exitance, h is the Planck's constant, λ is the wavelength. For a normal object, the radiative spectral density can be approximated by the product of the above expression and an emissivity factor. Based on eq. (1.1), the radiation peak wavelength can be determined by Wien's displacement law:

$$\lambda_{peak}\, T = 2898 \quad (\mu m \cdot K). \tag{1.2}$$

As the temperature increases, the radiation peak wavelength shifts to short wavelength side. Fig. 1.2(a) shows the blackbody radiation spectrum at near room temperature. For 300K objects, the wavelength region where the exitance decays to one half is around 6 μm to 17.5 μm. Thus, if we want to detect the radiation emitted by a room temperature object, the appropriate detection wavelength should be in this range. However, as shown in Fig. 1.2(b), because of the absorption by the atmosphere, most infrared region is opaque. The only two transparent window regions are around 3-5 μm (MWIR) and 8-12 μm (LWIR). This fact restricts the

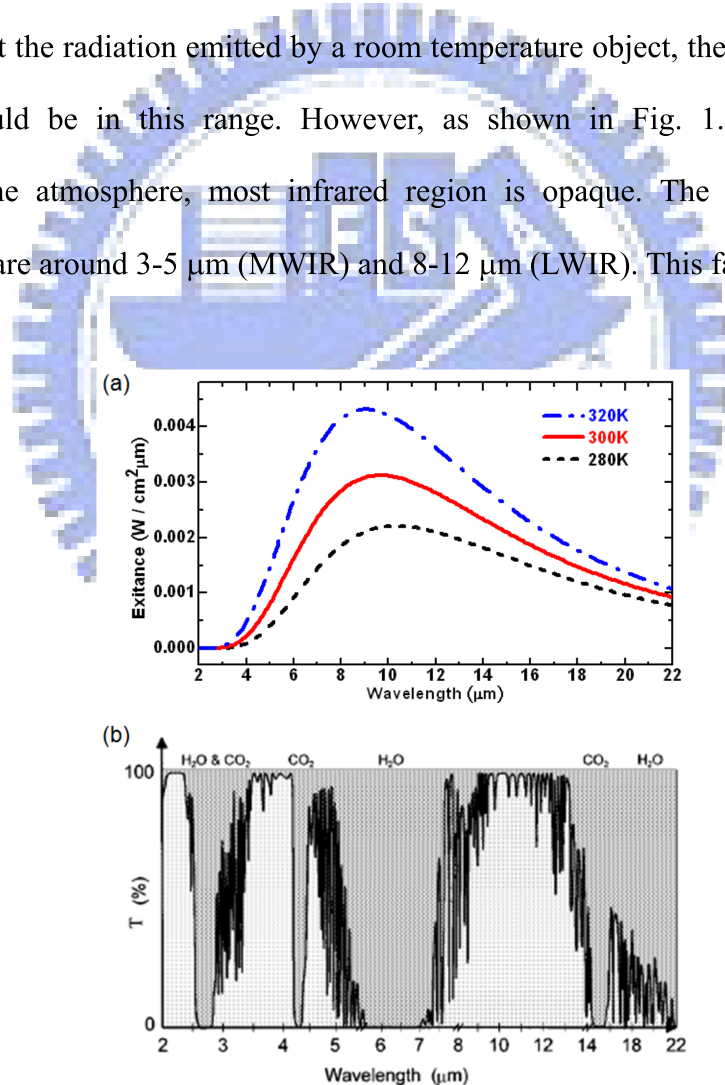

Fig. 1.2 (a) The blackbody exitance spectrum at near room temperatures. (b) Atmospheric transmission windows in the infrared range of the optical spectrum. This example of the spectrum is for transmission through 300 m of humid air at sea level [ref. 1.5].

infrared detection of objects on the earth at a distance. Comparing with Fig. 1.2(a) and (b), the most efficient infrared detectors aimed for detecting room temperature objects on the earth should be with the LWIR detection band. LWIR detectors are quite essential for the applications including night vision, remote sensing, environmental monitoring, and military target tracking, etc.

Conventional semiconductor photon detectors are operated via photoexcitation of carriers across the bandgap. For the detection of LWIR band, the bandgap energy (E_g) of the materials should be in the range of 0.1-0.15 eV. Such small-bandgap semiconductors, e.g. $Hg_xCd_{1-x}Te$, are well known to be more difficult to grow, process, and fabricate into devices than are larger-bandgap semiconductors. These difficulties thus motivate the study of novel “artificial” low “effective” bandgap materials which use quantum structures in large-bandgap ($E_g > 1eV$) semiconductors, e.g. $Al_xGa_{1-x}As$, $In_xGa_{1-x}P$. However, in order to employ these desired large gap materials for long-wavelength optical devices, the intersubband (i.e. intraband, mainly aimed at the conduction band) absorption mechanism rather than the usual interband absorption mechanism should be exploited. In order to create suitable, quantized energy states within the conduction band, quantum structures are used. An incident infrared photon with energy equal to the intersubband spacing of the quantized states in the structure can promote the ground-state electron to the excited state, where, with appropriate bias, the electron can be extracted out and then collected as a photoelectron, contributing to the electric signal.

The infrared detection using quantum structure intersubband transition was first experimentally demonstrated in 1985 by West and Eglash using AlGaAs/GaAs quantum wells [1.6]. After that, extensive studies have been being done on various quantum well infrared photodetectors [1.7]. Furthermore, with the breakthrough in self-assembled quantum dot growth, since 1998, 0-D quantum structures have been also used as the absorption media in infrared detectors due to the theoretically predicted superior performances [1.8-1.9]. Until now, development in quantum structure based infrared photodetector (QSIP) technologies, including

quantum wells, dots, superlattices, and novel heterostructures, has led to the realization of high performance infrared detectors, large-format focal plane arrays [1.10-1.11], and infrared cameras that now readily available commercially through several manufacturers. Compared with HgCdTe detectors, which have been investigated for over 50 years but are still very expensive in the fabrication cost, faster progress is definitely achieved in QSIP technologies due to the advantages including the mature GaAs growth and processing techniques, which lead to high uniformity, excellent reproducibility, and thus large-area, low-cost staring arrays. However, the operation of high performance QSIPs still requires cryogenic cooling. Cooling requirements are the main obstacle to the more widespread use of infrared systems based on semiconductor photon detectors making them bulky, heavy, expensive and inconvenient to use. For this reason, many researchers from all parts of the world have been still working to elevate the operating temperature of QSIPs to make them more powerful.

1.3 Organization of This Dissertation

In this dissertation, we try to get a comprehensive understanding of the growth control and electronic properties of self-assembled InAs 0-D quantum structures, and then put it into practice to realize LWIR QSIPs with improved performances and thus higher operating temperature. The experimental techniques used are described in chapter 2, including MBE growth, material characterization methods, device processing procedures, and QSIPs measurement techniques.

In chapter 3, the growth control on the self-assembled InAs quantum dots (QDs) and their geometric tailoring into quantum rings (QRs) are studied. Then, the influence of the geometric change during dot-to-ring evolution on electronic wavefunctions and state energies is discussed. Finally, the growth condition of high density and high quality QRs which are good for device applications is presented.

In chapter 4, the energy spectra of self-assembled InAs QDs are investigated using the

selective excitation photoluminescence technique. Three distinct regions with different mechanisms in carrier excitation and relaxation are identified in the emission spectra excited with different photon energies. The special joint density of state tail of the QD that extends from the wetting layer bandedge facilitates carrier relaxation and is posited to explain these spectral results.

In chapter 5, InAs QDs with different confinement barrier schemes are used in quantum-dot infrared photodetectors (QDIPs) for the detection wavelength and polarization absorption tuning. A novel confinement-enhanced dots-in-a-well (CE-DWELL) structure is shown to possess both the LWIR detection and the high normal-incident absorption capabilities. Most importantly, the device quantum efficiency is greatly enhanced with this new design.

In chapter 6, we perform detailed studies on the InAs/AlGaAs/$In_{0.15}Ga_{0.85}As$ CE-DWELL QDIPs. It is found the thickness and Al content of the AlGaAs insertion layers influence much not only the absorption property but also the transport property of the device. With appropriate device parameters of CE-DWELL, we present LWIR QDIPs with operation temperatures over 200K.

In chapter 7, the infrared photodetectors using InAs QRs as the absorption media are investigated. Compared with QDIPs, quantum ring infrared photodetectors (QRIPs) show wider photocurrent spectra, more stable responsivity with temperature change, and lower dark current activation energy due to the shallower confined states of electrons. With an $Al_{0.27}Ga_{0.73}As$ current blocking layer, the operating temperature of QRIPs is greatly elevated.

Finally, conclusions and a plan for future work are given in chapter 8.

Chapter 2

Experimental Techniques

The samples investigated in this dissertation were all grown by the molecular beam epitaxy (MBE) technology. After growth, the material characteristics of the samples were examined routinely by the atomic force microscopy (AFM) as well as the photoluminescence (PL) spectroscopy. Besides, the transmission electron microscopy (TEM) analysis was also performed for certain samples. For the samples aimed for infrared detectors, standard processing techniques including lithography, etching and metalization were used for the device fabrication. Measurements were then done to characterize the device performance, including I-V characteristics, responsivity spectra, and noise level. In this chapter, all of the above experimental techniques are briefly described.

2.1 Molecular Beam Epitaxy Growth

The epitaxy of nanometer scaled heterostructures is of increasing importance for both the physical studies and the quantum device associated applications. To fulfill this task, precise control over the epi-layer thickness as well as its composition including doping profile is essential. The molecular beam epitaxy (MBE) technique, which allows the epitaxial growth with atomic dimensional precision down to a few angstroms, emerges as the most promising approach. The MBE is a physical deposition process which takes place in an ultra-high vacuum (UHV) environment. The epitaxial growth proceeds via the reaction of molecular beams of the constituent elements with a crystalline substrate surface held at a suitable substrate temperature under UHV conditions. The high vacuum environment is the key leading to the advantages of the MBE growth. In the UHV environment, the mean free path of the molecules evaporated from each effusion cell is longer than the distance between the sources and the substrate, so the molecules strike directly on the substrate without any scattering event. For that reason, with the

fast switching action of the shutter in front of each cell, the amount of respective source molecules sticking onto the substrate can be precisely controlled by time and the cell temperature. Precise layer structures with abrupt interfaces within the atomic-layer thickness can therefore be achieved. The UHV environment also limits the amount of impurities inside the chamber so that the quality of the epitaxy films can be preserved. Moreover, under such high vacuum conditions, many surface analysis techniques can be performed *in situ* for the sample right after or even during the growth process [2.1].

2.1-1 MBE Apparatuses and Pre-growth Procedure

The MBE system in our lab is the Varian (or Veeco) Gen II (solid-source based) system, one of the most commonly used experimental commercial systems. It includes two individual epitaxy units (named LM and RN respectively) that are linked by an extension chamber. The two epitaxy units have basically the same configuration. Fig. 2.1 sketches the configuration for the LM system. The whole system comprises three chambers: the entry/exit chamber, the buffer chamber, and the growth chamber. The pumping machines are basically oil free. A turbo-molecular pump cascaded by a scroll pump (by a diaphragm pump for the RN system) is used for rough pumping. In the growth chamber, a cryopump and an ion pump are used to maintain high vacuum environment and a titanium-sublimation pump (TSP) is also equipped and used when the vacuum level is not good. In addition, the liquid-nitrogen-cooled cryopanel is installed within the growth chamber, surrounding the substrate manipulator and each cell, to improve the vacuum level during sample growth and also eliminate the cells from thermal cross-talk. For the buffer chamber, an ion pump and a TSP are used to keep the vacuum level. In the entry/exit chamber, a smaller cryopump is used.

Eight effusion cells are installed in the LM chamber. Two gallium cells, one aluminum cell and one indium cell are used for group III sources. One arsenic Kunsden cell and one arsenic valved cracker cell are used for group V sources. The other two cells are charged with

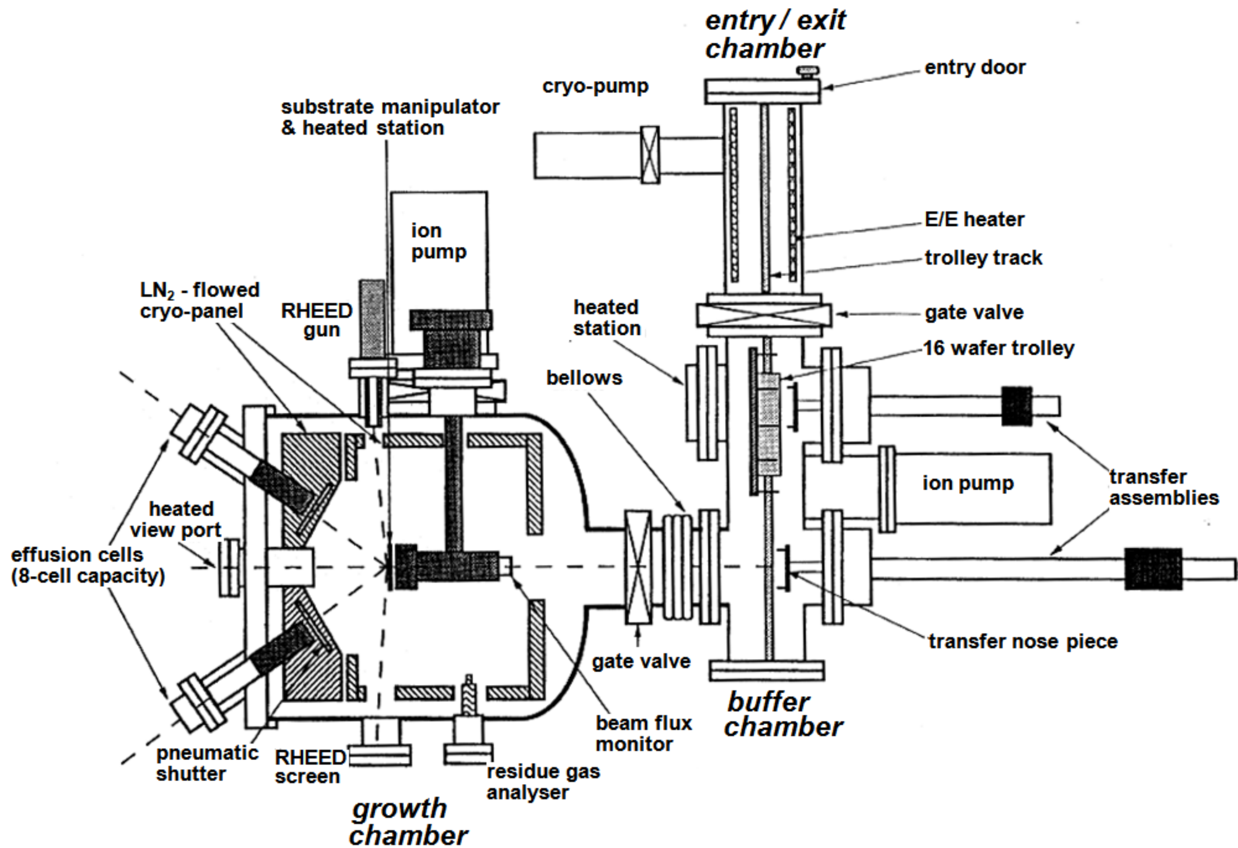

Fig. 2.1 Sketch of the Varian Gen II MBE system in our lab.

silicon and beryllium as n-type and p-type dopant sources. Thus, the LM chamber supplies the growth of arsenide based III-V materials. For example, AlGaAs, InGaAs on GaAs substrates; InAlAs, InGaAs, and InGaAlAs on InP substrates. For the RN chamber, there exist ten ports for source cell installation. Thus, besides the eight cells stated above, one antimony valved-cracker cell is also used for another group V source. So the RN chamber provides the opportunity for growing antimony related III-V materials on the substrates with larger lattice constant, such as InAs, GaSb, etc.

Also equipped in the growth chamber are two analysis instruments: the residue gas analyser (RGA) and the reflection high-energy electron diffraction (RHEED) monitor. The RGA is used to analyze the residue gas in the chamber and thereby help us to understand the cleanness in the chamber. By setting the detection range to only for the atomic mass unit (AMU) of 4, i.e. only monitoring the helium element, the RGA also serves as a very sensitive leak

detector. The RHEED is a powerful surface analysis instrument and is commonly used in the MBE system. More description about it will be given later.

To maintain the cleanness of the growth chamber and ensure the quality of grown samples, a standard treatment procedure for wafers before growth is necessary. Epi-ready GaAs wafers are mounted on molybdenum holders with springs and then loaded on a wafer trolley. After loading the trolley into the entry/exit chamber, the whole chamber is baked at 200 ^{o}C to remove the residual water molecules on the wafers. When the pressure is lower than $1x10^{-8}$ torr, the trolley is transferred into the buffer chamber, in which the standby pressure is typically $1\text{-}5x10^{-10}$ torr. In this chamber, each wafer is put on a heated station and then heated up to 400 ^{o}C for further removing other contamination such as organic species. After about three hours, when the pressure in the buffer chamber is definitely lower than that in the growth chamber (stand by at around $3x10^{-9}$ torr), the wafer is ready for epitaxy growth and can be transferred into the growth chamber. It should be noted that, before the cells are warmed up for sample growth, the cryopanel is fed with continuous-flowed liquid nitrogen to further lower the pressure of the growth chamber, typically, from ~$3x10^{-9}$ torr to less than $2x10^{-10}$ torr. Just before growth, the thin native oxide on the wafer surface is decomposed and desorbed by heating under enough arsenic flux. The desorption temperature depends on wafer materials and is about 620 ^{o}C for GaAs wafers. The temperature of the wafer is read by a pyrometer, which faces the heated viewport in front of the growth chamber (Fig. 2.1) and detects the thermal radiation from the wafer.

2.1-2 In Situ Surface Diagnosis and In Situ Growth Rate Calibration by Reflection High Energy Electron Diffraction

The situation of desorption can be easily traced with the RHEED instrument in the growth chamber. As mentioned previously, the RHEED is a powerful surface analysis

technique. It allows us to *in situ* monitor the surface construction of wafer or epi-layers. By using high-energy (about 10 keV) incident electron beam with a very small glancing angle (about 1-2°), the structure of the outermost layers of atoms of the sample can be analyzed with the diffraction patterns. When the RHEED pattern changes from an obscure pattern to a bright streaky pattern, it is suggested that the wafer surface becomes clean enough and desorption process is completed. After desorption, the epitaxy growth can be started. In principle, higher temperature can improve the quality of epi-layers, but the sticking coefficient of molecules decreases, especially for the species with smaller chemical bonding energy. In our system, the growth temperature for AlGaAs and GaAs is roughly at 600 ^{o}C, and for the pseudomorphic growth of InGaAs the temperature is at about 510 ^{o}C. While for the strain-induced three-dimensional (3-D) island growth of InAs, the so-called self-assembled quantum dot (QD) growth, the temperature is generally in the range between 480 ^{o}C and 520 ^{o}C, depending on the desired QD condition. Such 3-D island growth can be also *in situ* identified by use of the RHEED technique. Specifically, if the epitaxy growth goes in a 2-D layer-by-layer mode, a streaky RHEED pattern will be obtained in the meantime (see Fig. 2.2(a)). Once the surface construction transition from 2-D to 3-D occurs, the growth will proceed subsequently in a 3-D mode with the RHEED pattern also transiting from the streaky pattern (Fig. 2.2(a)) to the spotty pattern (Fig. 2.2(b)). Such a spotty RHEED pattern is commonly regarded as the indication

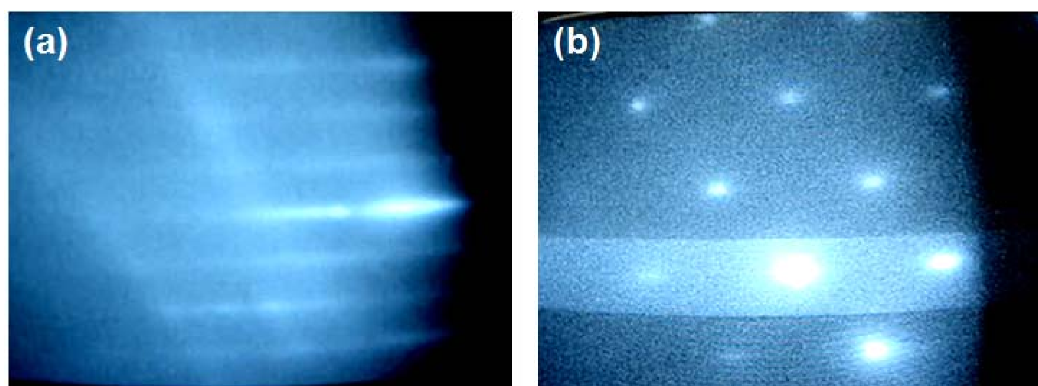

Fig. 2.2 The RHEED patterns that generated by (a) a 2-D surface construction and (b) a 3-D surface construction.

that the deposition amount of InAs is sufficient for QD formation. More details about the growth of the self-assembled InAs QDs will be described in the next chapter.

Besides the capability of surface construction analysis, the oscillatory behavior of the RHEED specular beam intensity also provides us a convenient method to *in situ* calibrate the growth rate. An explanatory diagram is shown in Fig. 2.3, in which θ is the fractional layer coverage. The equilibrium surface existing before growth is smooth, corresponding to high reflectivity of the specular beam. As growth starts, nucleation islands will form at random sites on the surface, leading to a decrease in reflectivity (due to enhanced random scattering). These islands grow in size until they coalesce into a smooth surface again. It is expected that the minimum in reflectivity would correspond to 50% coverage by the growing layer. Hence, the period of the oscillations corresponds precisely to the elapsing time for the growth of one monolayer. The behavior of layer-by-layer epitaxy growth can be thereby appreciated by observing the oscillation of the RHEED intensity.

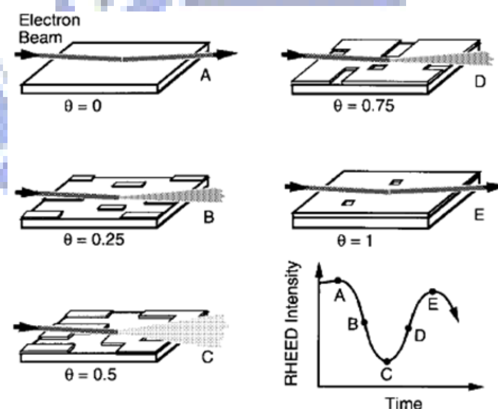

Fig. 2.3 Real space representation of the formation of the first complete monolayer of (001) GaAs with respect to RHEED intensity oscillations. θ is the fractional layer coverage [ref. 2.2].

Fig. 2.4 shows an example for the layer-by-layer growth of GaAs. Clear oscillatory behavior is observed for the RHEED intensity in spite of damped amplitude. This damping characteristic suggests that the growth gradually changes from a sequentially layer-by-layer mode to a stable step-flow mode. A growth rate of about one-fourth monolayer per second can

be derived from Fig. 2.4. It should be noted that one monolayer contains both Ga and As atoms and is equivalent to a half of the lattice constant. It is only the beam flux of Ga that determines the growth rate under As rich conditions [2.3]. For GaAs, the V-III flux ratio used in our lab is roughly 10 for As_2 and 20 or higher for As_4. Excess As_2/As_4 is lost by re-evaporation and therefore stoichiometric GaAs can be grown. The beam flux ejected from each cell is measured by a beam flux monitor equipped on the substrate manipulator (Fig. 2.1). The orientation of the substrate manipulator is changed by 180° for the beam flux monitor to face the effusion cell for beam flux sensing.

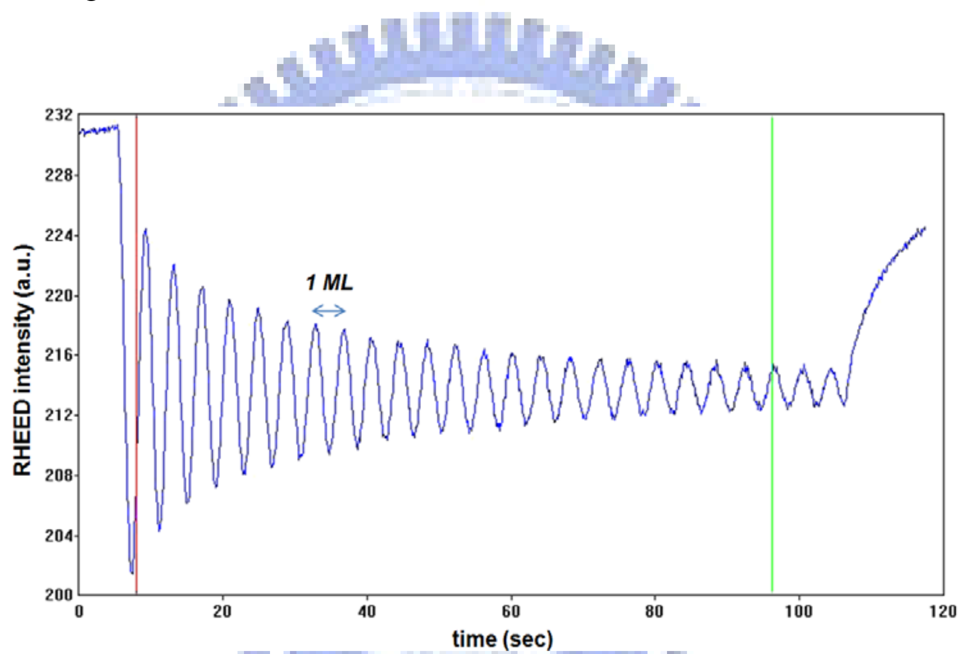

Fig. 2.4 One of the measured RHEED oscillations for GaAs in our MBE system.

2.2 Material Characterization

2.2-1 Atomic Force Microscopy

Atomic force microscopy (AFM) is a fast and convenient method for nano-scale surface characterization in semiconductor industry due to its operability in ambient air and minimal sample preparation for investigation. The AFM operation principle is illustrated in Fig. 2.5. The instrument consists of a cantilever with a sharp tip mounted on its end. It is the force between

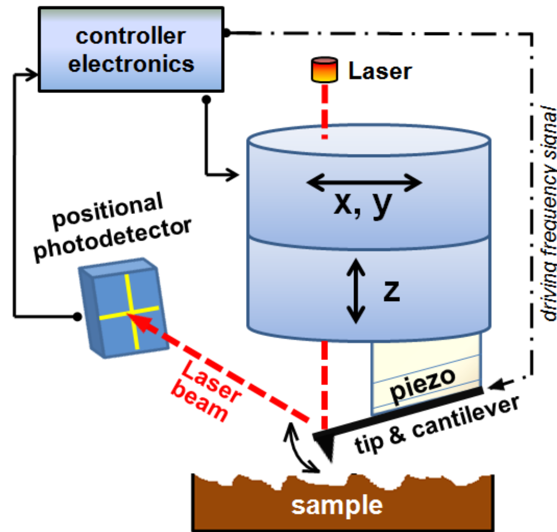

Fig. 2.5 Schematic illustration of an atomic force microscope.

the apex of the tip and the surface atoms in the sample that produces the AFM operation [2.4]. Such force depends sensitively on the distance between the tip and the sample. Considering the compromise between high image resolution and minimal damage creation for both samples and tips, the tapping mode was used throughout in this dissertation. The cantilever is excited close to its resonant frequency by a driving signal applied to the piezoelectric ceramic to which the cantilever is attached. The excited oscillation of the tip/cantilever is appropriately damped by the force between the tip and the sample due to an appropriate tip-sample distance, and the oscillation amplitude is recorded by a positional detector which detects the laser signal reflected by the end of the cantilever (see Fig. 2.5). With a feedback-control electronics and a 3-D scanning mechanics, when the oscillating tip scans over the surface of the sample, one can keep the tip-sample distance constant by keeping the oscillation amplitude constant. In this manner, the topography on the sample surface can be obtained with the resolution reaching ~1 nm. In our lab, the AFM is performed by a Veeco Digital Instrument D3100 commercial system, primarily for understanding the geometry, sheet density, and uniformity condition of the 3-D quantum objects in the samples.

2.2-2 Photoluminescence Spectroscopy

Photoluminescence (PL) spectroscopy is a very practical and efficient material characterization method for most III-V semiconductors, in which the process of the electron-hole (e-h) recombination is mainly radiative. It serves to determine the fundamental bandgap (E_0) of the sample, understand the crystalline quality of the sample, and identify the impurity species in the sample [2.5]. When a sample are excited by an optical source, typically a laser with photon energy $h\nu > E_0$, e-h pairs are generated, subsequently followed by a carrier thermalization process (including diffusion, capture, and relaxation of the carriers), and then the PL signals are obtained from the spontaneous emission of the sample due to the radiative e-h recombination. In our lab, the samples grown by our MBE machines are routinely characterized by a homemade PL system as shown in Fig. 2.6. Such a system has the capability of, besides the conventional PL, also the PL-excitation (PLE), resonant PL and micro-PL measurements.

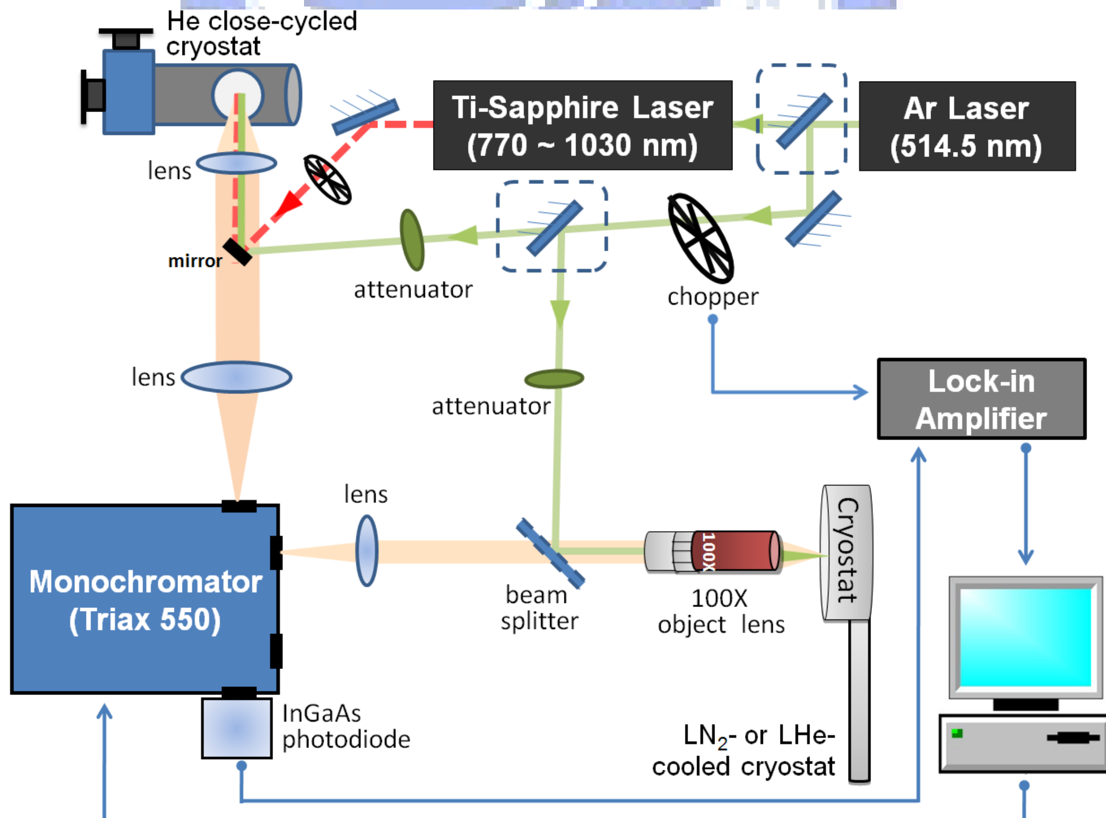

Fig. 2.6 The instrument setup for PL, PLE and micro-PL measurements in our lab.

For conventional PL measurement, an argon ion laser is used as the excitation source and the samples for investigation are mounted in a helium close-cycled cryostat, where the sample temperature can be maintained at from ~13K to room temperature. While for PLE or resonant PL, a Ti-sapphire laser pumped by the argon laser is instead used to excite the samples. The excitation photon wavelength can be tuned from ~770 nm to ~1030 nm using different lens kits. The emission signal of the sample was collected by a couple of plano-convex lenses, transferring through air space, dispersed by a 0.55m monochromator, and then detected by a thermal-electric cooled InGaAs photodiode. Using mechanical choppers to modulate the laser beams, the signal-to-noise ratio can be greatly improved by such a lock-in technique. Besides, a 100 times long-working-distance object lens along with an OXFORD designed liquid nitrogen/helium cooled cryostat is used for the micro-PL measurement, where the spot size of the excitation beam can be focused down to only ~1.5 μm. We take advantage of its ultra-high excitation density to obtain PL spectra revealing high-lying excited states of the InAs quantum objects that are studied in this dissertation.

2.2-3 Transmission Electron Microscopy

Transmission electron microscopy (TEM) is a powerful technique for obtaining highly magnified sample images with extremely high resolution, approaching 1-2 Å [2.6]. A very high energy electron beam, typically around 100-400 keV, is deflected and focused on the sample by electro-optic condenser lenses, and passes through the sample, forming a magnified image in the image plane which is then simply projected onto a fluorescent screen. The sample must be sufficiently thin (a few tens to a few hundred nm) to be transparent to electrons. Due to such a thin thickness, few electrons are absorbed in the sample. Thus, image contrast does not depend very much on absorption, as it does in optical transmission spectroscopy, but rather on scattering and diffraction of electrons in the sample.

Images formed using only the transmitted electrons are bright-field images and that using

a specific diffracted beam are dark-field images. On the other hand, if large aperture is used so that one transmitted beam plus many diffracted beam are all collected in the image plane, high-resolution images are formed. The image brightness is determined by the intensity of those electrons transmitted through the sample that pass through the image forming lenses. Therefore, heavier elements cause stronger scattering, hinder the electrons from reaching the fluorescent screen, and thus create dark image in the TEM picture. In general, for crystalline specimen, the contrast in the TEM images may arise from mass contrast, thickness contrast, diffraction contrast, etc. In this dissertation, TEM pictures are all obtained by a JEOL JEM-2100F field-emission TEM system using high-resolution image mode. Different from the AFM technique, which was routinely performed for every sample, TEM analysis was only performed for certain samples in this dissertation due to the challenging, time-consuming task on sample thinning.

2.3 Device Fabrication Process

The device samples for the studies of quantum structure infrared photodetectors (QSIP) in this dissertation were all grown on semi-insulating GaAs substrates with the type of vertical transport structure, i.e. active region is sandwiched between a top-contact and a bottom-contact n+ GaAs layers. Discrete devices were fabricated by a two-step process using standard processing techniques. Lithography for pattern definition was achieved by the I-line (365 nm) exposure source and the 5214E photoresist. First, wet chemical etching (with the solution of $H_2SO_4 : H_2O_2 : H_2O$ = 1: 8 : 80, etching rate being about 8 nm/sec at room temperature) was used to etch mesa down to reveal the bottom contact layer. Each mesa has a size of 260×370 μm^2. Then, E-gun evaporation (30nm Ni / 70nm Ge / 300nm Au was deposited in sequence for n-type ohmic metal) was used to metalize the top and the bottom contact-layers at the same time. The metal contact on the mesa was purposely formed with a ring-shaped geometry to

allow normal incidence measurement from the mesa top. The optical window has a size of 200×200 μm^2. After lift-off by acetone, the sample was treated by rapid thermal annealing (at 385°C for 30sec) to form good ohmic contact for the devices. The top-view picture of a completed single device on the wafer, taken by an optical microscope, is demonstrated in Fig. 2.7. It should be noted that the mesa etching does not penetrate through the bottom contact layer. As a result, the devices, although discrete, all share the same electric bottom contact, rather than being completely isolated.

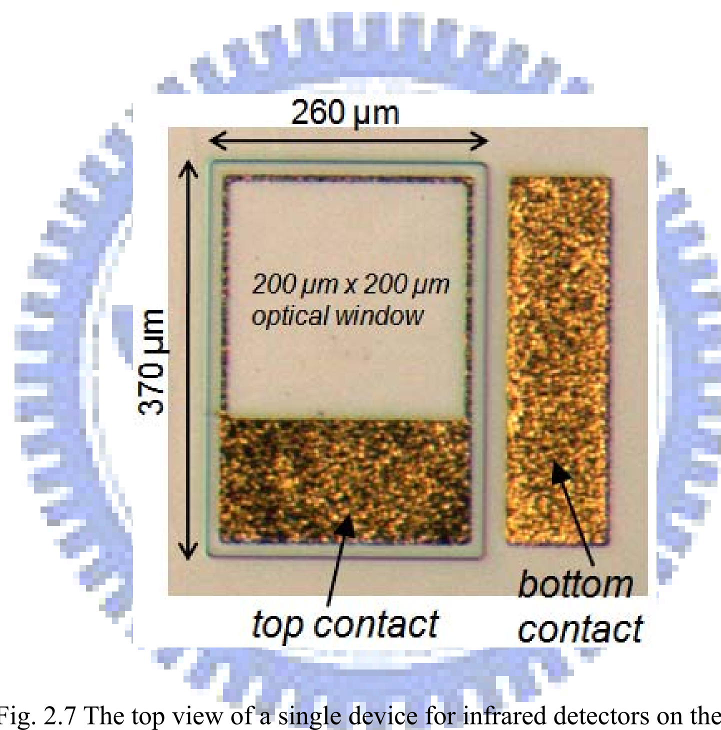

Fig. 2.7 The top view of a single device for infrared detectors on the wafer.

2.4 Device Characterization

After device fabrication, the sample was stuck onto a sample holder by silver glue. The sample holder is a good thermal conductor and has ten conductive fingers for wire bonding. Since all devices in the sample share the same electric bottom contact, nine devices can be chosen for measurement at most. Wire bonding was performed on the top-contact metal of the selected nine devices, connecting them respectively to different fingers on the holder. Two to

three of the bottom-contact metal pads were randomly selected from the wafer and wire-bonded to the residual finger on the holder. The sample holder carrying sample was then mounted in a helium close-cycled cryostat with electric feed-through for low temperature measurements.

The detector performance is judged by three important characteristics: I-V characteristics, responsivity spectrum, and noise level [2.7]. Responsivity is the electrical output for a given infrared input, and noise is the "clutter" that tends to hide the true signal. They are usually combined into one parameter, called detectivity, which represents the signal-to-noise ratio and is an important overall figure of merit for detectors [2.7]. The characterization procedure for our QSIPs is described in the following. First of all, the low temperature (~40K) I-V characteristics of the nine wire-bonded devices are examined one by one through a Keithley-236 source-measure instrument. To make a fast evaluation of the dark current level for each device, a polished cold shield inside the cryostat is used to reduce the background radiation illuminated onto the sample. The device temperature is monitored by a calibrated temperature sensor installed beside the sample. The purpose of the measurement at this time is to pick on an appropriate device for detailed investigations. In long-term statistics, the device yield is in the range of 15~60 %. Such a low yield is detrimental for the focal plane array application and is tentatively attributed to the not-high-enough growth temperature for the GaAs barrier layers in our QSIPs. Considering the stable growth temperature for InAs active layers, the GaAs barrier layers were not grown at its proper temperature. More studies about this issue should be done to improve the device yield.

After finding the appropriate device, we then measure the responsivity spectrum for QSIPs. This is achieved by Fourier transform infrared spectroscopy (FTIR) [2.5] and a blackbody radiation source. Fig. 2.8 shows the FTIR measurement system. This method can get the spectrum faster than using a monochromator. The FTIR used in our lab is made by Nicholet co. with computer control. It provides the measurement range from 2.5μm to 25μm. However, the ZnSe optical window on cryostat blocks the transmission of the photons with wavelength

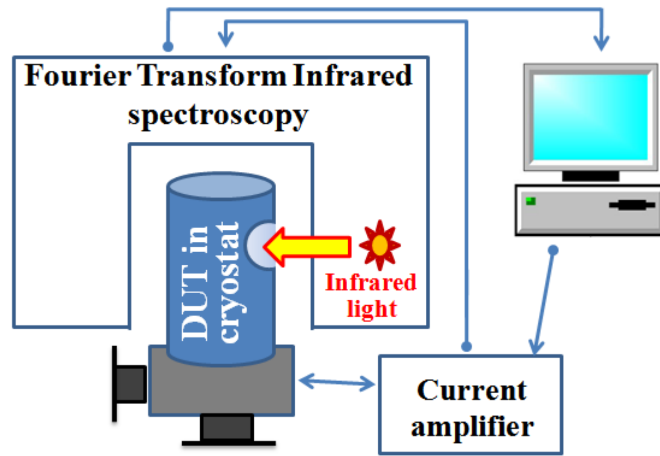

Fig. 2.8 The responsivity spectrum measurement setup.

longer than 20μm. The cold shield inside the cryostat is removed from the device under testing (DUT) to allow the illumination of the infrared light emitted from the FTIR. The photo-response signal produced by the DUT is first amplified by an SR-570 current amplifier and then fed into FTIR. The relative responsivity spectrum is obtained by the software for QSIPs at different biases and temperatures. After that, the spectra are calibrated by a Graseby Infrared blackbody source set at 1000 °C. The absolute responsivity measurement setup is shown in Fig. 2.9. Again, the lock-in technique is used to improve the signal-to-noise ratio. Besides, a germanium wafer is inserted in the optical path to filter out photons with wavelength

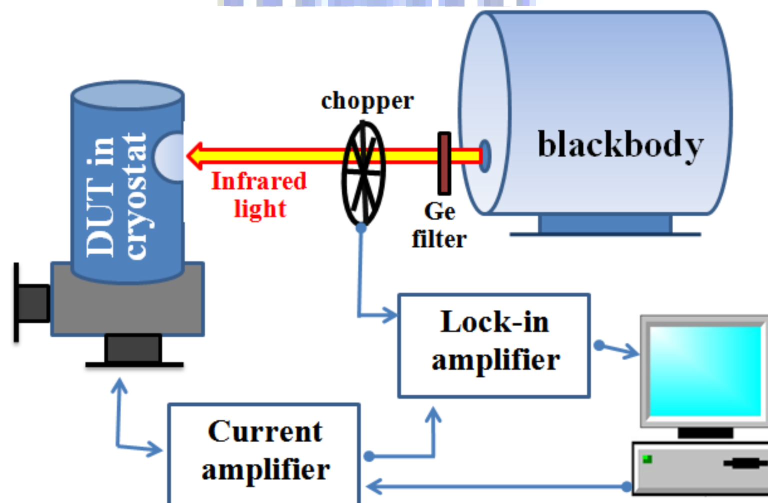

Fig. 2.9 The measurement setup for obtaining absolute responsivity using blackbody.

shorter than 2μm to insure that the measured photocurrent comes from the intra-band instead of the inter-band transition in QSIPs. The DUT detects the chopped blackbody radiation and produces an ac photocurrent, which is amplified previously by an SR-570 current amplifier and then by an SR-530 lock-in amplifier. Typically, the chopper frequency is set at 1 kHz for the measurement. The measured photocurrent comes from the excitation blackbody source which is a wavelength-continuous light source. Therefore, combined with the relative responsivity spectrum, the peak responsivity can be calculated by the following equation:

$$R_{peak} = \frac{I_{ph}}{A \cdot E \cdot MF \cdot T_{Ge} \cdot T_{ZnSe} \cdot T_{GaAs} \cdot \int \tilde{R} \cdot Q \cdot d\lambda} \qquad (2.1)$$

Where I_{ph} is the measured photocurrent, A is the area of the device optical window (200x200 μm^2), and Ts are the transmission of the Ge wafer, ZnSe window, and GaAs wafer which are about 0.64, 0.7 and 0.7, respectively. $\tilde{R}$ is the peak-normalized responsivity spectrum and Q is equal to the blackbody spectral exitance expressed by the equation (1.1). MF is the modulation factor of the chopper, and in our system it is about 0.38. E is the normal-incidence configuration factor given by:

$$E = \frac{(d/2)^2}{D^2 + (d/2)^2} \qquad (2.2)$$

Where d is aperture size of the blackbody source and D is the distance between the source and the sample. In our case d is 4 mm and D is 140 mm. The absolute responsivity spectrum is obtained once the peak responsivity is obtained. With different bias points, the relation between applied voltage and peak responsivity is also obtained by this setup. Frequently, the voltage-dependent responsivity is measured at different temperatures to understand the temperature-dependent behavior of QSIPs.

After the above optical measurements taken in the close-cycled cryostat are finished, the sample is then transferred into a dewar containing liquid helium to measure the dark current and the noise level of QSIPs. The measurement setup is shown in Fig. 2.10. The sample is

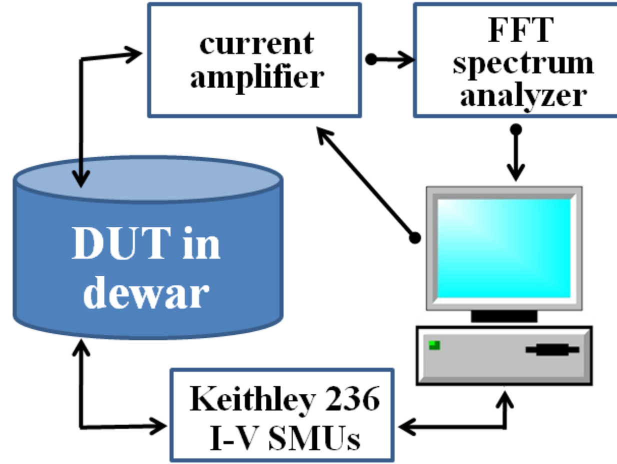

Fig. 2.10 The setup for noise spectrum measurement (top side) and dark current measurement (bottom side).

mounted on an electrical insert and the device for measurement is soldered with a low-noise coaxial cable. The noise spectrum is measured by an SR-770 fast-Fourier-transform (FFT) spectrum analyzer. The device dark current is first amplified by the SR-570 and then sent into the FFT spectrum analyzer. All the connection is made by the BNC cable to eliminate the coupling of outside noises. Besides, proper grounding is needed. The signal from the FFT is the combination of noises of all the circuit components. Accurate results of QSIP noise can be obtained by extracting all the equivalent circuit parameters [2.8]. However, since the resistance of QSIPs is usually higher than 1 MΩ at low temperatures, the noise spectral density can be well described by a simplified equation

$$V_n^2 \simeq V_{n0}^2 + A^2 I_n^2 \tag{2.3}$$

where V_n is the measured noise voltage (in the unit of V/(Hz)$^{0.5}$), V_{n0} is the noise under open circuit, and A is the gain of the SR-570 amplifier. A typical noise spectrum obtained for QSIPs is shown in Fig. 2.11. The flat shape characteristic for frequency higher than about 1 kHz shows that the noise is dominated by the frequency-independent noise mechanisms, which include Johnson noise and generation-recombination (G-R) noise [2.7]. That is,

$$I_n^2 \simeq I_{n,Johnson}^2 + I_{n,G-R}^2 \tag{2.4}$$

In the case of QSIPs, the Johnson noise is usually far smaller than the G-R noise and can be

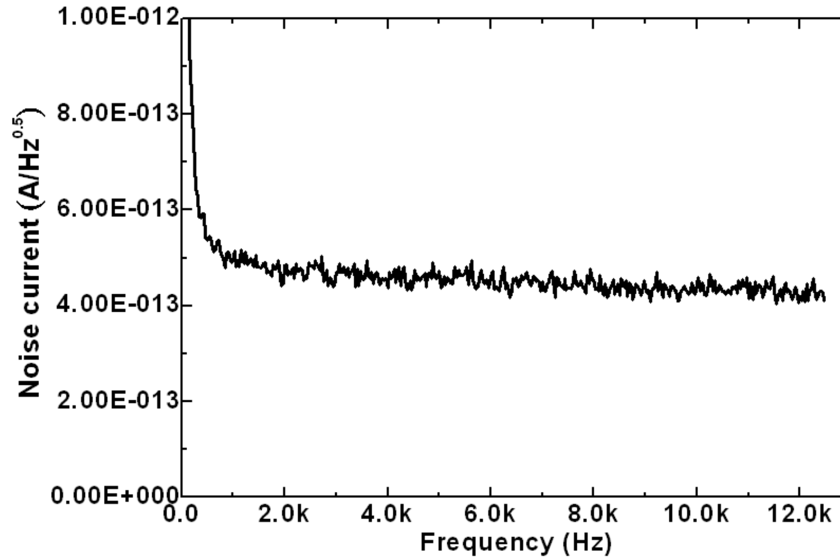

Fig. 2.11 The typical noise current spectrum of QSIPs.

neglected. We use the noise current density measured at around 1 kHz to calculate the specific detectivity for our QSIPs through the definition [2.7]

$$D^* = \frac{R_{peak}\sqrt{A'}}{I_n} \tag{2.5}$$

where *A'* is the area of the device mesa (370x260 μm^2). Due to the limit of the measurement system, noise current smaller than 2x10^{13} A/Hz$^{0.5}$ could not be correctly measured in lower bias range at lower temperatures. So, for the device with very high resistivity, the operation window where accurate detectivity can be measured is especially narrowed. As for the dark current characteristic, it is directly measured by a Keithley-236 source-measure-unit (SMU). By making use of the temperature gradient in the dewar, the temperature dependence of the dark current or the noise current can be also measured.

For photoconductor detectors such as QSIPs, the detector's responsivity is determined by two important factors, quantum efficiency, η, and photoconductive gain, g, through

$$R_{peak}=(e/h\nu)\eta g \tag{2.6}$$

where ν is the photon frequency [2.7]. The two parameters η and g characterize the optical and the transport properties of QSIPs respectively. Their physical meanings can be schematically

clarified by Fig. 2.12. Quantum efficiency is the average number of photoelectrons (or free electrons) that can be generated from the quantum structures by one incoming photon. Photoconductive gain is the total number of induced conducting electrons from electrode per photoelectron for reaching the steady state of the photon absorption. Photoconductive gain can be approximated by noise gain [2.9-2.10] and calculated by

$$g \simeq g_n \equiv \frac{I_{n,G-R}^2}{4eI_d} \approx \frac{I_n^2}{4eI_d} \tag{2.7}$$

where g_n is the noise gain, I_d is the dark current, and I_n is the measured noise current density at around 1 kHz. The quantum efficiency can be obtained through equation (2.6) once the photoconductive gain is obtained. The factorization of quantum efficiency and gain from responsivity is commonly performed to understand the inner nature of QSIPs. However, we should keep in mind that equation (2.7) is only an approximation and it may cause serious deviation when the avalanche multiplication in QSIPs becomes prominent [2.11].

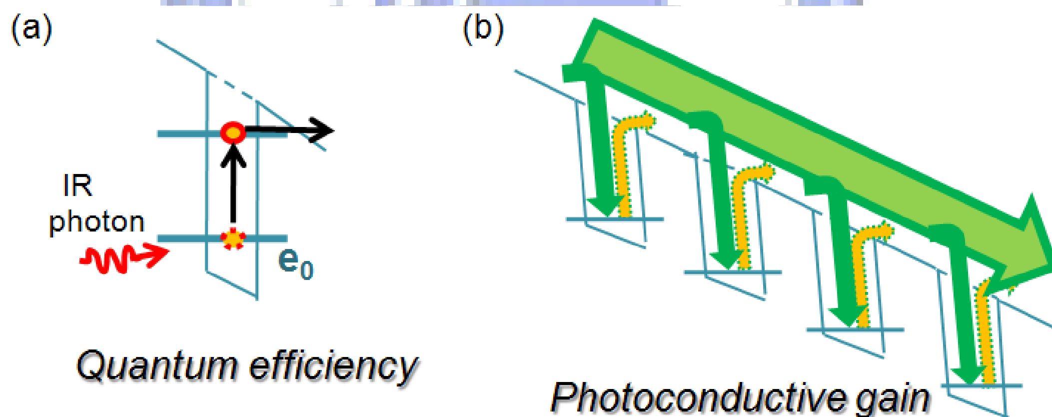

Fig. 2.12 Schematic photon detection mechanism in QSIPs: (a) photo-electron generation (including absorbing photons and escaping to become free carriers for electrons) followed by (b) current replenishment from electrodes (the behavior of gain establishing).

Chapter 3

Manipulation of the Geometry and Sheet Density of InAs Quantum Dots/Rings by Self-assembly Methods

In this chapter, we investigate the growth conditions to manipulate the sheet density and geometry of self-assembled InAs quantum dots (QDs) with fully *in situ* growth control. With appropriate growth parameters and growth procedures, a wide range of sheet densities from ~$1x10^{8}$ cm^{-2} to ~$1.2x10^{11}$ cm^{-2} is obtained. Furthermore, using the partial-capping and annealing technique, the shape of the QDs can be tailored into ring-like structures. The evolution of self-assembled InAs quantum ring (QR) formation is studied by AFM and PL spectroscopy. The influence of the geometric change during the dot-to-ring evolution on electronic wavefunctions and state energies is also studied by simulation. Finally, the growth condition of high density and high quality QRs which are good for device applications is presented.

3.1 Introduction to Self-assembled Quantum Dots and Quantum Rings

As mentioned in Chapter 1, zero-dimensional (0-D) quantum structures are expected to make revolutionary progress in the technology of optoelectronics due to their discrete density of states and the enhanced exciton oscillator strength. Experimental studies in this field for semiconductors started from the late 1980s, via ether the approach of lithography and etching [3.1] or the approach of strained layer self-assembled island growth [3.2]. The small nanostructures (≦ 50 nm in three dimensions) fabricated by etching usually suffer from serious degradation in quantum efficiency due to the process-induced defects at the interface, so they are not suitable for practical device applications where elevated operation temperature is usually required. On the other hand, using Stranski-Krastanow (S-K) mode growth, nano-islands can be formed spontaneously. These nano-islands, after *in situ* coverage of host material, are the so-called self-assembled quantum dots (QDs). They are free of the interface damage

problem and are promising for device applications [3.3]. Hence, since the early 1990s, huge amount of efforts have been expended to the growth and characterization of self-assembled QDs, especially in the $In_xGa_{1-x}As/GaAs$ system [3.4-3.18]. Until now, the fabrication of In(Ga)As QDs has been well developed. By manipulating the sheet density, InAs QDs with low enough density have been put on the studies of single photon sources [3.19] while QDs with high density have been put into practice in the technologies of laser diodes [3.20] and infrared focal plane arrays [3.21].

Besides QDs, quantum rings (QRs) are also 0-D quantum structures but have special nonsimply-connected geometry with rotational symmetry. Because the size is so small, the energy associated with the carrier motion even along the ring is quantized. Such special ring-like nanostructures have been received a considerable attention for decades [3.22-3.27]. Particular interest on QRs lies in its predicted magnetic property, such as Aharonov-Bohm effect, persistent current, and magnetization [3.25]. Again, the method of self-assembled growth, without the problem of interface damage, serves as the most promising approach to fabricate semiconductor QRs for ether physical studies or realistic applications. The formation of InAs ring-like nanostructures by self-assembly was firstly discovered by Garcia *et al* in 1997 [3.12]. They found that a remarkable morphological change of self-assembled InAs QDs would happen during growth if a pause was introduced after overgrowing the dots with a few nm of GaAs. Since then, the fabrication of semiconductor QRs by tailoring the geometry of QDs using *in situ* growth control has been studied extensively for different materials in the MBE technology [3.28-3.36].

Because the fabrication of QRs is achieved by transforming the geometry of QDs, it is important to appreciate this evolution process and then control it for obtaining quasi-realistic donut-shaped structures so that the particular magnetic properties of “rings” could be observed. Furthermore, the different geometric nano-objects at different stages of the evolution process must have different electronic state energies. The ability of manipulating these nano-objects

provides us with another freedom in tuning the working wavelength for the photonic devices operated either by interband transitions or by intraband transitions. In the following, the growth of self-assembled InAs QDs using MBE technique will be described at the beginning.

3.2 Growth of Self-assembled InAs/GaAs Quantum Dots

The typical growth procedure and the growth mechanism of the InAs/GaAs QDs grown by MBE in S-K mode are described as follows: at first, after desorption of native oxide, the GaAs buffer layer is grown in 2-D layer-by-layer mode. Then, InAs is deposited at an appropriate substrate temperature. The first few monolayers (MLs) growth of InAs on GaAs is in 2-D mode because of the smaller surface energy of InAs. However, due to the rapidly increased strain energy induced by the lattice mismatch (7.2%), the surface construction transition from 2-D to 3-D occurs for minimizing the total energy [3.3]. The energy relaxation at this stage is elastic so the resulted 3-D InAs islands are coherent to the substrate. By carefully controlling the amount of InAs deposition, defect-free InAs QDs form after GaAs capping. In general, such defect-free InAs/GaAs QDs could be obtained reproducibly with InAs deposition thickness less than 3 MLs. From previous studies, the thickness that would trigger the surface elastic relaxation was extracted to be 1.5 MLs [3.8]. This is the so-called critical thickness. So, the InAs QDs by S-K mode growth must come along with a thin wetting layer (WL), which will generate a 2-D quantum state in the QD layer. It should be mentioned that, however, the WL thickness is not a well defined constant but subtly depends on the growth conditions. The reported InAs WL thickness varies from 1.5 to 2 MLs. Such different thicknesses for WL means there exists a delay in the 2-D to 3-D phase transition, which is attributed to the persistence of the metastable 2-D growth during epitaxy [3.3]. After phase transition occurs, the nucleation of the islands is asynchronous and randomly distributed on the growth front due to the local fluctuations of the InAs flux that arrives at surface. Hence, due to such random growth process, the size of the QDs must have a distribution. The size

non-uniformity in self-assembled QDs is generally known to be the dominant factor for the inhomogeneous broadening in PL spectrum.

The final characteristics of the self-assembled InAs QDs depend on many factors including growth parameters, surrounding materials, and growth procedures [3.10-3.18]. Important growth parameters are: substrate temperature (T_{sub}), InAs ML thickness, InAs growth rate, As species, As pressure, etc [3.10-3.13]. Even if a specific growth recipe is used, the results may vary from chamber to chamber due to the difference in ether the chamber conditions or the parameter calibrations. Take the parameter T_{sub} as an example, the dependence of PL peak energy (E_0, the representative ground state transition of the QD ensemble) on T_{sub} surprisingly showed opposite trends for a wide range of T_{sub} (480°C ~ 535°C) in ref. 3.13 and 3.14. Therefore, it is necessary to master and monitor the growth conditions of QDs in individual growth chambers before controllably growing device samples.

In point of general optoelectronic devices, QDs with high sheet density are preferred; on the other hand, low density QDs are required for implementation of single photon sources. For that reason, it is significant to be able to manipulate the QD density.

3.3 Manipulation of the Sheet Density of InAs Quantum Dots

In this section, seven QD samples with different growth conditions are used to study the AFM images and the PL spectra. The growth parameters and the characterization results are listed in Table 3.1 for these samples. Parameters are purposely selected so as to enlarge their difference in QD densities. Each sample was grown with a single active InAs QD layer sandwiched between 150 nm GaAs barrier layers and a surface QD layer as the uncapped counterpart for AFM measurement. Besides, concerning that InAs QDs may be still far from their quasi-stable morphology just after InAs deposition finishes [3.37], a 20~30 seconds of growth interruption under As overpressure (the As_2 flux was commonly used) was performed before depositing GaAs cap layers in every samples.

Table 3.1 InAs QDs growth parameters and characterization results.

Sample #	T_{sub} (°C)	As (10^{-6} Torr)	In_G.R.(μm/hr)	In_MLs	D (10^{10}/cm^2)	E_0 (eV)
RN0069	515*	~1.3	0.056	0.3 x10	~0.01	1.102
LM4598	540	~1.3	0.033	3.2	0.5	1.112
LM4571	520	~1.3	0.056	2.6	2.3	1.128
LM4572	490	~1.3	0.056	2.6	8.5	1.185
LM4455	480	**~15**[a]	0.1	2.4	12	1.269
LM4786	520	~3.3	0.152	2.8	3.0	1.132
LM4563	520	~1.3	0.056	3.2	5.3	1.278

* The temperature with star was indicated by a different epitaxy system from the others. The nominal value should be added by about 20 °C if one would compare it with the others.

[a] The number with underline means As_4, others are As_2.

The AFM images and the low temperature PL spectra of the upper five samples in Table 3.1 are displayed in Fig. 3.1. A large difference in dot density is clearly seen. The QD densities span a wide range from ~$1x10^8$ cm^{-2} to ~$1.2x10^{11}$ cm^{-2}. The peak energy of each PL spectrum (E_0) also varies from 1.102 eV to 1.269 eV due to the different QD sizes (especially, the height of the dot). With minor difference in InAs deposition amount, a smaller QD size comes along with a higher QD density and results in a larger E_0 as predicted by the quantum mechanics.

We first consider the sample with medium sheet density (LM4571). As indicated by the AFM image, the QDs are quit uniform in size, with average height about 10 nm. Narrow size distribution is also reflected by the PL spectrum, of which the full-width-half-maximum (FWHM) is only 40 meV. With this QD condition (2.6 MLs InAs, 0.056 μm/hr growth rate and 520°C T_{sub}), strong PL emission can be reproducibly obtained even at room temperature. For that reason, the QD condition of LM4571 was frequently used for device fabrication in our lab. When we want to lower the QD density but keep the dot size large enough, we choose the

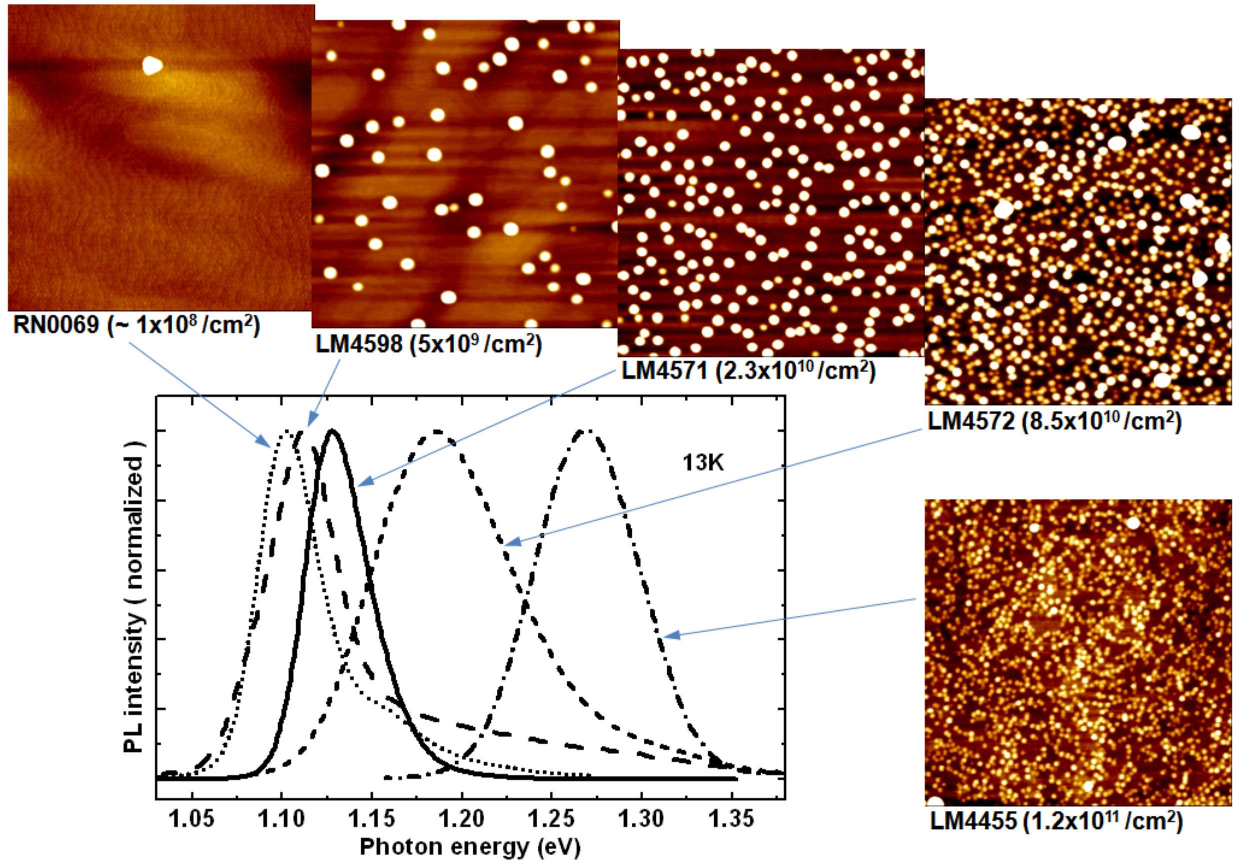

Fig. 3.1 The 1x1 μm^2 AFM images and the low power (~1 W/cm^2) PL spectra at 13K of the samples

growth parameters so as to increase the mobility of In adatoms and suppress the island growth from later nucleations. In this case, high growth temperature, low growth rate, and moderate deposition thickness for QDs are preferred. Concerning that the sticking coefficient of In will dramatically decrease when T_{sub} raised over ~545 ^{o}C, we chose 540 ^{o}C for QD growth. As demonstrated by the AFM image of LM4598, low density QDs with large sizes are obtained. The density is 5x10^{9} cm^{-2} and the average dot height is about 18 nm. The E_0 of LM4598, however, is only 16 meV smaller than that of LM4571 despite large difference in the uncapped dot heights (18 nm versus 10 nm). The result is attributed to the enhanced In-Ga intermixing during the GaAs overgrowth at such a high temperature of 540 ^{o}C [3.18], which results in a blue-shift in E_0 that counteracts the red-shift caused by the increased dot size. In fact, this inference has been confirmed by examining another sample with the T_{sub} of the GaAs cap layer

lowered to 505 ^{o}C while other conditions are kept the same. In this case, E_0 is further reduced to 1.061 eV (Fig. 3.7) due to suppressed intermixing effect. As mentioned, the QD density around several 10^9 per cm^2 can be obtained by high growth temperature along with low growth rate. This density, however, is sometimes not low enough for isolating a single QD. A special growth procedure was used in RN0069 for further reducing dot density. Ten periods of 0.3 ML InAs deposition followed with a 10 seconds interruption step were used for growing QDs, aimed to further suppressing the possible island formation from later nucleation. In this case, only one QD was observed in the 1x1 μm^2 AFM image (see Fig. 3.1). QDs with such an ultra-low density, ~10^8 cm^{-2}, are very promising for single photon sources. However, the reproducibility of this segmental flux growth is not very good and every so often the dot density of ~$2x10^9$ cm^{-2} is reached. The reason is not clear now and further investigations are needed.

On the other hand, high density QDs are always preferred for optoelectronic devices such as QD lasers and QD detectors. A direct approach for obtaining high density dots is to lower the growth temperature of QDs. The T_{sub} in LM4572 was lowered by 30 ^{o}C compared to LM4571, while all other growth parameters were kept the same. Comparing the AFM images, clear elevation of dot density is identified in LM4572 (Fig. 3.1). The sheet density is increased to $8.5x10^{10}$ cm^{-2} due to a much shorter In migration length at low temperature. However, it is also noticed that the size uniformity of the QDs obtained by this growth condition is not good. The FWHM of the PL spectrum in LM4572 reaches 91 meV, over two times larger than that in LM4571. Such severe inhomogeneous broadening in PL emission is usually unfavorable for device applications. To improve the size uniformity but not sacrifice the dot density, it is necessary to eliminate the coalescence of InAs islands during QD growth. In sample LM4455, the QDs were grown at 480 ^{o}C under As_4 overpressure. The purpose of using As_4 rather than As_2 is to further reduce the In migration length to lower the probability of coalescence. As indicated by the AFM picture, the number of coalescent dots is obviously reduced and the obtained QDs are very dense and small. The dot height is only ~1.5 nm (see Fig. 4.2) and the

dot density reaches 1.2×10^{11} cm^{-2}. Due to the ultra-small QD height, the E_0 greatly blue shifts to 1.269 eV. Although the QDs are relatively uniform judging from the AFM image, the FWHM of the PL spectrum reaches 72 meV due to increased sensitivity of confinement energy on size distribution in such small-size regime.

As described above, high density QDs could be easily achieved by lowering the growth temperature (to below 500 ^{o}C). However, the associate PL spectrum is generally so broad that the peak intensity is instead reduced. More than that, deteriorated crystal quality due to low temperature epitaxy around QD layers also makes the QDs unsuitable for room temperature applications. Hence, alternative approaches are required to increase the dot density at high enough growth temperatures (in general, ＞510 ^{o}C). Two approaches are introduced here. One is to increase the InAs growth rate and the other is to deposit a few MLs of AlAs before QD growth [3.17]. Both methods serve to reduce the In migration length. The obtained results are demonstrated in Fig. 3.2. Let us focus on LM4786 first. Compared with LM4571 (Fig. 3.1), the InAs growth rate here was raised for about 3 times while T_{sub} was unchanged. With this

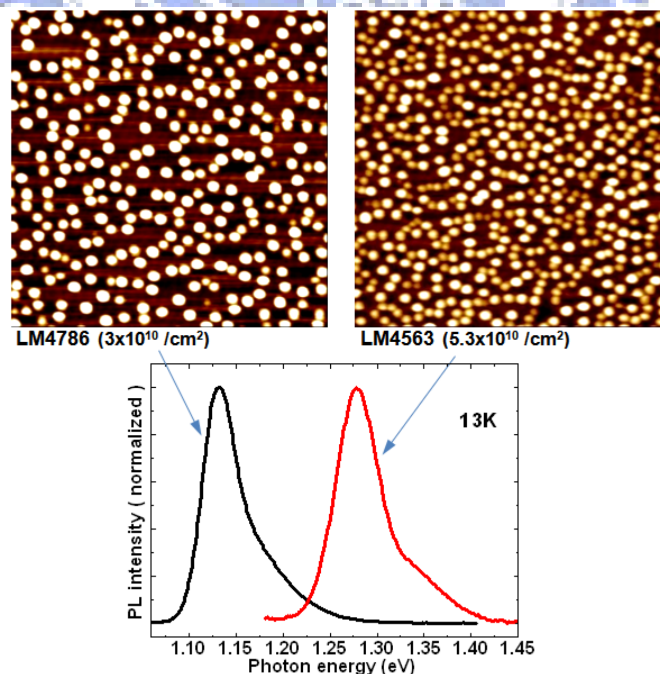

Fig. 3.2 The 1x1 μm^2 AFM images and the low power (~1 W/cm^2) PL spectra at 13K of the samples.

adjustment, the QD density was increased by a factor of 1.3. Note that with a slight increase in InAs deposition MLs, the QD size scarcely shrinks in spite of the increase in dot density. The E_0 shifts to high-energy side by only 4 meV. Using this growth condition, a sheet density of $3x10^{10}$ cm^{-2} and a FWHM of 48 meV are achieved. On the other hand, by introducing a 3 Å AlAs layer, the mobility of In adatoms is dramatically reduced and the density of the QDs is greatly increased to over $5x10^{10}$ cm^{-2} in LM4563. A relatively narrow size distribution is also obtained despite high density. It should be mentioned that, the E_0 reaches to 1.278 eV, an unexpected high energy. Although the dot size in LM4563 is larger than in LM4455 (5 nm versus 1.5 nm), the E_0 is instead higher in LM4563 than in LM4455. It means the Al atoms somewhat must be incorporated into the QDs and contribute to the electronic states. In general, the incorporation of Al to the InAs QDs is not preferred because it not only reduces the depth of confining potential but also deteriorates the material quality of the QDs.

3.4 Manipulation of Geometry: Evolution of Self-assembled InAs Quantum Ring Formation

In this section, we present detail studies on the evolution of shape transformation from QDs to QRs by using self-assembled growth technique. The growth procedure of self-assembled InAs QRs is schematically described in Fig. 3.3. At first, the InAs QDs are formed via S-K mode island growth. In the following, a GaAs layer is deposited with thickness thin enough to cover the QD sidewalls but leave the tips exposed. Due to the strain distribution on the QD layer, the deposited GaAs tends to accumulate on the region between InAs dots first, so plane-type coverage rather than conformal-type coverage is achieved. Then, with a proper duration of annealing (interruption under As flux), InAs materials are torn apart from the tip of the dots and migrate out to form ring-like structures. After the coverage of GaAs barrier layers, the QRs are completely formed.

The possible mechanisms of the outward migration of InAs materials from the QDs

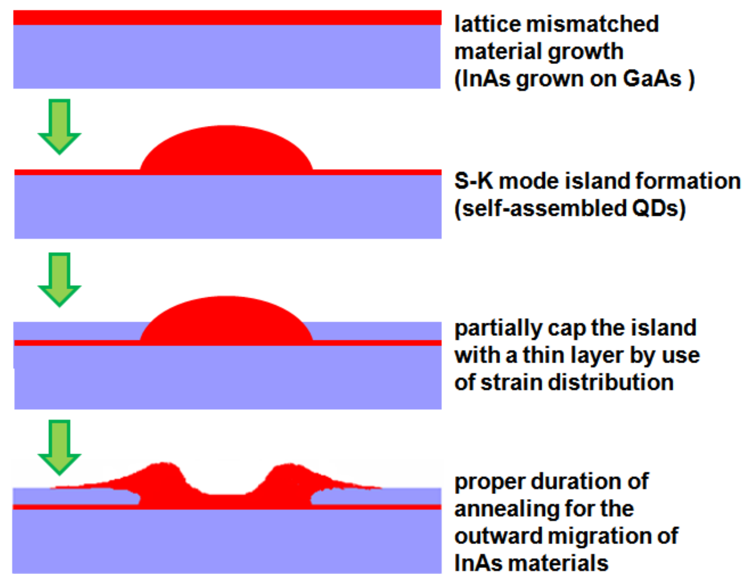

Fig. 3.3 Schematic for the growth process of self-assembled InAs QRs.

have been reported [3.28-3.30]. It was ascribed to (1) a higher In surface mobility (compared with Ga) which causes the outward “diffusion” of In atoms from the exposed portion of InAs QDs during the annealing duration [3.28] and (2) an outward driving force for In atoms generated by the instability at the interface between the exposed InAs droplets and the surrounding solid GaAs materials [3.29]. Therefore, the whole process is quite complicated. The surface migration (referred to as diffusion in Ref. 3.28) depends on the temperature and the duration of annealing, while the imbalanced surface tension at solid-liquid interface depends on the shape of the InAs dots and the thickness of the GaAs cap layer. In the following, the dependence of QR formation on the annealing temperature and that on the cap layer thickness are both investigated. The geometry and the optical properties of QRs at each stage of ring formation are recorded by AFM and PL techniques, respectively. The quantum effect associated with the dot-to-ring geometric changes is also studied by simulation.

3.4-1 Effect of Annealing Temperature and Dot Size on the Ring Formation

Three samples (LM4592-LM4594) were prepared to investigate the effect of annealing temperature on QR formation. The typical structure, a single InAs active layer sandwiched

between two 150 nm GaAs barrier layers with a counterpart of InAs layer on the surface, was grown in each sample. For all the three samples, before exerting different capping techniques, the precursor InAs dots are formed with identical growth parameters (T_{sub} of 520 ^{o}C, 2.6 MLs of InAs, In_G.R. of 0.055 μm/hr, and ~1.3x10^{-6} Torr As_2 overpressure) followed by an interruption of 10 sec. For LM4594, after the QD growth, GaAs with 1 μm/hr growth rate was continuously deposited to entirely cover the dots. No additional annealing step was used. But for LM4593 (LM4592), after the dot growth was finished, the T_{sub} was ramped down to 450 ^{o}C (470 ^{o}C) within 100 sec for the following capping and annealing process: a thin GaAs layer of 2.5 nm was deposited with a growth rate of 1 μm/hr and then a 50 sec interruption under As_2 flux was performed at the same substrate temperature for annealing. Finally, the GaAs barrier layer with 1 μm/hr growth rate was grown to complete the growth process. Note that this high growth rate for GaAs barrier is essential to minimize the deformation of the as grown structures.

The AFM images of the three samples are shown in Fig. 3.4. We can see very clearly that after the capping and annealing process, the shape of the QDs was dramatically changed. The original QDs, shown in Fig. 3.4(a) and (a'), changed to a volcano-like structure (Fig. 3.4(b) and (b')) or a ring structure (Fig. 3.4(c) and (c')) depending on the annealing temperature. At a lower capping and annealing temperature of 450 ^{o}C, the outward migration of In atoms from the uncovered tip of each dot left behind a volcano shaped structure as shown in Fig. 3.4(b'). When the capping and annealing temperature was raised to 470 ^{o}C, more In atoms moved out of the dot leaving behind a deep crater in the center depleted of InAs. In this case, a complete ring was formed. It should be mentioned that the surface profiles in Fig. 3.4 have different elevations, or height references. In LM4594, with the dot profile shown in Fig. 3.4(a'), the QD stands on the WL and the whole dot is visible. For LM4593 and LM4592, however, the base height is elevated because of the cap layer coverage. Although the nominal deposition thickness of the cap layer was 2.5 nm, the base height was estimated to be ~3.4 nm due to the presence of

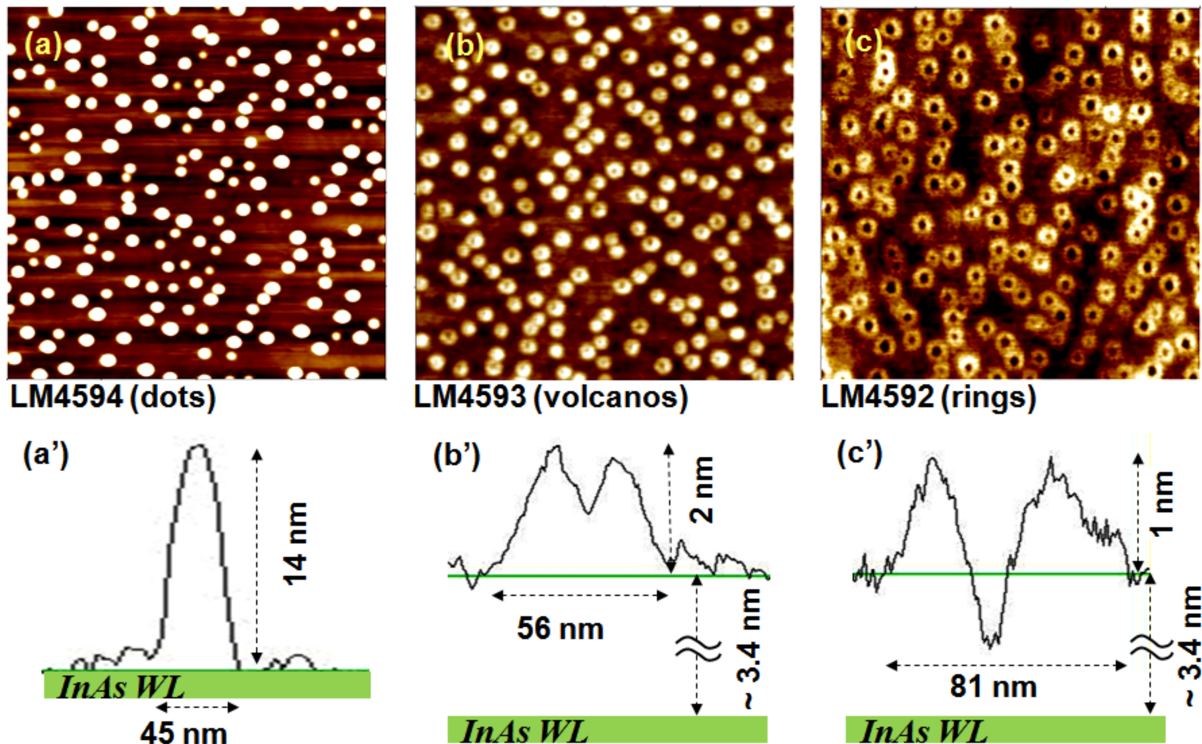

Fig. 3.4 The 1x1 μm^2 AFM images of (a) LM4594 (quantum dots), (b) LM4593 (quantum volcanos), and (c) LM4592 (quantum rings), and the representative surface profile of individual structure in each sample.

the QDs (Based on the size and density of the dots, 26% of the surface was occupied by the dots in the QD layer). So for these two samples, a large portion of the InAs volcanos and rings lies below the surface of the cap layer. The actual height of the volcano shown in Fig. 3.4(b') is 5.4 nm measured from the surface of the WL and the height of the ring shown in Fig. 3.4(c') is 4.4 nm.

If we look very closely at the surface image of LM4594 shown in Fig. 3.4(a), two groups of dots with different sizes are seen. Such bimodal size distribution is quite common in self-assembled QD growth [3.38]. It is because that at a given growth condition, there is an optimum number of nucleation sites and QD size. When the optimum size is reached, further deposition of In atoms will tend to form new nucleation and new dots (due to the attachment barrier around the edge of the old dots [3.39]). So the larger dots are the ones with the optimum size and the smaller ones are from the later nucleations. The typical size of the larger dots is

shown in Fig. 3.4(a'). The height is around 14 nm and the base diameter is around 45 nm. For the smaller size dots, the typical height was measured to be ~9 nm and the diameter was ~38 nm (not shown). Now as these dots are covered by a thin cap layer, the uncovered portion of the dots is different depending on the size of the dots. Obviously the larger ones have a larger portion exposed and the smaller ones have a smaller portion exposed. When the samples are annealed, these two types of dots evolve into rings differently. A closer look at Fig. 3.4(b), which underwent 450 ^{o}C capping and annealing, indeed reveals two groups of dots, one with a small depression at the center and the other without. Fig. 3.4(c) of LM4592, annealed at a higher temperature of 470 ^{o}C, also shows two groups of rings with two different sizes.

The PL emission spectra of the three samples described above are shown in Fig. 3.5. The excitation power was purposely kept low to ensure only ground state emission is allowed. The bimodal distribution of the QDs in LM4594, which was not annealed, is clearly seen with two emission peaks. After annealing at 450 ^{o}C, the emission peak of LM4593, shifts to a higher energy. Although it appears to be only a single peak, a careful fitting with Gaussian curves reveals there are actually two Gaussian distributions (see dash-line curves), a higher sharp peak

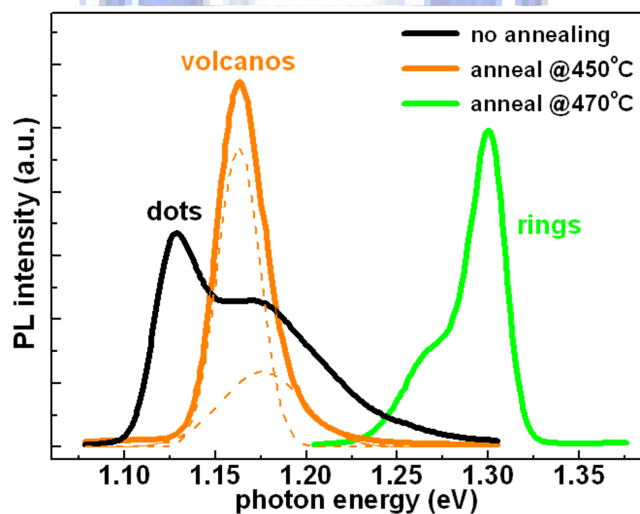

Fig. 3.5 The PL spectra of LM4594 (no annealing), LM4593 (anneal at 450 ^{o}C), and LM4592 (anneal at 470 ^{o}C) under low excitation power (~1 W/cm^{2}) at 13K.

at 1.163 eV with a FWHM of 27 meV and a lower broad peak at 1.176 eV with a FWHM of 52 meV. We attribute the larger peak to the emission from the nano-volcanoes, which were evolved from the larger QDs. The shift in energy is readily understood because the height of the dots has been reduced as the nano volcanoes were formed (see Fig. 3.4(a') and (b')). The smaller peak was from the smaller dots. Because the emission wavelength of this peak is almost the same as that of the smaller dots in LM4594 (no annealing), it is most likely that there has not been any change in the shape of the dots. The inability to change shape suggests that their tips were not exposed but instead covered by the GaAs layer during the annealing step. The reason for the coverage is probably due to the poor mobility of the deposited Ga adatoms at the T_{sub} of 450 ^{o}C.

Further shift in emission peak to higher energy is observed for LM4592, which was annealed at 470 ^{o}C, due to further reduction in the height of the dots as rings are formed. Again two peaks are seen. The larger peak, at 1.301 eV, is originated from the rings evolved from the group of QDs with a larger size. The shoulder peak at a lower energy of 1.276 eV comes from another group of rings that are evolved from the original smaller QDs. These small dots, which were unchanged after 450 ^{o}C annealing, now have also changed to ring structures. The higher capping/annealing temperature causes the tips of the smaller dots also exposed due to the increased surface mobility of Ga atoms. Because a less amount of InAs is removed from the tip, the shift in energy of the emission peak is less than that of the larger rings.

Let us look carefully into Fig. 3.4(c). The larger rings, which originated from the larger dots, have also larger sizes in their craters (a crater depth of ~1.7 nm could be observed in Fig. 3.4(c')). For the smaller rings that originated from the smaller dots, the crater is not as wide and deep as that of the larger rings. So clearly, the ring formation is at an earlier stage comparing to the larger ones. In other words, the smaller dots, after being partially capped have smaller driving force for shape transformation than the larger dots. As will be described in the

following, this can be explained by the difference in the degree of surface tension imbalance for the different size dots as they are partially covered.

3.4-2 Effect of Cap Layer Thickness on the Ring Formation and the Formation Mechanism

As described above, the difference in the amount of cap layer coverage for the QDs with different sizes causes difference in the final ring structure. So to get a better picture of the effect of cap layer on the ring formation, we have also prepared another group of QD samples (LM4600~LM4602 and LM4641). In this group of samples, QDs with larger sizes were grown. 3.2MLs of InAs were deposited at a higher growth temperature of 540 ^{o}C and a lower growth rate of 0.033 μm/hr. Such growth condition also gave a better size uniformity for the QDs. After the QD growth was finished, the T_{sub} was ramped down rapidly to 505 ^{o}C for the following capping process. In LM4641, the continuous capping of GaAs was used for the QD reference. In the other samples, the partial-capping and annealing process was used for the QR formation. The cap layer thickness used was 5.5 nm, 4 nm and 2.5 nm for samples LM4602, LM4601 and LM4600, respectively. Following the deposition of the cap layer, the samples underwent 50 sec annealing at the same temperature of 505 ^{o}C.

The AFM images of these samples and the surface profiles of the representative individual nano-structures are shown in Fig. 3.6. As shown in these pictures, the QDs (Fig. 3.6(a) and (a’)) again transformed via volcanos (Fig. 3.6(b) and (b’)) to rings (Fig. 3.6(c), (c’), (d) and (d’)) after the capping and annealing process. However, this time the factor that determines the final shape of the ring structure is not the temperature but the cap layer thickness. The amount of In that migrates out from the center portion of the dots depends on the amount of coverage of the cap layer.

In LM4602, which had a thicker cap layer of 5.5 nm, the QDs turned into volcano-like

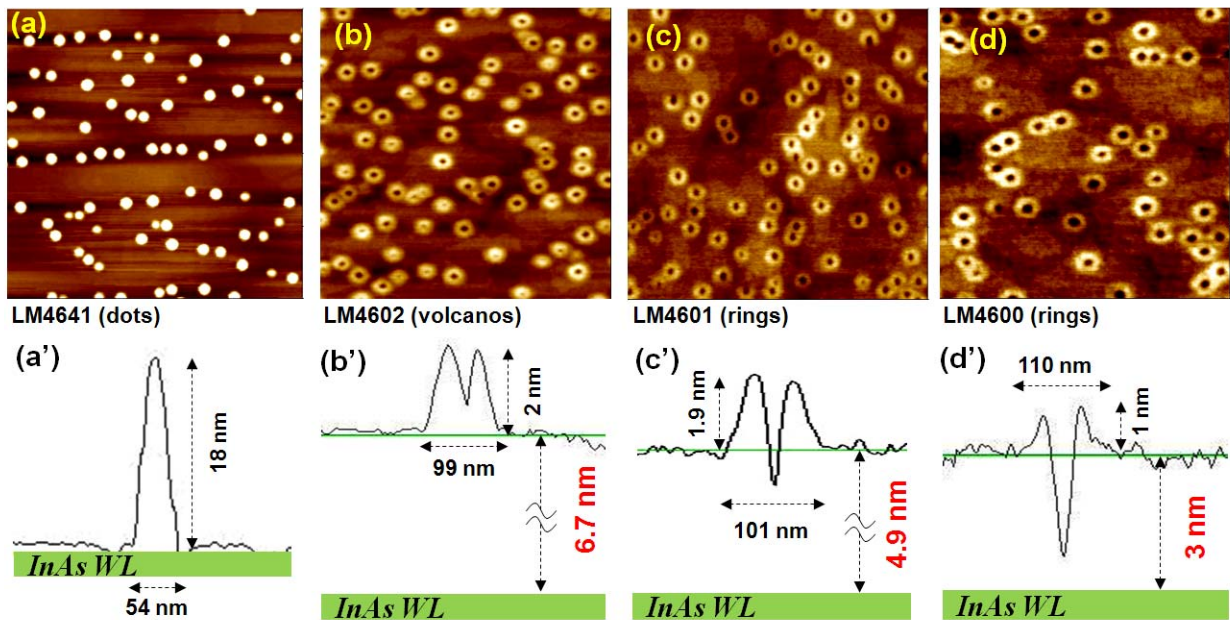

Fig. 3.6 The 1x1 μm^2 AFM images of (a) LM4641 (quantum dots), (b) LM4602 (quantum volcanos), (c) LM4601 (quantum rings), and (d) LM4600 (quantum rings), and the representative surface profile of individual structure in each sample.

structures with the center crater about 1.4 nm deep. The rim of the volcano was 2 nm above the GaAs cap, which was ~6.7 nm thick (based on 5.5nm deposition amount and 18% occupation of the surface by the precursor dots). So the height of the InAs volcano was about 8.7 nm, which is a great reduction from the original 18 nm height for the QDs. The InAs material that moved from the top of the dots spread out to the adjacent area above the GaAs cap. The base of the volcano that rose above the GaAs surface was widened to 99 nm. We need to bear in mind, however, the bottom base of the volcano underneath the cap layer should be still the same as that of the original QD. Judging from the AFM picture, this volcano structure is still far from a ring. However, for LM4600, which had a thinner cap layer of 2.5 nm, the final structure had a very deep hole with the In atoms almost totally depleted (see Fig. 3.6(d')). The rim of the ring was only about 1 nm above the cap layer. In other words most of the ring was buried below the GaAs cap, which was about 3 nm thick. The outer diameter of the rim reached 110 nm, which is much wider than the original base diameter of the QD. Although the ring-shaped geometries of the QRs had been undoubtedly revealed by the surface scan in Fig. 3.6(d) and (d'), the

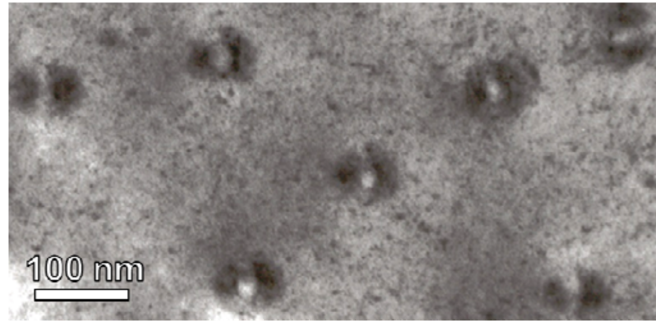

Fig. 3.7 The plan view TEM image of the imbedded QRs.

practical material distribution condition of the imbedded QR layer should be still verified with the TEM technique. Fig. 3.7 demonstrates such a plan view TEM picture (taken for LM4643, a sample with the growth parameters for QRs nearly the same as that in LM4600). The ring-shaped dark images confirm the ring-shaped accumulations of the InAs materials and somewhat the strain field of the QRs.

The PL spectra of the four samples described in Fig. 3.6 are shown in Fig. 3.8. Only one primary peak is seen for all the samples. Because of the growth condition chosen, we were able to get only one dominant size for dots. The emission peak continues to shift to higher energies

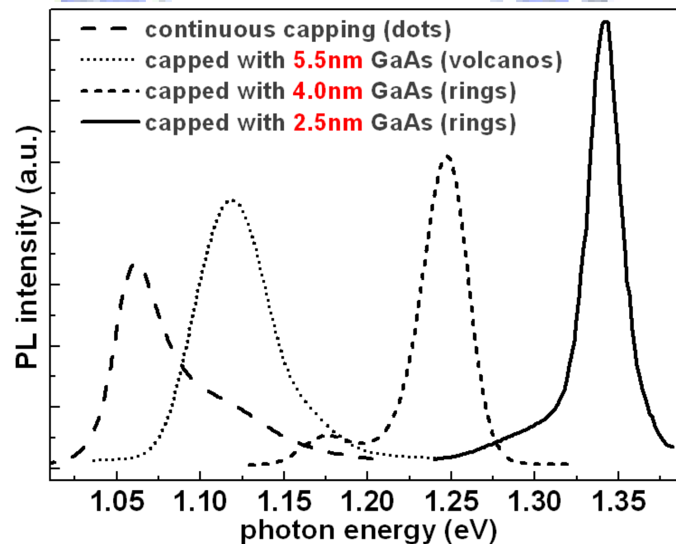

Fig. 3.8 The PL spectra of LM4641 (continuous capping), LM4602 (5.5 nm cap layer), LM4601 (4 nm cap layer), and LM4600 (2.5 nm cap layer) under low excitation power (~1 W/cm^2) at 13K.

as quantum rings are evolved from the original QDs due to the reduction of the height. The peak energy, E_0, changes from 1.061 eV for QDs to 1.342 eV for QRs. A vary wide range difference in E_0 (281 meV) was then achieved by such geometric manipulation for self-assembled dots. Moreover, the quantum ring formation is accompanied by a peak width shrinkage, which can be observed clearly from Fig. 3.8. The FWHM of the emission peak from the QDs decreases dramatically from 43 meV to 23 meV after the dots are transformed to QRs. This is attributed to a better uniformity in the height of the rings after annealing. Since the thickness of the cap layer should be very uniform, the fluctuation of the height of the original dots results in different exposed top areas. Subsequent annealing and the outward migration of InAs will tend to smooth out the original height fluctuation and cause the height of the final structure more uniform.

Since the QD sizes are the same for all the samples discussed here, the sample with a thicker cap layer will have a less amount of the exposed portion that can move outward upon annealing. Not only that, the migration of the In atoms from the tops of the QDs depends on the imbalance of the surface tension at the interface between the cap layer and the QD droplet. Based on this so-called dewetting model [3.29], it is not hard to picture that the driving force for the outward migration of In depends on how thick the cap layer is. Fig. 3.9(a) and (b) show the scenarios of a lens-shaped dot capped by a thicker GaAs layer and a dot capped by a thinner

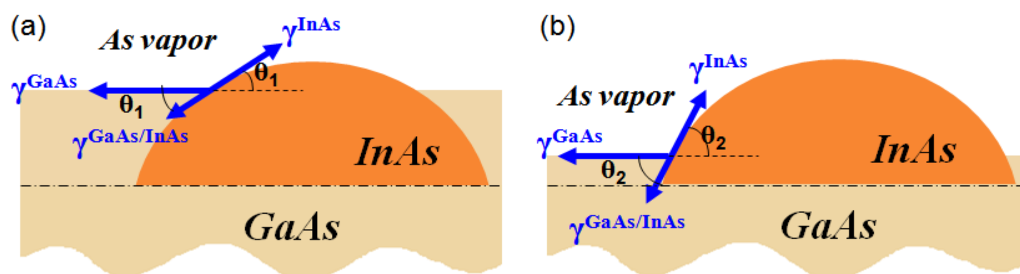

Fig. 3.9 Scenarios of a lens-shaped InAs island partially covered by (a) a thicker GaAs layer and (b) a thinner GaAs layer respectively. The three arrows indicate different interfacial tensions acting at the borders between GaAs, InAs, and As vapor.

GaAs layer, respectively.

Because of the curvature of the lens-shaped QDs, the net forces at the corner of the interface between the dot and the cap layer are different for these two situations. Let γ^{GaAs}, γ^{InAs} and $\gamma^{GaAs/InAs}$ denote the interfacial tension forces between GaAs and As vapor, InAs and As vapor, and GaAs and InAs, respectively. The net horizontal surface tension that pulls the InAs away from the dot would be

$$F = \gamma^{GaAs} - (\gamma^{InAs} - \gamma^{GaAs/InAs}) \cos\theta. \quad (3.1)$$

As a result of these imbalanced forces, InAs is pulled away from the tips of the dots to form volcanos or rings (note that $\gamma^{GaAs} > \gamma^{InAs} >> \gamma^{GaAs/InAs}$ is used here [3.40]). The reason why the removal of InAs materials is primarily from the tip of the dot can be attributed to its weaker binding force than that of the surrounded rim. Based on equation (3.1), the pulling force depends on the interface angle θ. As Fig. 3.9 shows, θ is larger as the cap layer is thinner. So the force that exerts on the dots is increased when a thinner cap layer is used. In other words, more InAs will be pulled out of the centers of the dots to the surrounding areas. Comparing to the case with a thicker cap layer, the crater is deeper and the base of the rim is wider. This explains why different volcano or ring structures are obtained when cap layer with different thicknesses are used.

In addition to the four samples described above, another sample (LM4599) with an even thinner cap layer (only 1 nm) in the capping/annealing process was also prepared for the AFM and PL studies. The results are shown in Fig. 3.10. As shown in Fig. 3.10(a), disk-like QDs rather than ring-shaped structures are seen. As the inset shows, the diameter of the QD is about 62 nm and the total thickness of the dot is about 2.6 nm (again, the 18% surface occupation by QDs was used to estimate the base height). Although an even thin cap layer was used to tailor the geometry of the dots, ring structures were not obtained. We attribute the reason to be: for the GaAs cap layer with such a thin thickness, the region with In-Ga intermixing due to the In segregation [3.41] from the wetting layer becomes not negligible. In this case, the surface

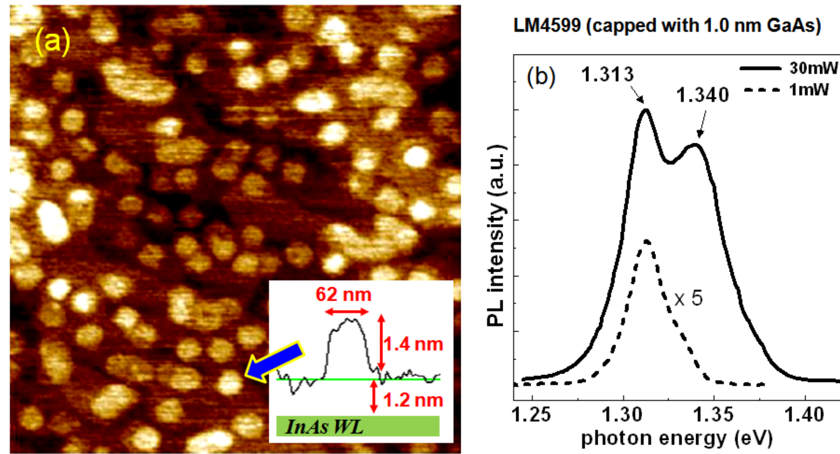

Fig. 3.10 (a) The AFM image and (b) the PL spectra with different excitation power at 13K of LM4599. The inset in (a) shows the surface profile of the InAs dot pointed by the arrow.

tension of the cap layer is reduced so that the net outward force for pulling InAs dots instead decreases. Consequently, the driving force is so small that it cannot tear the tips of the InAs dots into crater-like structures to form rings. Judging from the power dependent PL spectra shown in Fig. 3.10(b), the E_0 is 1.313 eV and the first excited state emission energy, E_1, is 1.340 eV. The high ground state energy is due to the small QD height, and the small energy separation between E_0 and E_1 is due to the small height-to-width aspect ratio for QDs [3.42].

Let us compare with the geometry and the ground state transition energy for the sample LM4600 with deep-crater rings and the sample LM4599 with disk-like dots. The rim thickness of the ring in LM4600, which is ~4 nm (see Fig. 3.6(d')), is larger than the thickness of the dot in LM4599, which is ~2.6 nm (see Fig. 3.10(a)). However, the ground state energy of the QRs in LM4600 (1.342 eV) is instead higher than that of the dots in LM4599 (1.313 eV). This fact suggests that, for the QR with the volcano-like geometry, the dominant factor determining the ground-state confinement energy lies in the condition of the center crater but not the thickness of the peripheral hump. In the following, the influence of the crater formation on the electron energy states in a volcano-like QR will be studied by modeling and calculation.

3.4-3 Effect of Crater Depth on the Single-particle Electron States in a Volcano-like Quantum Ring

The QD was modeled as a cone-shaped structure standing on a thin wetting layer. The transformation of the QD into the volcano-like QR, is then modeled by digging down through the tip of the cone. The modeled geometry is defined in cylindrical coordinate with azimuthal symmetry shown in Fig. 3.11(a). The center height of the structure, h, is the variable for simulating dot-to-ring evolution. The one-band Hamiltonian with material-dependent effective mass approximation was used to calculate the single-particle electron states [3.43]. We used the commercial software, COMSOL, to solve this 3-D Schrodinger equation using finite difference method. The constant-confining-potential model was used here and the input parameters such as potential well depth (V_0) and effective mass (m_e) in each domain were quoted from Ref. 3.44 where the effect of the local strain has been included. Assume 85% In composition in QDs (QRs) to account for the intermixing effect, we assign the parameters as follows: $V_0 = 356$ meV, m_e (InAs) = $0.05m_0$, m_e (GaAs) = $0.067m_0$, where m_0 is electron mass. Also illustrated in Fig. 3.11(a) is the formulation of the electron wavefunction. Because of the azimuthal symmetry, the azimuthal part of the wavefunction can be treated independently, generating the quantum number m, which is associated with the orbital angular momentum along z-direction. The radial part (for both z-axis and r-axis) of the wavefunction gives the other quantum number n. Hence, the electronic state excluding spin is designated by (m, n) in this calculation.

The calculated energy levels of the low-lying electron states are plotted as functions of h in Fig. 3.11(b), where h is the intersection between the z-axis and the InAs domain illustrated in Fig. 3.11(a). From Fig. 3.11(b), it is observed that when h is reduced, the energies of the (0, 0), (0, 1) and (±1, 1) states are raised with the speeds higher than the other states. When h is reduced to significantly lower than 6.15 nm, i.e. a ring-like structure emerge (see the geometry defined in Fig. 3.11(a)), the energy separation between (0, 1) state and (±2, 0) states and that between (±1, 1) states and (±3, 0) states, which are both negligible at the high end of h, become

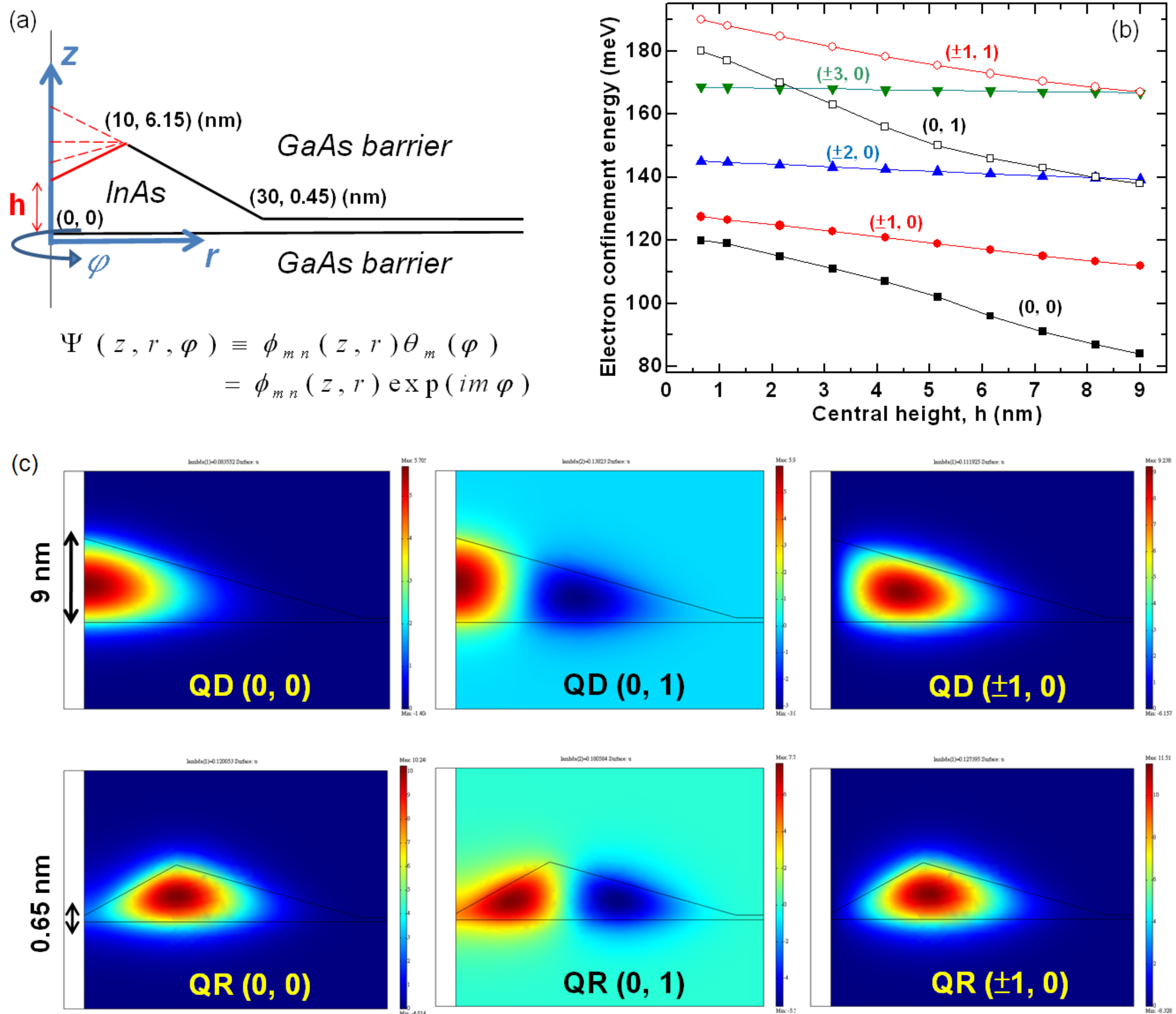

Fig. 3.11 (a) Half of the side-view cross-section of the volcano-like structure illustrating the evolution from QD to QR and the formulation for the time-independent eigenstate wavefunctions. (b) The calculated electron energies of the low-lying states as functions of volcano's center height, h. (c) 2-D plots of some electron wavefunctions of the QD (h = 9 nm) and the QR (h = 0.65 nm).

very prominent. Hence, we can get some observations if we make comparisons for the two extremes of h: First, as the QDs (h = 9nm) are evolved into QRs (h = 0.65nm), the original quasi-degeneracy in QDs will be removed apparently in QRs. Second, with the QR formation, more than one states with non-zero angular momentum (such as (±1, 0), (±2, 0), (±3, 0), etc.) will appear between the (0, 0) state and the (0, 1) state in the energy axis. Last, compared with the QDs, the electronic state energies increase but the energy separations shrink for the QRs.

In order to clarify these observations, the wavefunctions of the (0, 0), (0, 1), and (±1, 0)

states in QDs (h = 9nm) and QRs (h = 0.65nm) are plotted respectively in Fig. 3.11(c). In QDs, for the states with zero orbital angular momentum, i.e. (0, 0) and (0, 1) states, the maximum of the wavefunctions all occur at the center of symmetry (z-axis) despite the difference in the number of "zeros" in r-direction. For the (±1, 0) state, which has non-zero angular momentum, the wavefunction tend to accumulate away from the center of symmetry at the cost of the elevation in total energy. In the case of QRs, the wavefunctions of (0, 0) and (0, 1) states, despite zero angular momentum, are pushed away from the center of symmetry by the potential barrier at the center. For that reason, the state energies of (0, 0) and (0, 1) are significantly elevated. As for the (±1, 0) state, the influence of the center barrier of the QR is less evident because the wavefunction of the state with non-zero angular momentum naturally tends to accumulate out of the center. Such argument holds for all (±m, 0) states in QRs. In fact, the influence of the center barrier is even weaker for the higher-lying (±m, 0) states as the wavefunctions locate more distantly from the center. As a result, the energy separations of the electron states in QRs are smaller than in QDs. The simulation results also explain the experimental observation in the last sub-section. For QRs, the deeper the center crater is, the outer the ground state wavefunction will be pushed, so the higher the ground state energy will be. It is the central thickness of the ring rather than the rim height of the ring that dominantly determines the ground state energy of QRs.

The quasi-degeneracy between the (0, 1) state and the (±2, 0) states in QDs (as calculated for the high end of h in Fig. 3.11(b)) was further confirmed by the magneto-PL spectroscopy. The QD sample RN0069 (which has been described previously in section 3.3) was chosen for examination here. The sample was inserted in a magnet-surrounded dewar cooled by liquid helium. The magnetic field was perpendicular to the sample surface with the intensity adjustable from 0 T (Tesla) to 14 T. The photo-excitation and the signal collection are performed by coupling through an optical-fiber bundle to the pumping laser and the monochromator, respectively. The supplied excitation power density was about 0.8 W/cm^2.

Despite such low power density, the PL spectrum revealed clear state-filling characteristics due to the ultra-low dot density of the sample. Fig. 3.12 shows such spectra with the magnetic field changed from 0 T (bottom) to 14 T (top). It is clearly observed that the first two excited-state transition peaks (p-shell and d-shell) at 0 T evolves into five different peaks (guided by dash-lines) with increasing magnetic field due to the orbital Zeeman splitting as well as diamagnetic shift [3.45]. The originally undistinguishable (0, 1) state and the (±2, 0) states in d-shell is clearly separated when the magnetic field is higher than about 10 T. Because of the dipole-allowed transition selection rule, the PL emissions are dominated by the recombination of the electrons and holes from the respective shells of the same quantum numbers. So the resolved three features split from the d-shell peak in Fig. 3.12 indeed confirm the previous calculation for electron states.

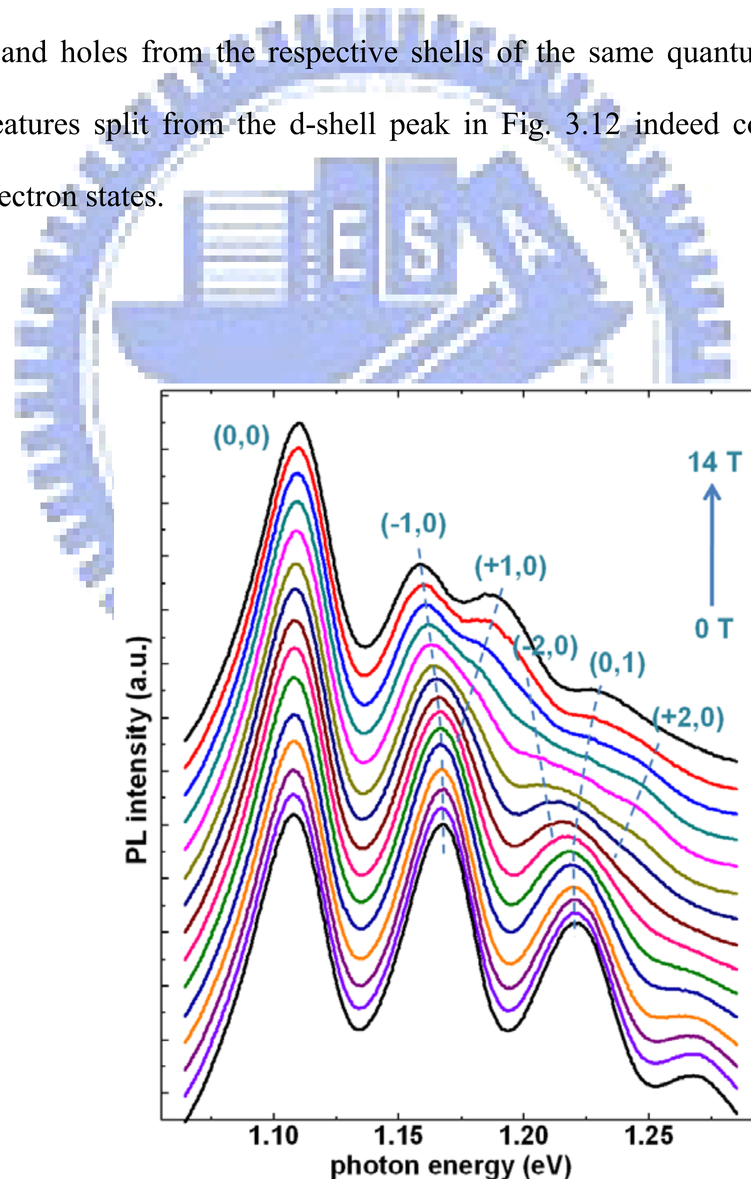

Fig. 3.12 The PL spectra of the QD sample at 1.5K in magnetic field perpendicular to the sample surface.

3.5 High Density Quantum Rings with Strong Photoluminescence Emission at Room Temperature

As described in the last section, the geometry of the QRs depends critically on the cap-layer thickness and the annealing temperature. By controlling the amount of In migration at the annealing step and then continuously depositing GaAs with high growth rate to "freeze" the as grown InAs morphology, the shape of the quantum rings can be controlled. Because the ring formation has such a kinetically controlled growth property, we have another freedom to control the ring evolution, i.e. the annealing duration. In fact, high annealing temperature along with short annealing time can give the same stage of ring evolution as low annealing temperature with long annealing time does. Despite obtaining identical ring morphology, the former growth condition commonly makes the quality of the epilayer better, especially for the subsequently grown GaAs barrier layer, which should be grown at high enough temperature for high quality epitaxy. Also, in point of the growth of multi-layer QRs, another concern is the stable control on substrate temperatures, for both the precursor QDs and the subsequent ring evolution are very sensitive to the substrate temperature. In this case, using identical substrate temperature for both the QD growth step and the capping/annealing step without any temperature ramp is preferred. For that reason, the effect of annealing time on the QR formation was also investigated, with a substrate temperature of 520 ^{o}C throughout the growth of the QR layer. Two samples were studied, both with 2.8 MLs of InAs at the growth rate of 0.056 μm/hr and 2 nm of GaAs cap layer for ring formation. One (LM4729) was annealed with 5 sec while the other (LM4693) was annealed with 30 sec. Their AFM images and PL spectra are compared in Fig. 3.13. For the sample with 5 sec annealing, clear ring-shaped structures are seen (Fig. 3.13(a)), and the ground state energy is at 1.204 eV (Fig. 3.13(c)). While for the sample with a longer annealing time of 30 sec, structures with the larger crater-like holes as well as the smeared outer rims are observed in Fig. 3.13(b). The ground-state emission peak, as expected, shifts to a higher energy, at 1.289 eV (see Fig. 3.13(c)). The borders of the QRs being

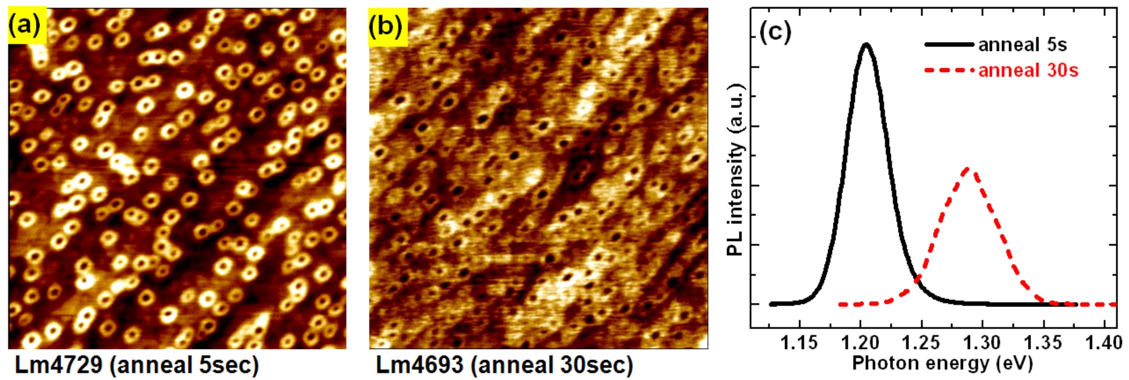

Fig. 3.13 (a),(b) The 1x1 μm^2 AFM images and (c) the PL spectra at 13K of the QRs with different annealing duration for ring formation.

smeared indicates that the outward migration of In adatoms is so distant that the overlap between each QR occurs. Thus, an annealing duration of 30 sec is definitely too long for growing isolated QRs. From Fig. 3.13, it is observed that the sample with isolated rings in the QR layer has stronger PL emission as well as narrower emission line-width than the sample with overlapped QRs.

It should be mentioned that for the surface QR layer, the migration of In adatoms cannot be quenched instantly after the annealing step is finished due to the finite heat capacity of the substrate holder. For the case where short duration of high temperature annealing is used for QR growth, over-estimation on the ring evolution for the imbedded QRs may be significant if we refer to the morphology of the surface rings. Hence, for the samples studied in this section, in order to make the surface QRs resemble the imbedded counterpart as good as possible, the substrate temperature was additionally ramped down by 20 ^{o}C before the capping/annealing process for the surface QR layer.

Finally, with the optimum growth parameters (2.8 MLs InAs, 0.056 μm/hr, T_{sub} of 520 ^{o}C, 2 nm GaAs cap layer, and 10 sec annealing time), high density QRs with good optical quality were obtained via this dot-to-ring shape engineering. The power-dependent PL spectra taken at room temperature and the 3-D AFM pictures are shown in Fig. 3.14 for both the InAs QDs ((a) and (a')) and its transformation, InAs QRs ((b) and (b')). Due to the excellent epitaxy quality

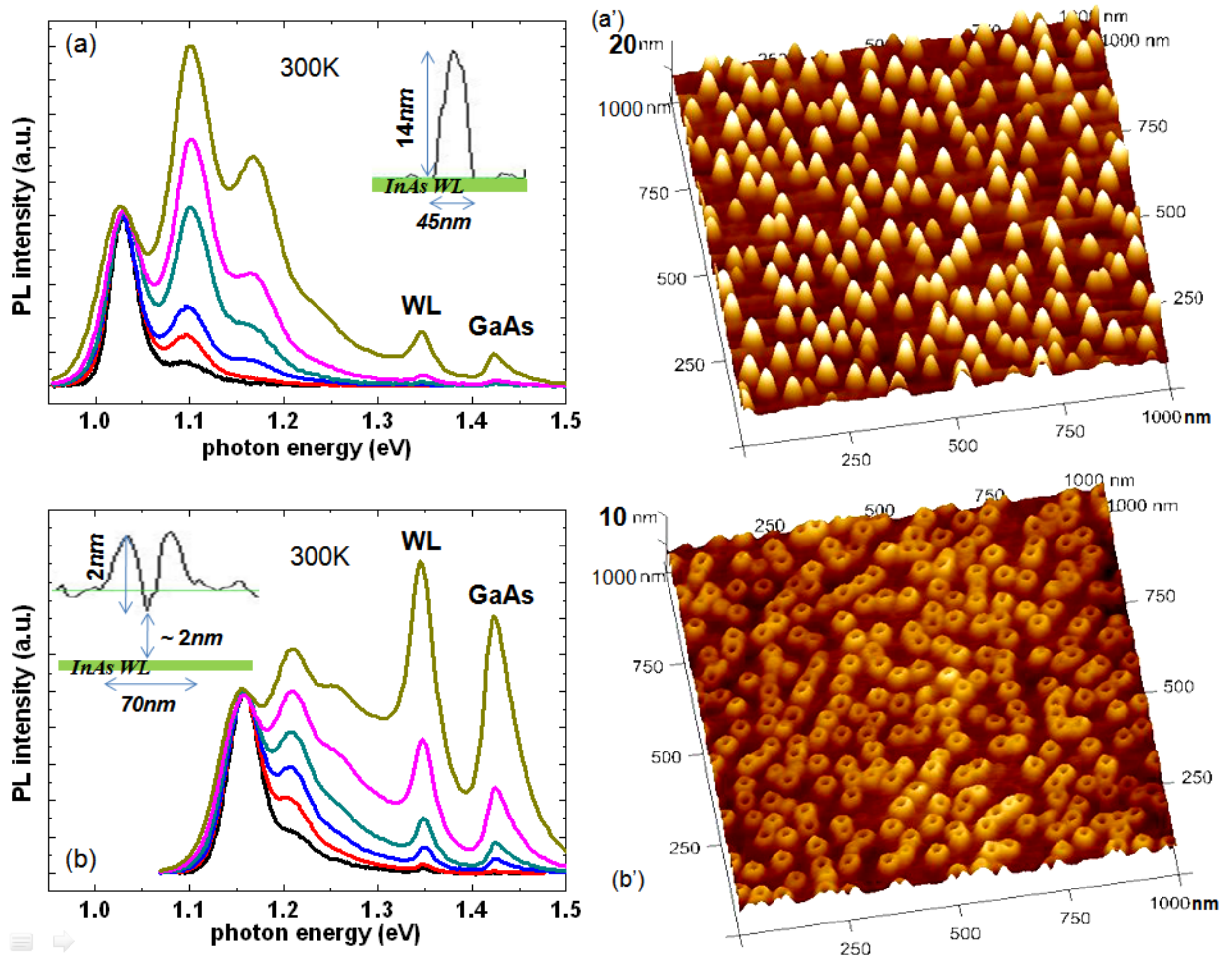

Fig. 3.14 The power-dependent PL spectra with normalized ground-state peak intensity of (a) QDs and (b) QRs. Also illustrated in the inset is the representative surface profile of a single structure. At the right hand side are the 3-D AFM images of (a') QDs and (b') QRs.

obtained, both the QDs and QRs show strong PL signals at room temperature. The emission signals due to the higher-lying shells of the QDs/QRs appear sequentially as the excitation power is raised. For QDs, the E_0, E_1, E_2 and E_3 are at 1.028eV, 1.101eV, 1.169eV and 1.237eV, respectively. While for QRs, because of the reduced center thickness and widened lateral dimension, the E_0, E_1, E_2 and E_3 blue-shift to 1.159eV, 1.210eV, 1.253eV and 1.297eV respectively. Besides the discrete states of QDs or QRs, the signal of the WL also appears under high excitation power. The WL ground-state energy locates at about 1.348eV for both the two samples, indicating after the annealing process the thin GaAs cap layer only modifies the electronic structure of the InAs islands but by no means affects the imbedded wetting layer.

Judging from the AFM image, the QRs have well defined outer peripheries and the sizes are quite uniform. The sheet density is also very high, reaching $2.6x10^{10}$ cm^{-2}. The QR condition obtained here is very promising for fabricating photonic devices with the QRs as the active media, such as quantum ring infrared photodetectors, which will be described in chapter 7.

3.6 Summary

We investigated the growth conditions of self-assembled InAs/GaAs QDs to get wide ranges of sheet densities. The dot densities ranging from $\sim 1x10^{8}$ cm^{-2} to $\sim 1.2x10^{11}$ cm^{-2} were achieved by adjusting the growth parameters and the growth procedure. We also studied the formation mechanism of self-assembled InAs QRs in GaAs matrix obtained by the partial-capping and annealing process. The gradual transformation from QDs to QRs was captured by the AFM surface scan and the PL measurement. The process depends on the annealing conditions and the cap layer thickness. The imbalance of surface tensions at the interface between InAs QDs and the cap layer provides the driving force for the outward migration of the InAs from the tips of the dots to the surrounding areas. The outward driving force depends on the interface angle and thus the cap layer thickness for the QDs with the lens shaped geometry. A thinner cap layer, because of a larger angle, results in a larger driving force and therefore more matured rings with deeper center craters. The annealing temperature provides the thermal energy needed for the migration of InAs. The annealing duration also determines the migration length of InAs. By controlling these growth parameters, we were able to manipulate the geometries and therefore the electronic properties of 0-D quantum structures by the way of self-assembly. By solving effective mass based Schrodinger equation, we found that the formation of the ring-like potential inhibits the wavefunctions from accumulating to the ring center so that the state energies are raised while the energy separations are reduced. With optimized growth conditions, we have realized high density InAs QRs with uniform size and strong room temperature PL emission that are very promising for device applications.

Chapter 4

Energy-dependent Carrier Relaxation in Self-assembled InAs Quantum Dots

In this chapter, selective excitation PL (SEPL) spectroscopy is employed to study InAs/GaAs self-assembled QDs. Under different excitation energies, different groups of QDs are selected and then emit light. The excited carriers relax to the ground state through different mechanisms when excited at different energies. Three distinct regions with different mechanisms in carrier excitation and relaxation are identified in the emission spectra. These three regions can be categorized from high energy to low energy, as continuum absorption, electronic state excitation, and multi-phonon resonance. The special joint density of state tail of the QD that extends from the wetting layer bandedge facilitates carrier relaxation and is posited to explain these spectral results.

4.1 Introduction to the Selective Excitation Photoluminescence Spectroscopic Studies on Carrier Relaxations

As mentioned in the last chapter, self-assembled QDs in the $In_xGa_{1-x}As$/GaAs material system achieved by S-K growth mode are very promising to serve as the active media of the photonic devices, including QD laser diodes and QD infrared photodetectors. For both devices, the carrier relaxation in QDs plays a crucial role in the operation mechanisms. It governs the light-emission efficiency for the QD lasers and determines the carrier life time for the QD photodetectors. On the other hand, the coupling condition between carriers (ether for electrons or excitons) and phonons as well as the associated relaxation dynamic in localized systems is itself of physical interest [4.1-4.2]. In particular, the fascinating anti-crossed dispersion

relations of the so-called polarons have been evidenced by the magneto-spectroscopy of the InAs/GaAs QDs recently [4.3-4.4]. Such experimental results confirm the theoretically concerned strong coupling regime, where the electronic states of the QD system are entirely altered by the lattice vibration. In that case, the concept of the Fermi-golden rule is no longer adequate but a more complete, nonperturabative approach should be employed. Hence, the relaxation mechanism of carriers in such systems with discrete density of states is indeed an important subject. Numerous efforts have been made in this area using various spectroscopic approaches [4.3-4.15].

Despite the evidence of the polarons, the concept of weak coupling approximation still applies to most experiment results under zero magnetic fields [4.5-4.15]. Based on the Fermi-golden rule, the energy relaxation of carriers in QDs cannot be simply achieved by the interaction between carriers and acoustic phonons because of the large separation between quantized energy levels. Such a restriction slows down the relaxation of electrons/excitons to be slower than the radiative recombination, leading to the so-called "phonon bottleneck" effects [4.16-4.17]. Other channels such as Auger-type scattering [4.18] and/or multi-optical phonon scattering [4.19] are required to bypass the phonon bottleneck to enable the relaxation process.

The carrier relaxation through multi-optical phonon scattering can be studied using photoluminescence (PL). The discreteness of the phonon energy and the inhomogeneity in the quantized energy levels of the QDs support the application of the selective excitation PL (SEPL) or PL-excitation spectroscopy (PLE) techniques to probe the energy spectrum of selected QDs and examine the carrier relaxation process, even though these approaches are basically time-independent.

Carrier relaxations both with and without multi-optical phonon "filtering" have been observed [4.6-4.15]. These two behaviors can be distinguished in the spectra because of the difference between the characteristics of the relaxation mechanisms. Without multi-phonon

filtering, the SEPL or the PLE spectra should reveal information on the energy levels of the QDs selected by resonant excitation. In contrast, if the relaxation undergoes multi-phonon filtering, such that only the QDs with relaxation energies equal to multi-phonon energies can emit light, then the spectra instead reveal certain longitudinal optical (LO) phonon replicas. For those filtered out QDs, which do not satisfy multi-phonon energy conservation, the excited carriers cannot relax to the ground state but are depleted either through non-radiative recombination [4.15] or through excited-state emission. The two aforementioned phenomena have been observed from different samples by different research groups [4.6-4.15]. However, the inter-relationship between these two phenomena, and the detailed mechanism of the efficient carrier relaxation between QDs' discrete states that bypasses LO phonon filtering, are still unclear.

In the following, we describe the observation from a single sample that the carrier relaxation with and without LO phonon filtering are both revealed under different excitation energies. For the first time, this energy-dependent relaxation mechanism is investigated and explained.

4.2 Sample Growth and Basic Characterization

The QD samples used herein were grown using our MBE system on (001) n+ GaAs substrates. Two samples with InAs/GaAs QDs of different sizes were investigated. They were both grown with the typical layer structure, i.e. a single active QD layer sandwiched between two 150 nm GaAs barrier layers with a counterpart of QD layer on the surface for AFM measurement. In sample A (RN0083), large QDs were purposefully grown. 2.6MLs of InAs with a 0.056 μm/hr growth rate were deposited at 505 ^{o}C (~525 ^{o}C if compared to the LM-series samples) under $3x10^{-6}$ Torr As_2 overpressure (the cracking zone of the As cell was set at 840 ^{o}C). However, for sample B (LM4455), ultra-small QDs were prepared with 2.4MLs of

InAs grown at a rate of 0.1 μm/hr and a lower growth temperature of 480 ^{o}C. As_4 atmosphere (the cracking zone was lowered to 500 ^{o}C) at a pressure of $1.5x10^{-5}$ Torr was used to minimize the probability of coalescence of the QDs. The layers except the regions near QDs were grown at around 600 ^{o}C to ensure the growth of high-quality epi-layers.

The AFM measurement was achieved by a commercial machine using the tapping mode scan. Fig. 4.1 and Fig. 4.2 present the AFM images and the surface profiles of sample A and sample B, respectively. The AFM data reveal that the QDs in both samples have lens-shaped geometry. For sample A, the typical QD height is 9 nm, the base diameter is 47 nm, and the sheet density of the dots was about $2x10^{10}$ cm^{-2}. In sample B, the QDs are very small and dense, but they still look quite uniform in size (see Fig. 4.2). The measured dot height and base diameter was about 1.5 nm and 17 nm respectively; the density reached $1.2x10^{11}$ cm^{-2}.

The SEPL or the PLE spectra of the QDs were measured using a Ti-sapphire laser that was pumped with an argon ion laser, while the conventional PL (or non-resonant PL) spectrum was obtained directly using the argon ion laser. The samples were mounted in a helium close-cycled cryostat for low-temperature measurements. The emission signal of the sample was transferred through air space, dispersed by a 0.85m double-grating monochromator (rather than the 0.55m single-grating monochromator shown in Fig. 2.6), and then detected by a thermal-electric cooled InGaAs photodiode. Lock-in technique was used to improve the signal-to-noise ratio,. Since the QDs in these two samples are of different sizes, the samples exhibit different ground state transition energies. At 13K, the measured peak energies for samples A and B were at 1.168 eV and 1.269 eV, respectively.

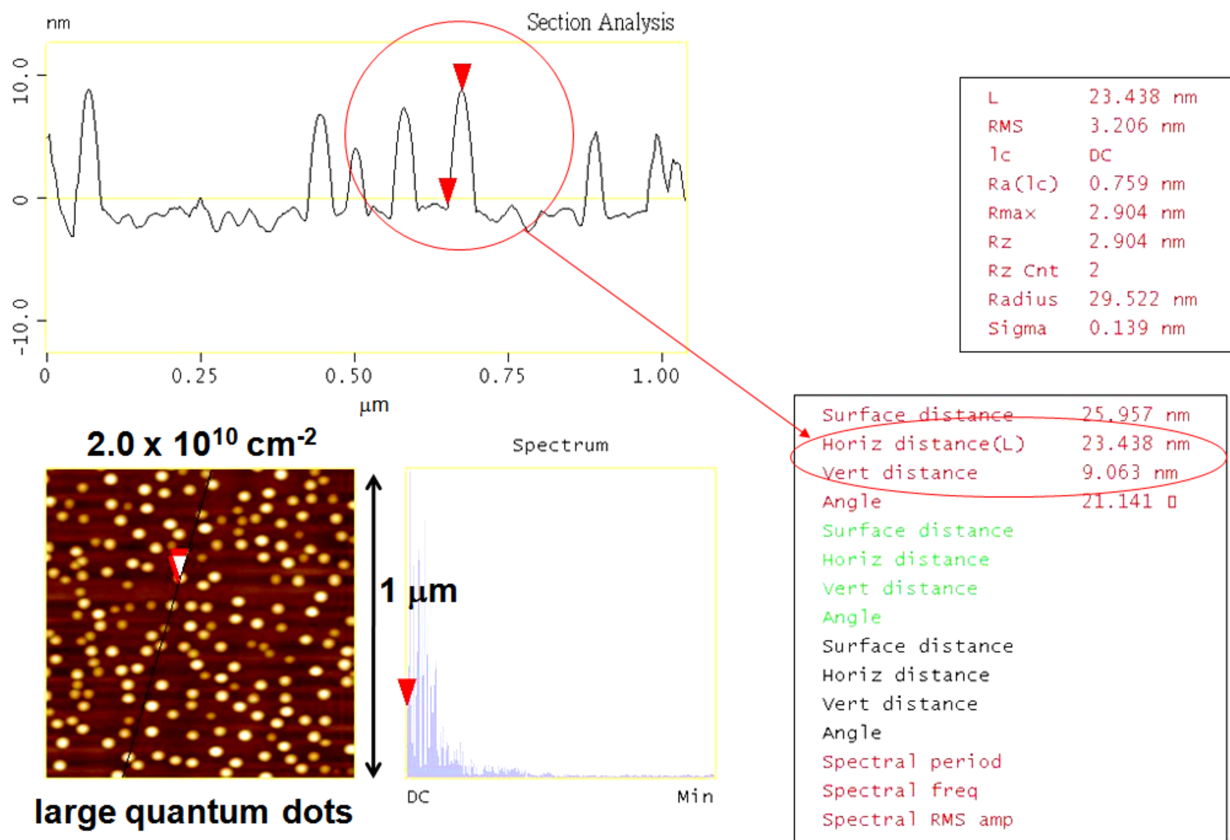

Fig. 4.1 The 1x1 μm^2 AFM image and the surface profile of large QDs (sample A).

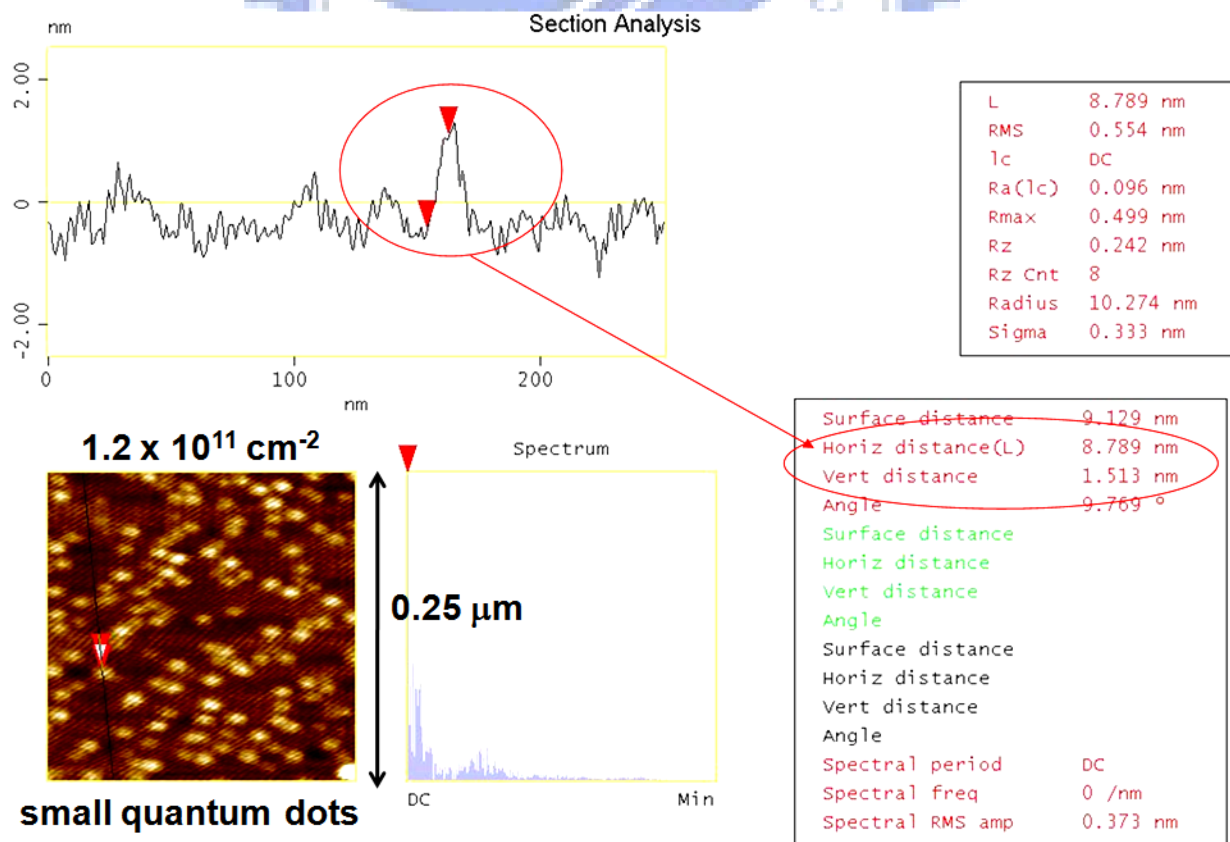

Fig. 4.2 The 0.25x0.25 μm^2 AFM image and the surface profile of small QDs (sample B).

4.3 Discussion for Large Quantum Dots: Electronic State Relaxation and Optic-phonon Filtered Relaxation

The SEPL spectra of sample A, shown in Fig. 4.3, were obtained as the excitation energy was varied from 1.378 eV to 1.211eV. (The spectra are arranged with decreasing from top to bottom.) The excitation energy for each spectrum is marked by a cross on the right-hand side. All excitation energies were below the wetting layer (WL) ground state energy (which was approximately 1.45 eV, as determined from the high-power PL spectrum shown in the inset) to ensure that only the QD layer could absorb the pumping photons. The excitation power was around 1 W/cm^2, which was purposely chosen to be low enough to avoid any emission from an

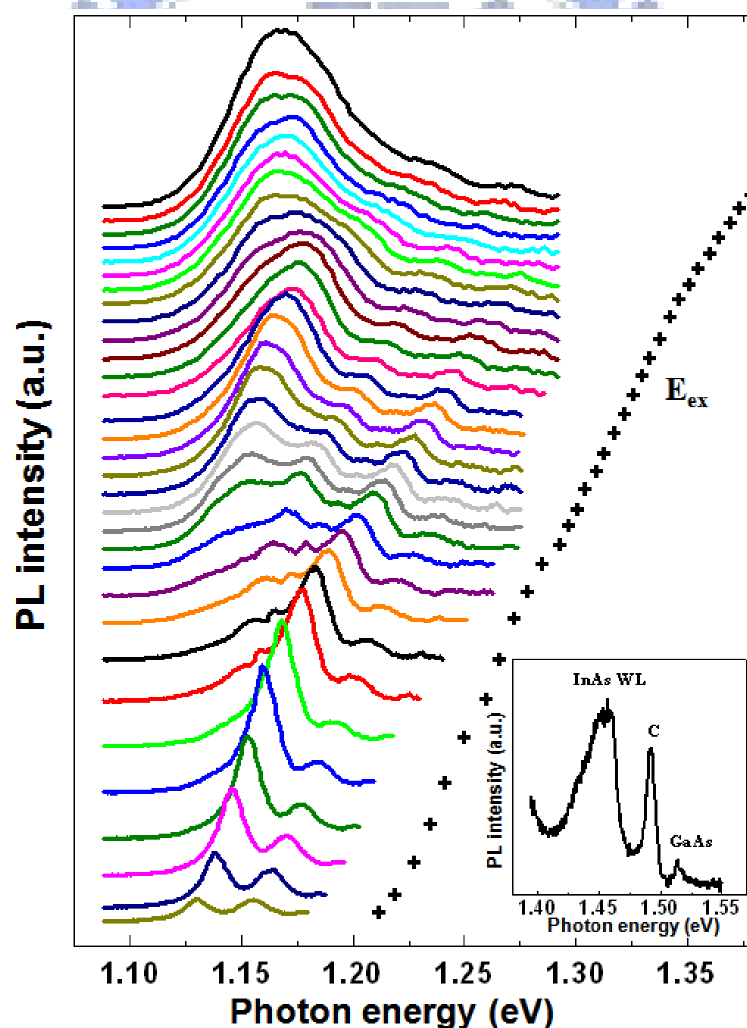

Fig. 4.3 SEPL spectra of large QDs (sample A) obtained at 13K. The cross on the right-hand side of each spectrum indicates the excitation energy. The inset shows the high-power PL spectrum.

excited state and to reduce the possibility of Auger scattering. When the excitation energy (E_{ex}) exceeds 1.34eV, the luminescence spectra show a broad peak, indicating that all QDs are excited. As the excitation energy decreases, fine structures with narrower peaks are observed, because of the selective excitation of QDs with specific sizes that allow carrier relaxation through discrete energy levels.

The spectra obtained in Fig. 4.3 are better understood by plotting them as functions of relaxation energy, E_{ex} - E_{det} , which is the difference between the excitation energy and the emission energy of each QD. This plot, in Fig. 4.4, reveals three distinct regions. At the low end

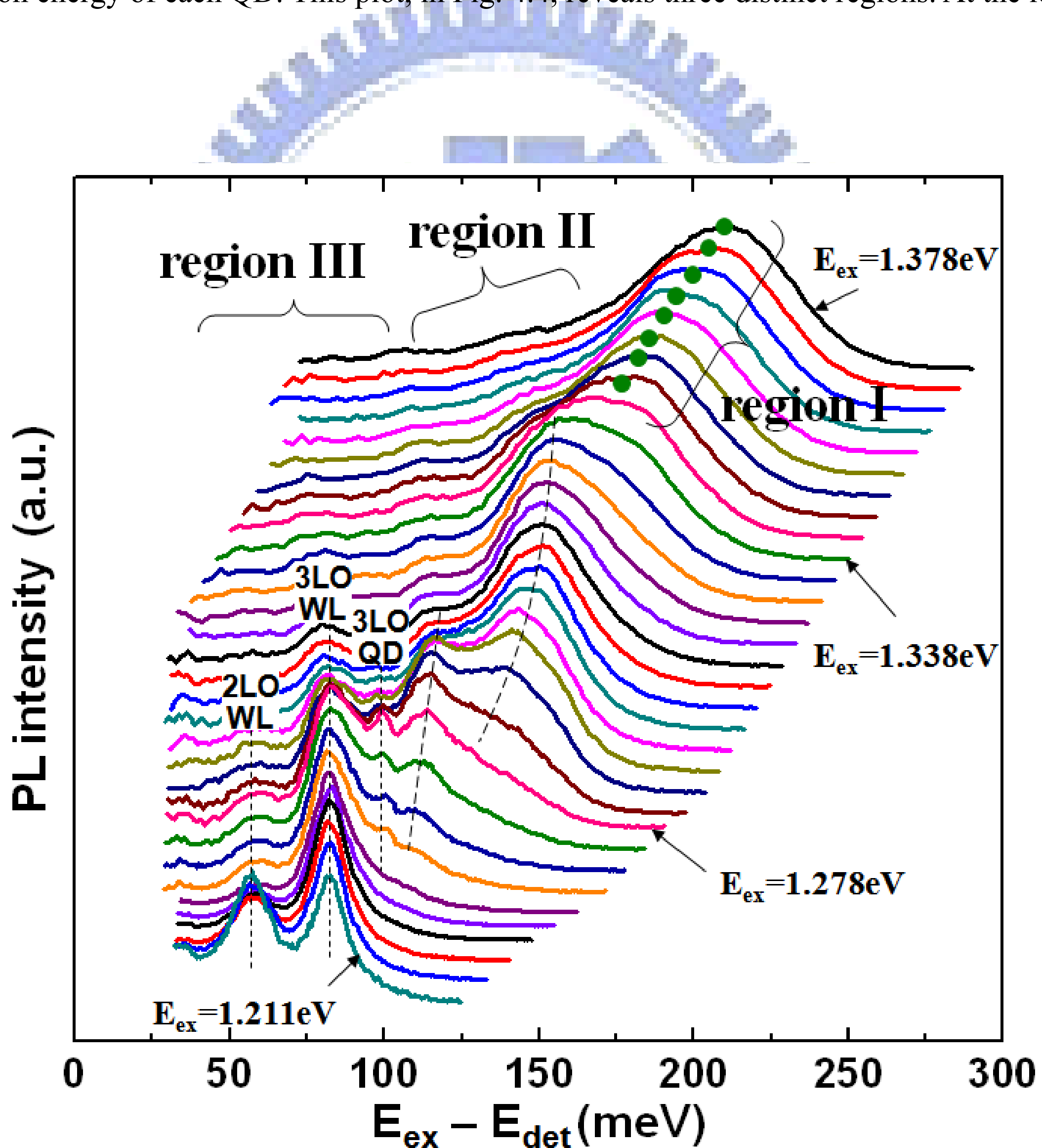

Fig. 4.4 SEPL spectra of sample A with the intensity normalized, exhibited as a function of relaxation energy ($E_{ex} - E_{det}$). The three regions I, II, and III correspond to different excitation and relaxation mechanisms.

of the excitation energy, the sharp peaks in the bottom few spectra line up vertically in the same positions. The peak values of E_{ex} - E_{det} correspond exactly to particular multi-LO phonon energies, suggesting that only the QDs with excited states at multiple phonon energies above their ground state are selectively excited. At the high end of the excitation energy, with energies of over about 1.338 eV, only one broad peak (indicated by the filled circle) is observed in each spectrum. These broad peaks have the same emission energy as in the conventional PL spectrum, suggesting that all the QDs are excited and participate in the light emission. When the excitation energy is in the middle range, a different excitation scheme is observed. Both the emission energy (Fig. 4.3) and E_{ex} - E_{det} (Fig. 4.4) of the selective excited QDs vary continuously with the excitation energy. The sharp peaks associated with selective excitation via a multi-LO phonon process are no longer there, but the broad emission peak observed at high excitation energies is also absent. As will be discussed in the following, the quantized energy levels in the selected QDs are responsible for the emission spectra in this energy range.

The three distinct regions in the PL spectra under various excitation energies are designated as regions I, II and III (from high to low energy). The origin of these three regions is explained by the different excitation and carrier relaxation mechanisms, as follows. The pioneering work of Toda *et al*. [4.20] demonstrated the existence of a continuum of tail states below the WL band edge in the PLE spectrum of a single QD. Vasanelli *et al*. explained that a such broad band is the result of the crossed transitions between the discrete states in the QD and the continuum states in the WL [4.21]. The joint density of states between the localized and the delocalized states give rise to the continuous background in the excitation spectrum of the QD.

In Fig. 4.5, we plot qualitatively the joint density of states of a QD for understanding the observed energy-dependent spectra. The diagrams present three discrete states with the upper most state lying within the continuum tail. The positions of the excitation energy and the emission energy (lowest discrete state) in the three different situations described above are also

indicated. Figures 4.5(a), (b) and (c), explain the excitation and relaxation schemes for regions I, II and III in Fig. 4.4.

When E_{ex} is lower than the WL peak but higher than the discrete states of the QD, as shown in Fig. 4.5(a), the excited carriers can relax to the ground state by rolling down the continuum tail (through acoustic phonon emission) and then cascading through multi-LO phonon emission. Because the excitation energy which lies within the continuum tail generates a localized electron/hole in the QD and a quasi-free carrier with opposite charge in the wetting layer, the quasi-free carrier can be readily captured by the QD due to a Coulomb attraction. Hence the relaxation of excited carriers is efficient in this regime. Moreover, through quasi-continuous absorption, all of the QDs are excited, although the E_{ex} is lower than the WL band-edge. Therefore, under this excitation condition (region I or high-energy excitation), all of the QDs emit light and the emission spectra are basically the same as that from conventional PL measurement.

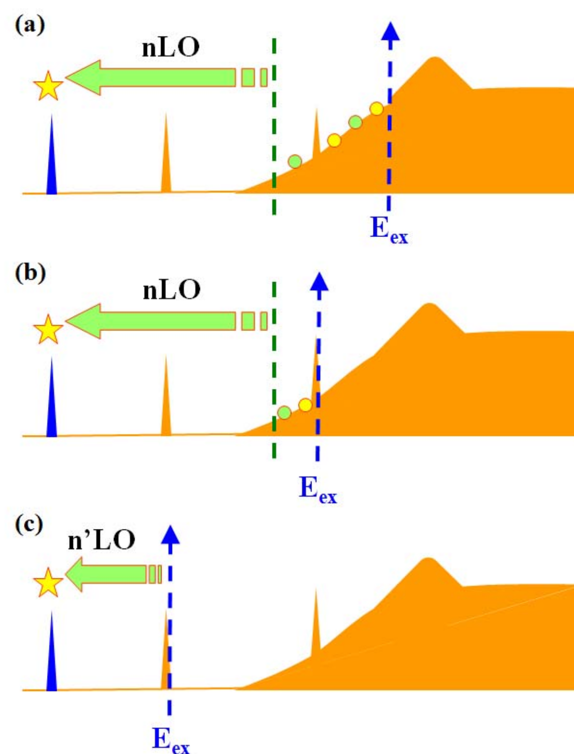

Fig. 4.5 Schematic excitation and relaxation processes for (a) region I, (b) region II, and (c) region III in Fig. 4.4.

The density of states associated with the continuum tail declines gradually as the energy decreases. Once the excitation energy of the pumping photons is sufficiently low to reach the discrete states of the QD, the sharp levels enhance absorption by resonant excitation. At moderate excitation energies (region II in Fig. 4.4), the carriers are resonantly excited to the upper discrete states, which lie within the continuum tail of the joint density of states. As shown in Fig. 4.5(b), in addition to the multi-LO phonon scattering, the relaxation of the excited carriers can be still achieved via the continuum states. The QDs whose upper states resonate with the excitation energy thus yield ground state emission. In this case, the energies of the discrete states of the QDs can be extracted from the spectra. Since the QDs are inhomogeneous not only in size but also in shape and alloy profile, the emission energy of the resonantly excited QDs may still have a distribution. Therefore, the observed emission peak is not as narrow as that from a single QD.

Notably, the continuum in the joint density of states arises from the continuous states above the WL band-edge either of the conduction band or of the valence band. Once an electron-hole pair has been excited into a state within the continuum, the energy of this pair can be relaxed through the continuous states by either the electron or the hole. This is basically the energy relaxation mechanism associated with regions I and II in Fig. 4.4. The difference between the two, however, is in the selective excitation process in region II, which is governed by the sharp peaks associated with the discrete energy levels that overlap the continuum in the joint density of states. The enhanced absorption due to these peaks selectively excites the QDs whose peaks resonate with the excitation energy. These resonantly excited electron-hole pairs can undergo electron-hole scattering [4.22] and then release energy through continuous states in either the conduction band or the valence band. Since the quantized energy levels in QDs are functions of their size, information can be gained on the size-dependent energy levels of the QDs from the spectra in region II.

At very low excitation energies, as shown in Fig. 4.5(c), when the carriers are resonantly

excited to states below the continuum tail, they can relax to the ground state only via a multi-phonon process. The sharp peaks in the bottom few emission spectra in Fig. 4.4 (region III) are therefore signatures of multi-LO phonon filtered relaxation. These phonon resonant peaks have been confirmed to arise from an excited-state absorption followed by multi-phonon relaxation but not from a resonant Raman process [4.14]. The emission peaks in region III are even narrower than those in region II because the selected QDs need to be consistent with not only resonant absorption but also a multi-phonon resonant relaxation. Three phonon lines, marked by vertical straight lines in Fig. 4.4, are ascribed, from left to right, to the 2LO WL phonon peak (56meV), the 3LO WL phonon peak (83meV) and the 3LO QD phonon peak (100meV). These assignments yield the energy of the WL phonon as ~27.8meV and that of the QD phonon as ~33.3meV. These values are very close to those obtained by Steer et al. [4.12], which were ~28.4meV as the WL phonon energy and ~34meV as the QD phonon energy. The value for the WL phonons is lower than the LO phonon energy of the bulk InAs, 29.9 meV, because of the strong phonon confinement in the thin WL; the higher phonon energy for the QDs follows from the strong strain effect associated with the QDs [4.13]. It deserves to be mentioned that, in such regime where energy relaxation in QDs is efficient only via a multi-LO-phonon resonance process, an extremely long relaxation time of ~7.7 ns indeed has been reported for the first-excited-state excitons with the relaxation energy off-resonant with multi-phonon energy, demonstrating the existence of a pronounced phonon bottleneck [4.17].

4.4 Discussion for Small Quantum Dots: Electronic State Relaxation with No Optic-phonon Filtering Effect

The distribution of the joint density of states and the relative positions of the discrete states to the continuum are functions of the QD size. As the QDs become smaller, their discrete states move to the high energy side faster than does the continuum, so they may lie deeper in the continuum tail [4.21]. In this case, the energy relaxation of carriers via the continuum is

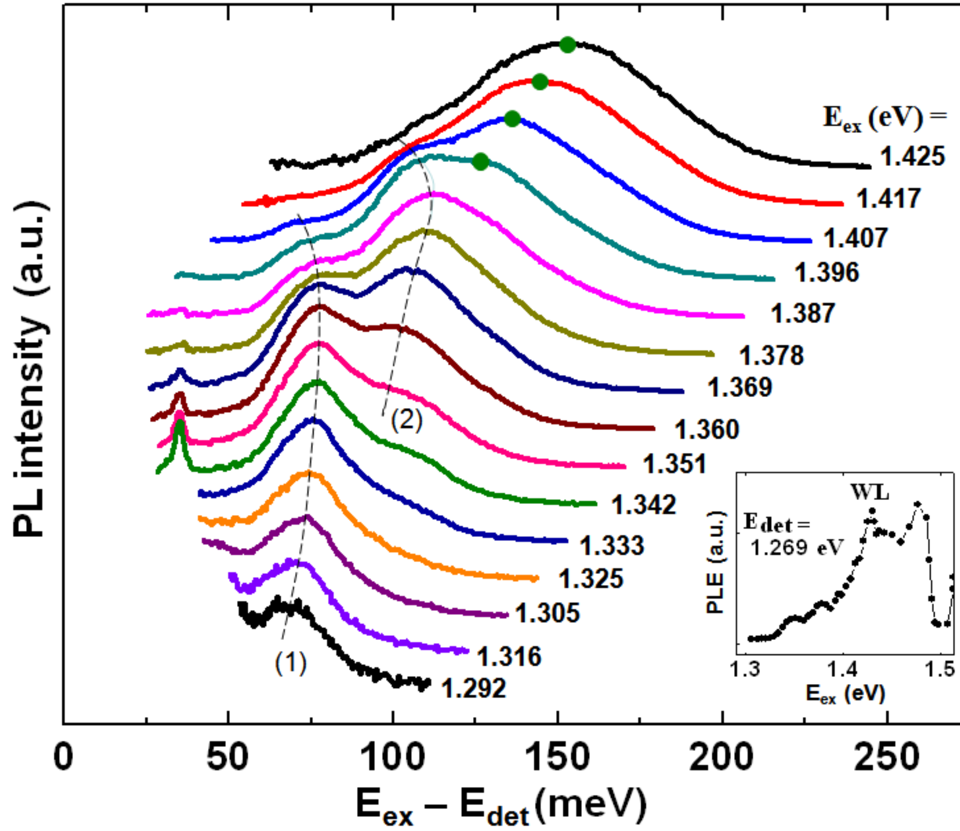

Fig. 4.6 SEPL spectra of small QDs (sample B) obtained at 13K. The x-axis refers to $E_{ex} - E_{det}$ and the intensity of each spectrum is normalized for clarity. The inset displays the PLE spectrum detected at 1.269 eV.

more pronounced. The SEPL study of sample B, which has extremely small QDs, was also conducted. Figure 4.6 displays the spectra of sample B that are plotted versus $E_{ex} - E_{det}$. The peak intensity is also normalized for clarity. All excitation energies were below the WL band edge, which was 1.43eV (as determined from the PLE spectrum in the inset). The shapes of the upper few spectra are similar to those of region I in Fig. 4.4. Hence, the carriers were excited to the continuum portion of the density of states. When the excitation energy is lower than 1.41eV, two resonant peaks are observed (see guided lines (1) and (2)). The fact that they do not line up at the same horizontal positions suggests that energy relaxation proceeds not only via the multi-LO phonon process, as in region III in Fig. 4.4. Rather, the process is of the type associated with region II in Fig. 4.4. This result confirms the continuum tail assisted relaxation under resonant excitation in such a sample with small QDs. In fact, afterward we also performed the SEPL spectroscopic studies for a quantum ring sample (LM4643), whose

discrete states (ground state energy is 1.329eV) lie even closer to the WL bandedge than the above small QDs. The obtained spectral result was similar to Fig. 4.6. It is then confirmed once more that continuum tail assisted relaxation indeed happens in samples with shallow discrete states. Figure 4.6 also includes another very sharp peak at E_{ex} - E_{det} = 35meV. The particularly small peak width (~ 2meV) suggests a resonant Raman process, in which the carriers are directly excited to the ground state of the QDs. The characteristic peak energy, 35meV, suggests that this Raman process is associated with the interface phonons in the QD structure [4.13, 4.23].

Since the relaxation process in sample B need not to meet the multi-LO phonon resonance condition, size-dependent excited state separations can be obtained by plotting the relaxation energy (E_{ex} - E_{gs}) versus the ground state energy (E_{gs}) for the two resonant peaks in Fig. 4.6. Figure 4.7 is such a plot, and it demonstrates that E_{ex} - E_{gs} initially increases with E_{gs}

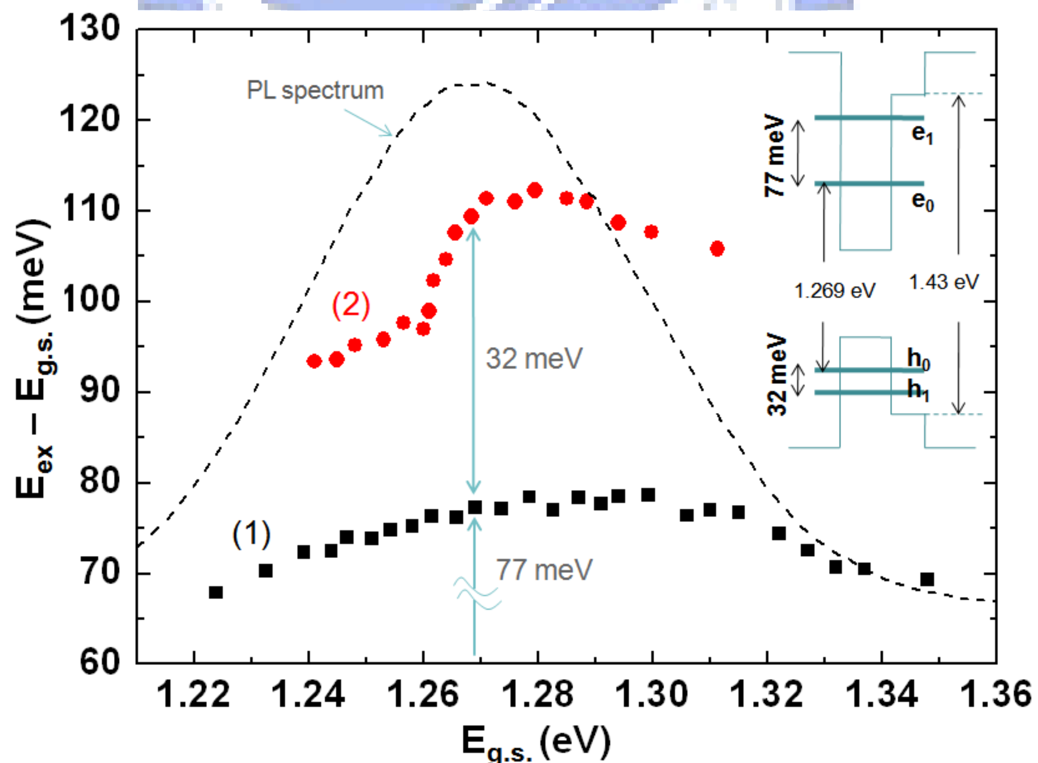

Fig. 4.7 Relaxation energy as a function of ground state energy plotted for the two resonant peaks in Fig. 4.6. The dash-line curve is the PL spectrum of the sample showing the size distribution of the QDs. The band diagram in the inset is constructed for the most populated QDs.

but then declines. For the QDs with an E_{gs} of lower than about 1.28 eV, the increased excited state separations exhibit a typical quantum size effect. However, for the small dots whose ground state energies exceed 1.28 eV, the quantum shape effect masks the quantum size effect [4.10]. In other words, these small QDs have a much lower height-to-width aspect ratio. This finding is expected because in the early stage of Stranski-Krastanov island growth, the deposited atoms do not support three dimensional growth until the nucleation sites are completely formed. Figure 4.7 also plots the size distribution of QDs in sample B, which is represented by the PL spectrum (dash line). For the most populated QDs, in which the ground state energy is 1.269 eV, the first excited state is separated by an energy separation of 77 meV from it, and the second excited state is separated by another 32 meV. Given the relaxed transition selection rule for the self-assembled QDs due to the broken symmetry, we believe that the large energy separation of 77 meV is associated with that between the e_0 state and the e_1 state. The small energy separation of 32 meV, on the other hand, follows from that between the h_0 state and the h_1 state. The possible band diagram for the most populated QDs is then constructed as shown in the inset. Assuming that 70% bandgap locates at the conduction band, this band diagram indicates that 48 meV is required to delocalize the bound holes in the h_0 state. Accordingly, when the h_0 hole and the e_1 electron are generated by the first excited state excitation, the e_1 electron first releases energy to enter the e_0 state by transferring 77 meV to the h_0 hole and making the hole free. The free hole can then release energy easily through the continuous states in the valence band. Therefore, the relaxation of carriers from this resonant excitation is not restricted by particular LO phonon energies. Similarly, the relaxation of carriers from the second excited state excitation proceeds even easier because the energy transfer from the e_1 electron is evidently sufficient to delocalize the h_1 hole. This band diagram thus verifies the feasibility of the continuum tail assisted relaxation scheme described in Fig. 4.5(b).

4.5 Summary

The energy spectra of InAs/GaAs self-assembled QDs were investigated using the selective excitation photoluminescence technique. The dependence of the emission spectra on the excitation energy provides important information about the carrier relaxation mechanism. Three distinct regions can be identified as associated with changes in the excitation energy. At high excitation energies, all quantum dots are excited and participate in the light emission with the help of the continuum states. At low excitation energies, the absence of the continuum states is such that the carrier relaxation is restricted to a multi-LO phonon process. Only the QDs with excited states at particular multi-LO phonon energies above the ground state can absorb and emit light. At medium energy, the QDs are resonantly excited through discrete electronic states, but the relaxation of the carriers does not need to meet the multi-phonon resonance condition with the help of a continuum tail. For these resonantly excited electron-hole pairs, intra-dot electron-hole scattering provides an efficient channel for the release of energy via the continuous states of either electrons or holes.

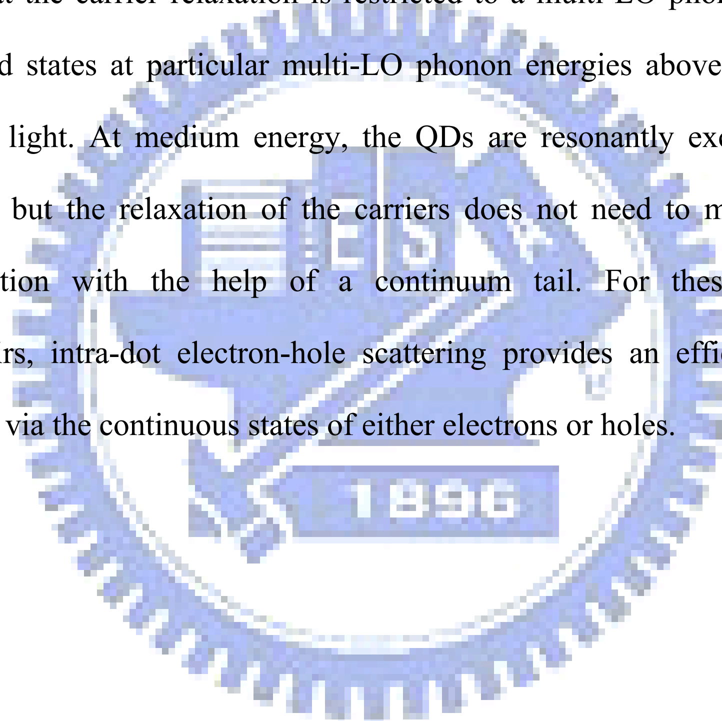

Chapter 5

Manipulation of Detection Wavelength and Device Performance in InAs Quantum Dot Detectors by Tailoring the Confinement Schemes

In this chapter, InAs QDs with different confinement barrier schemes are used in quantum dot infrared photodetectors (QDIPs) for the detection wavelength and device performance tuning. Compared with the simple InAs/GaAs QD structure, the QDs sandwiched by InGaAs well layers pushes the detection band to a longer wavelength to meet the 8-12 μm atmospheric transmission window. In addition, it enhances the TE-to-TM response ratio by a factor of 2.4, which is attributed to the reduced confinement of QDs in the vertical direction. The structure with QDs covered by a thin AlGaAs layer also serves to enhance the TE/TM ratio due to the enhanced lateral confinement of dots. Integrating these two functional structures, we design a modified InAs/$In_{0.15}Ga_{0.85}As$ dots-in-a-well (DWELL) structure for QDIPs with high degree of normal-incidence sensitivity and the detection peak of 8 μm. A thin $Al_{0.3}Ga_{0.7}As$ layer is inserted on top of the InAs QDs to enhance the confinement of QD states in the DWELL structure especially in the lateral directions. Besides additionally raising the TE/TM ratio by a factor of 1.8, the better confinement of the electronic states increases the oscillator strength of the infrared absorption and also the escape probability of the photoelectrons. Compared with the conventional DWELL QDIPs, the quantum efficiency increases more than 20 times and the detectivity is an order of magnitude higher at 77K under normal incidence configuration. Moreover, multi-color detection is achieved by replacing the InGaAs layers underneath QDs with GaAs for this confinement-enhanced structure. Tailoring the confinement barrier schemes of the QDs can extensively change the device characteristics of QDIPs and therefore provides the flexibility in QDIP design to fit different application requirements.

5.1 Introduction to the Confinement Dependency of the Polarization Intraband Transitions in Self-assembled Quantum Dots

As mentioned in chapter 1, infrared photodetectors based on intraband transitions in the III-V quantum structures are of great potential to be economical alternatives to the present leading HgCdTe based interband detectors. Particularly, with three-dimensional (3-D) quantum confinement, quantum dots (QDs) can restrain interaction of the bound-state electron with phonons and also relax the transition selection rule in quantum wells (QWs) [5.1] so that the radiation from all directions can induce the transitions. For that reason, it is anticipated that quantum dot infrared photodetectors (QDIPs) are more promising than commercial quantum well infrared photodetectors (QWIPs) to get breakthrough in cost down of the large-format imaging focal plane arrays (FPAs).

The normal incidence absorption capability of QDIPs is of great benefit because it avoids the necessity of fabricating grating couplers in the standard QWIP imaging arrays [5.1]. The grating coupler, regardless of its more fabrication cost, usually has high coupling efficiency only for a narrow bandwidth and becomes insufficient when broadband or multi-color detection is needed. Indeed, with the mature self-assembled QD growth, the normal incidence response in QDIPs with different spectral ranges has been reported since the pioneering work in 1998 [5.2-5.5]. However, from the polarization-dependent photoresponse measurements using the 45° edge-coupling scheme, QDIPs were found still more sensitive to the radiation with the electric field perpendicular to the epilayers (TM response) [5.6-5.10], similar to QWIPs. The response of normal-incident radiation (TE response, where the radiation electric field is parallel to the epilayers) was found dominant only for photons with very long wavelengths (≧ 15 μm) [5.11]. These findings are believed to result from the small height-to-width aspect ratio of the self-assembled QDs.

From the single-band calculation for QDs modeled as square-flat plates, strong confinement in the vertical direction creates large enough quantization with energy separation

accounting for the typical response band observed for QDIPs, while weak lateral confinement of the dot contributes to the deep-lying states with much smaller energy quantization. For such a square plate QD, the photo-induced transition of electrons between the bound states arising from a specific directional confinement is only allowed when the radiation has electric field component parallel to the confinement direction. This is the so called transition selection rule. In real case, QDs have a lens-shaped geometry instead of a plate-like geometry. Thus, each discrete state cannot be exclusively attributed to a certain directional confinement. The TE response and TM response may both have non-zero oscillator strength for a specific transition. Nevertheless, because the height-to-base-width aspect ratio of the dots is far smaller than unity (typically in the range of 1/10 - 1/3), the TE response dominates for up-transitions of the ground-state electrons to the deep-lying excited states while the TM response dominates for the photo-excitation to the high-lying excited states. The electrons that are excited to the higher-lying states have higher escape probability to contribute to the photocurrent, so the associated transition signals usually govern the photocurrent spectra of QDIPs. Such transition energies can be tuned to cover the important mid-wavelength infrared (MWIR, 3-5 μm) band and long-wavelength infrared (LWIR, 8-12 μm) band with different QD structures. Although the response of QDIPs in this wavelength range has lower sensitivity for TE-polarized photons than for TM-polarized photons, in principle, one can still enhance the TE mode response by means of tailoring the confinement scheme of the QDs in QDIPs. That is, to improve the lateral confinement of the dot while somewhat to reduce the vertical confinement of the dot.

The idea to enhance the TE response by improving the lateral confinement of the dot would be more appreciable if we examine the polarization absorption behavior of the wire-like quantum structures with clear asymmetry in the x-y directions [5.12]. It has been reported that, for the elongated InAs/$In_{0.52}Al_{0.48}As$ QDs, the normal-incident polarization-dependent absorption [5.12] or photocurrent [5.13] measurement unambiguously shows the dominant sensitivity to the polarized photons with the electric field parallel to the short axis of the dot ([1

1 0] direction), in which direction the quantum confinement is much stronger than in the long axis. On the other hand, for the In(Ga)As/GaAs QDs with more symmetric shapes on the x-y plane, such different “in-plane” polarized absorptions virtually disappear [5.10]. Hence, it is expected that the absorption coefficient of the normal-incident radiation, whose electric field is parallel to the epilayers, can be elevated by improving the lateral confinement of the QDs.

In the next section, for examining the effect of barrier confinement on the polarization intraband transition of InAs QDs, five QDIP samples with different QD confinement schemes were used to investigate the polarization-dependent photocurrent spectra under the 45 degree edge-coupling configuration.

5.2 Tuning of the Detection Wavelength and Polarization Response in InAs Quantum Dot Infrared Photodetectors

The active regions of the five QDIPs used in this study all contain ten layers of active structures separated by 50-60 nm GaAs barrier layers and have the same total thickness of 660 nm, which in turn are sandwiched between two 500 nm n^+GaAs contact layers. A δ-doped Si layer with a concentration of 1×10^{10} cm^{-2} was inserted 2nm underneath each InAs QD layer to provide electrons to the dots. This doping method, where only the shutters of Si cell and As cell were opened during the doping duration, was used so that the Si dopants could effectively occupy the cation sites to be the donors but not the acceptors. The QD growth in these five samples can be distinguished into two different situations. One is InAs QDs grown on GaAs, and the other is InAs dots grown on a 2nm $In_{0.15}Ga_{0.85}As$ pseudomorphic layer. In order to exclude the complex influence of the dot sizes and shapes, different InAs deposition amounts were purposely used in these two growth situations to form QDs with similar sizes. On GaAs surface 2.8 MLs of InAs were deposited, while on $In_{0.15}Ga_{0.85}As$ only 2.2 MLs of InAs were used because of the pre-accumulated strain energy in the $In_{0.15}Ga_{0.85}As$ layer. In both cases the growth rate and the growth temperature of the QDs were at 0.1 μm/hr and 510°C respectively.

The QD morphologies were checked by AFM scan for the uncapped QDs on the sample surfaces. The images are compared in Figure 5.1. The QD conditions obtained from the two different growth situations turned out to be very similar. Both exhibited similar dot sizes and good size uniformity. Similar sheet densities were determined in both conditions to be ~2.1×10^{10} cm^{-2}. Given the doping density used, we estimated an average number of original carriers in each QD around 0.5. With such a small carrier number, the possibility that the infrared response originates from the absorption of the excited state electrons should be very small so is ruled out in our analysis. In the following, basic device characteristics pertaining to the five samples with different QD confinement schemes are described first. After that, the polarization dependence of the responsivity of the five structures will then be discussed.

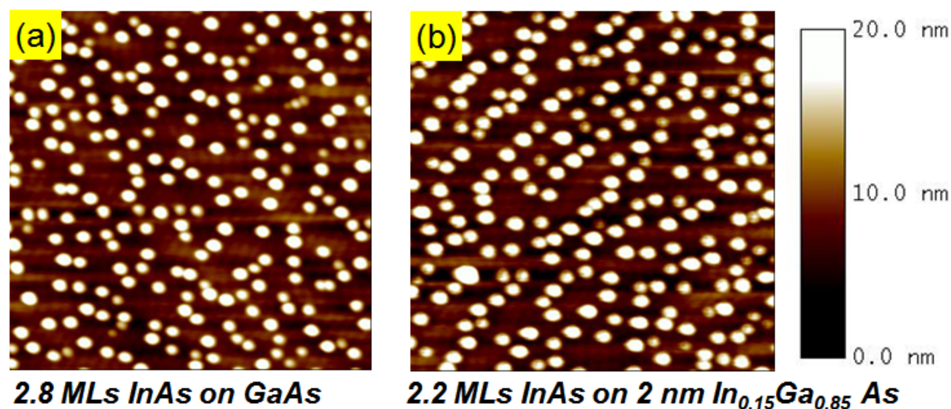

Fig. 5.1 1x1 μm^2 AFM images of the QDs grown on (a) the GaAs surface and (b) the InGaAs strained layer.

Fig. 5.2 shows the photocurrent spectra of the five samples and also schematically plots the respective single-layer active structures on the right hand side. The exhibited spectra were obtained with no polarizer. The sample with simple InAs/GaAs QD layers (RN0172) shows a response peak at 6.5 μm. By use of the state-filling PL spectroscopy, this response peak is believed to be from the intraband transition between the QD ground state and the wetting layer (WL) state. With such a simple QD structure, the device usually suffers from a very high dark

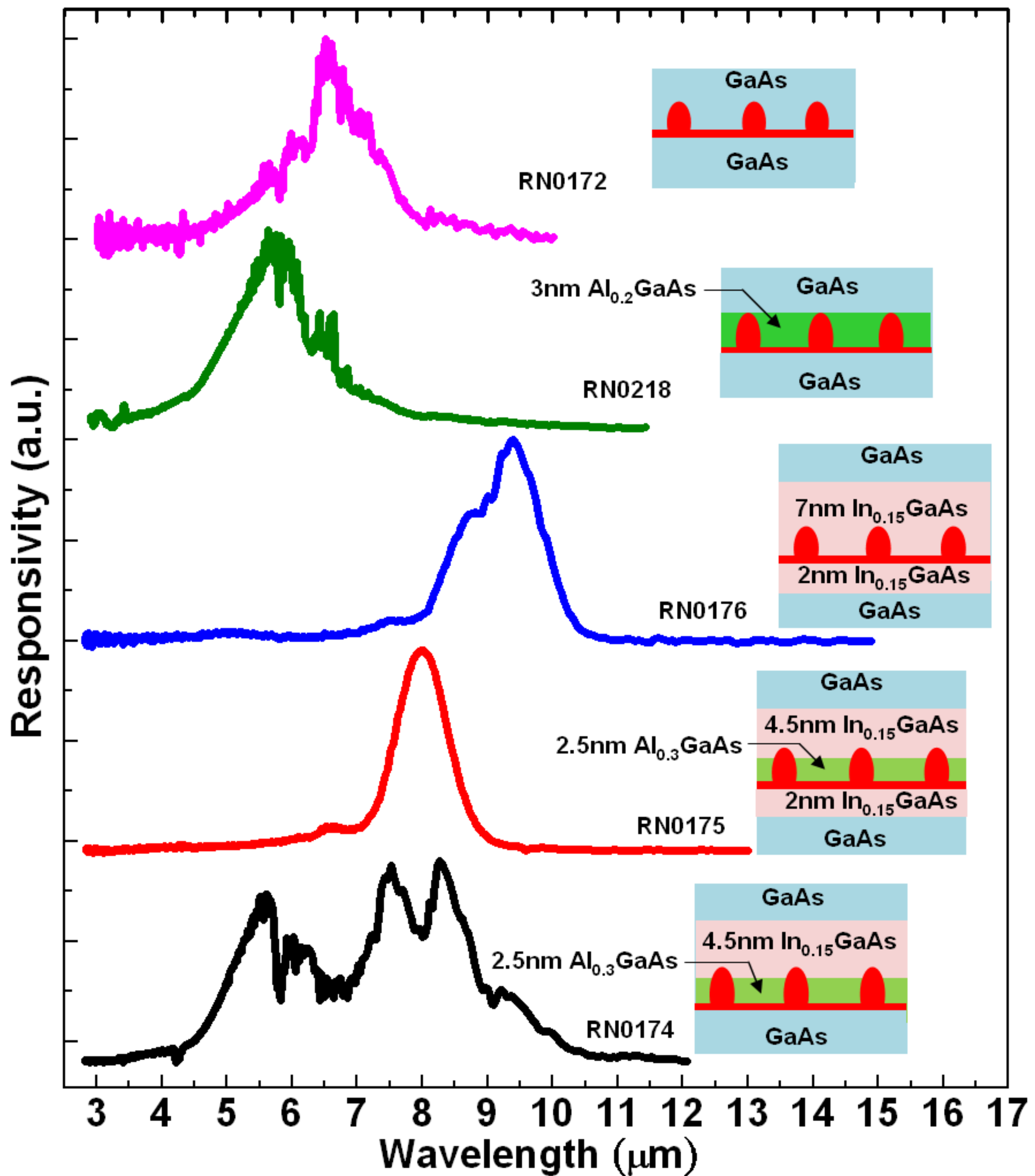

Fig. 5.2 Responsivity spectra of the five QDIP samples with negative bias at around 40K. Each active-layer structure is illustrated on the right hand side respectively. The QD layers are all grown with InAs materials.

current level, indicating the excellent electron transport property in GaAs materials. In order to reduce the dark current to an acceptable level, a 3nm AlGaAs layer is introduced on each QD layer to restrain the current flow across the WL region where no QD stands on it (RN0218). With this design, the device performance is greatly enhanced [5.14]. Also, the detection band slightly blue-shifts to around 6 μm because the AlGaAs layers push the WL state to a higher energy. Although the detector RN0218 has evidently enhanced device performance, the

detection band unfortunately is outside the atmospheric transmission window. As described in chapter 1, it is desirable to push the detection band to the long wavelength side into the LWIR transmission window (8-12 μm). Such a detection band not only allows longer distance detection but also corresponds to the maximum of the thermal radiation of room temperature objects. In order to fit the detection band into the LWIR window, the QDIPs designed with InAs/InGaAs dots-in-a-well (DWELL) structures have attracted more and more attentions recently [5.5, 5.15-5.23]. The detector RN0176 is such an example. The InAs QDs are imbedded in a 9 nm $In_{0.15}Ga_{0.85}As$ well, which in turn is positioned in the GaAs matrix. The photocurrent spectrum covers the wavelength range of 8.3-10.2 μm, which is good for the LWIR detection. Inspecting the spectrum carefully, the response band actually comes from two closely-separated transition peaks with the larger one at ~9.3 μm and the smaller one at ~8.8 μm. Both response peaks have relatively narrow bandwidths of about 10% ($\Delta\lambda/\lambda p$). Such narrow bandwidths along with the reduced transition energies suggest that the transitions are from the bound-to-bound (B-B) transitions of the QDs in the DWELL structure (which could be assigned more definitely by the state-filling PL spectroscopy shown in Fig. 5.7). With the help of the InGaAs well layers, the photo-electrons from the QDs' B-B transitions can be extracted outside so that longer wavelength detection is achieved. With the desired LWIR detection band, however, QDIPs with conventional DWELL structures suffer from their inherently poor quantum efficiency. The confinement barrier for QDs is lowered with the surrounded $In_{0.15}Ga_{0.85}As$ materials so that the oscillator strength of the infrared response suffers. To solve this problem, we design a modified DWELL structure as schematically plotted in Fig. 5.2 for the sample RN0175, which use a 2.5nm $Al_{0.3}Ga_{0.7}As$ layer on InAs QDs in the DWELL structure to provide enhanced wavefunction confinement, especially for the lateral confinement that is inherently weaker for self-assembled QDs. Again, relative to RN0176, transition wavelength in RN0175 blue-shifts to 8 μm due to the enhanced confinement effect for QDs by the insertion of AlGaAs layers. For also examining the influence of the InGaAs

layer below QDs on the device characteristics for the confinement-enhanced DWELL (CE-DWELL) QDIPs, another CE-DWELL structure was also studied by the sample RN0174. Compared with RN0175, the only difference of RN0174 lies in the replacement of the 2nm $In_{0.15}Ga_{0.85}As$ layer underneath QDs by GaAs materials. With this adjustment, the shape of the photocurrent spectrum changes dramatically, which is seen clearly in the bottom side of Fig. 5.2. The spectrum of RN0174 shows a multi-color detection. In addition to the sharp peaks with wavelength longer than 7 μm (λ_p at 8.3μm) that are associated with the B-B transitions in QDs, a broader transition signal spanning the 4.5-7 μm band also emerges unambiguously in the spectrum (the dip at 5.8 μm could be observed for all the different QDIP structures, so we regard the neighboring response signal as one broad peak rather than two narrow peaks). This broad signal is most likely from the transition from the QD ground state to the 2-D state in the CE-DWELL structure (such a higher-lying state is recognized in Fig. 5.7), and the reason for its emergence could be ascribed to the enhanced confinement for the 2-D state wavefunction due to the substitution of the GaAs materials for the InGaAs materials underneath QDs. Such an enhanced wavefunction confinement makes the oscillator strength between the 2-D state and the QD ground state high enough to contribute to the photoresponse.

Due to the strain distribution, the deposited thin $Al_{0.3}Ga_{0.7}As$ layer was expected to aggregate in areas without QDs first. Such a property is favored since with a proper AlGaAs thickness the structure can provide barriers that enhance the confinement in the lateral direction but do not deteriorate the carrier transport through QDs in the vertical direction much. In order to confirm this, the active layer structure of RN0175 was examined by the cross-sectional TEM image shown in Fig. 5.3. It is clearly seen that the AlGaAs layer is flat instead of conforming to the shape of the InAs dots. Besides, the coverage of 2.5 nm AlGaAs is thin enough to leave the QD tip exposed. The height of the QD is about 5 nm and the base width is about 26 nm. For the QD structure as shown in Fig. 5.3, the confinement barrier for InAs QDs is elevated by AlGaAs

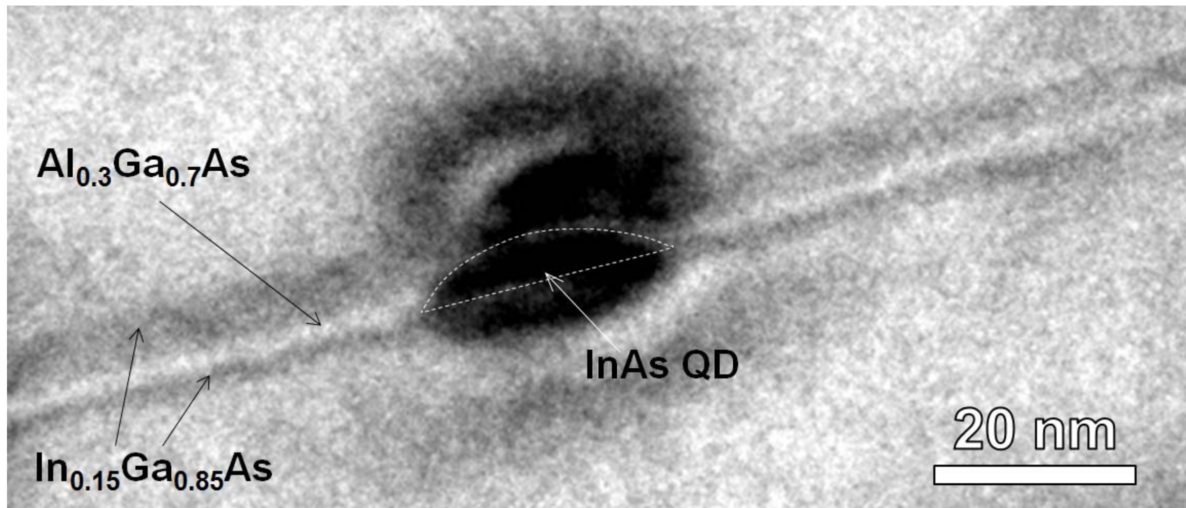

Fig. 5.3 Cross-sectional TEM image of the confinement-enhanced DWELL structure with a thin AlGaAs layer.

materials in the lateral directions while lowered by InGaAs materials in the vertical direction. In this case, the unbalanced confinement effect for QDs due to inherently small height-to-width aspect ratio now is partly compensated. As a result, it is also expected that with such a confinement scheme, the TE response could be enhanced relative to the TM response.

The polarization dependence of the integrated responsivity of the aforementioned five QDIP samples, as well as a B-B type GaAs/AlGaAs QWIP sample, is compared in Fig. 5.4. The measurements were performed under the 45° facet-coupled configuration as schematically illustrated in the inset. It should be mentioned that, here the metal contact on device mesa was purposely evaporated with no optical window to avoid incorporating stray light from the mesa top. A polarizer was put into the optical path to polarize the incident infrared light. When the polarizer angle was changed, the responsivity spectrum of each sample varied accordingly. It was found that the variation lies mainly in the intensity but scarcely in the spectral shape. The photons with 0° polarization induce photocurrent in the sample with 50% from the TM response and 50% from the TE response, while the 90° polarized photons generate photocurrent from pure TE response. As shown in Fig. 5.4, all the samples reveal a monotonic decay for the integrated responsivity when polarizer angle changes from 0° to 90°, showing dominance of the TM response over the TE response due to the dominant confinement effect in the z direction.

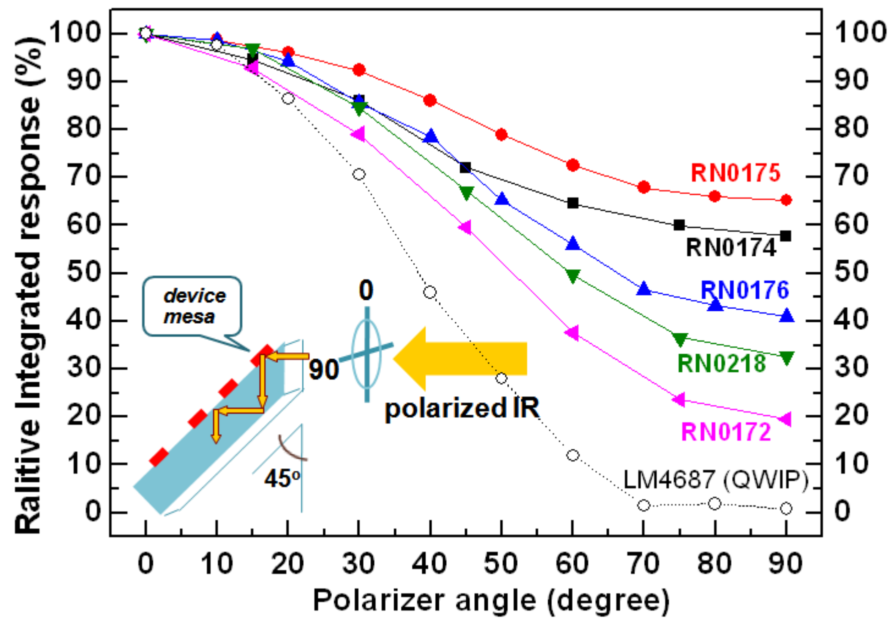

Fig. 5.4 Polarization dependence of the integrated responsivity of the five QDIPs measured under the 45° edge-coupling configuration illustrated in the inset. Also added on to the figure is the data (empty circles) of a GaAs-AlGaAs QWIP with B-B type transition, demonstrating the polarization selection rule predicted for QWIPs.

The decay in the QWIP sample is especially fast, with the intensity becoming negligible for the polarization angle larger than 70°. Almost zero TE response is obtained in this case, confirming the polarization selection rule predicted for the n-type QWIPs with B-B transitions [5.1]. While for the five QDIP samples, remarkable TE response is obtained due to significant quantum confinement in the x-y directions. Among them, the detector with the CE-DWELL structure (RN0175) as shown in Fig. 5.3 reveals the highest capability of TE response as expected, for it has both enhanced lateral confinement and reduced vertical confinement. The TE-to-TM integrated response ratio of RN0175 is deduced to be ~48%, over four times higher than that of the QDIP with a simple QD structure (RN0172, ~11%). Such a great improvement in normal incidence absorption makes the CE-DWELL QDIPs promising for the FPA applications. Looking into the distribution of the relative TE response (at 90°) of the five QDIPs, the correlation between the TE mode sensitivity and the confinement scheme of QDs can be understood as the following. First, RN0218 has the TE/TM ratio higher than RN0172, for the introduced thin AlGaAs layer on QDs enhances the QD confinement mainly in the lateral

directions. Then, the other three samples (RN0174-176) with InGaAs layers adjacent to the QDs show even higher TE/TM ratios, which are attributed to the reduction of the vertical confinement of QDs. This confinement reduction may be due ether to the reduced barrier height by InGaAs materials or to the strain reducing by capping QDs with InGaAs that makes the dots steeper in shapes. Comparing RN0175 with RN0176, the thin AlGaAs layer on QDs improve the lateral confinement for the dots in the DWELL structure and thus further contributes to the increase of the TE/TM ratio by another factor of 1.8. Finally, RN0174, which has the CE-DWELL structure however with the InGaAs layer underneath QDs replaced by GaAs, demonstrates a slightly lower TE/TM ratio than RN0175 due to the increase in the vertical confinement of QDs. The 2 nm thin InGaAs layer underneath QDs turns out to be beneficial for improving the TE mode sensitivity by lowering the confinement barrier for QDs in the vertical direction.

It should be mentioned for getting optimal signal quality in each device, the different polarization-dependent behaviors shown in Fig. 5.4 were measured for the five QDIPs at different temperatures (within 20K-77K) with different bias conditions. To check if such a comparison has general validity, 0° polarized and 90° polarized photocurrent spectra were compared for RN0175 under different operation temperatures and bias polarities. The results are shown in Fig. 5.5. Two conclusions about the polarization can be obtained: (1) The spectral shape has little dependence on the polarization angle for all operation conditions. (2) The peak

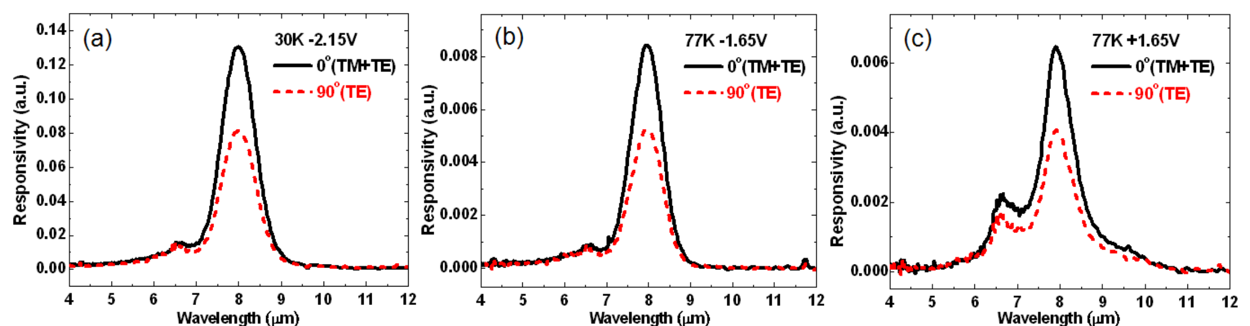

Fig. 5.5 0° polarized and 90° polarized photocurrent spectra of the CE-DWELL QDIP at different temperatures ((a), (b)) and different bias polarities ((b), (c)).

intensity ratio of 0° response to 90° response in each operation condition is nearly the same, about 1: 0.63. It is thus confirmed that the operation condition is not decisive to the polarization-dependent behavior of the device. However, it may be suspected that the polarization dependence of the responsivity depends critically on different transition states (final state) rather than the confinement schemes of the QDs. This concern could be verified by comparing the 0° polarized and 90° polarized photocurrent spectra of RN0174, for its response signals include the photo-excitation to both the QD bound excited-states (B-B) and the 2-D associated states (B-2D), as shown in Fig. 5.6. Judging from the figure, the intensity ratios between 0° polarization and 90° polarization for both the B-B type and the B-2D type transitions are very similar. No discriminating polarization dependency is observed for the two transitions with very different final states. So, the QD confinement scheme should be the governing factor of the polarization absorption property of QDIPs. The previous discussion for the five QDIP samples with different confinement schemes is confirmed.

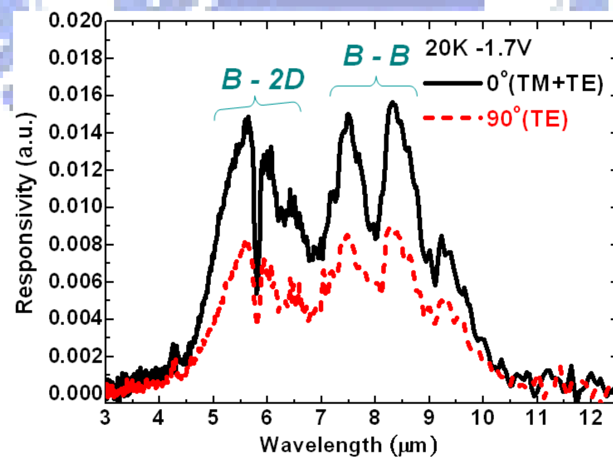

Fig. 5.6 0° polarized and 90° polarized photocurrent spectra of the CE-DWELL QDIP with multi-color detection.

5.3 Comparison between the LWIR Quantum Dots-in-a-Well detectors with and without Thin AlGaAs Layers

As described in the last section, we can tailor the detection wavelength as well as the

polarization response for InAs QDIPs by using different confinement barrier schemes for QDs. Among the five examined QDIPs, the structures with InGaAs layers adjacent to the QDs (RN0174-RN0176) show the capability of LWIR detection and, because of more balanced confinement effects, reveal higher TE/TM ratios. So, they are more favorable than the others to the FPA applications. In this section, we further look into and compare their device performance under normal incidence configuration, with a view to picking out the most promising active structure for further development.

At first, state-filling PL spectroscopy was performed at 77K for the three samples, RN0174-RN0176, to understand the distribution of energy states in each QD structure and also identify the transition states for the infrared response. The measured spectra are compared in Fig. 5.7 with the vertical scale shifted apart for clarity. Each spectrum reveals several QD states (filled up to the fourth or the fifth energy shells) as well as a 2-D bound state in the active structure. In addition, the emission from the n^+ GaAs contact layers is also clearly seen (with

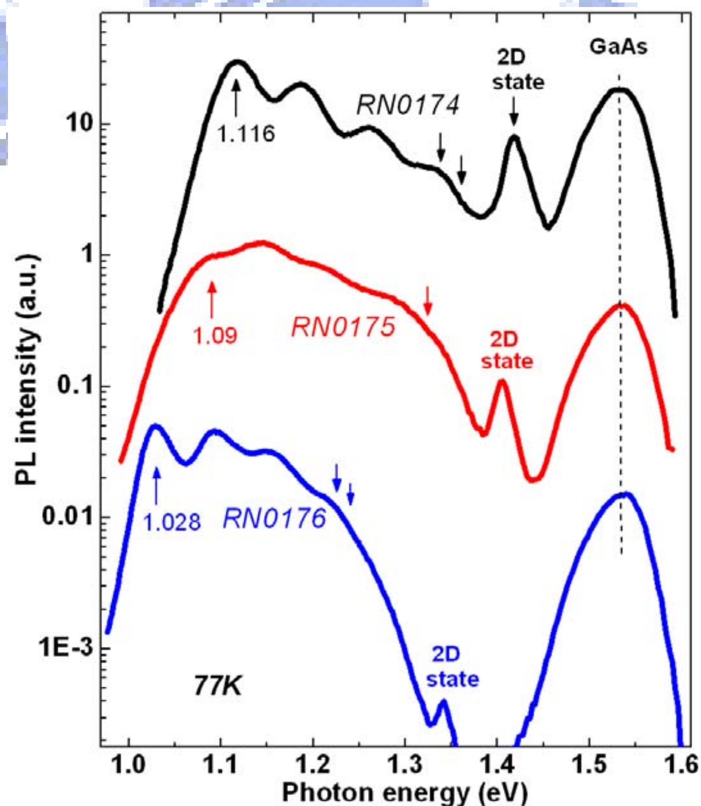

Fig. 5.7 PL spectra of the three QDIP samples under high power excitations at 77K.

identical peak energies as aligned by the dashed line). The confinement of the QD states of the samples gradually increases from RN0176 to RN0174 due to higher barrier surrounding the QDs. This is confirmed by the spectra in Fig. 5.7. Compared with RN0176, the ground state energy blueshifts by 62 meV in RN0175, while it blue-shifts by 88 meV in RN0174. We attribute the observed blueshift to arise from the enhanced confinement effect of the QDs rather than the composition change of the dots that might result from different capped materials, because it has been reported that capping the InAs QDs with an Al contained layer should instead cause a redshift for the ground state energy due to the suppression of the In segregation [5.24]. Given that the ratio of the confinement energy in conduction band to that in valence band is typically about 2 : 1, we can identify the infrared response peaks observed for RN0174-RN0176 in Fig. 5.2 to be from the transition(s) between the ground state to the high-lying state(s) that is/are marked by the downward arrow(s) in each spectrum in Fig. 5.7. For ether RN0176 or RN0175, the infrared response only involves the B-B transitions of the QDs. While for RN0174, beside the QDs' B-B transitions, the transition from the QD ground state to the 2-D state in the active structure (B-2D) also contributes to the responsivity spectrum (see Fig. 5.6). Such a multi-response property makes the structure of RN0174 a potential candidate for the MWIR and LWIR dual band detection [5.25].

After perceiving the state energy distribution in the active structures, the detailed device performance at 77K were then compared and discussed. Fig. 5.8(a) shows the comparison of the dark current curves. The dark current in RN0174 is higher than that in RN0175, which in turn is higher than that in RN0176. Such a result is understandable because higher ground state energy for QDs corresponds to smaller carrier activation energy which could generate higher dark current. At 77K and -1V, the dark current in RN0174, RN0175, and RN0176 is 3.00×10^{-6} A, 3.68×10^{-7} A, and 3.17×10^{-8} A respectively. All three values are far lower than what measured for the sample with simple QD structures (4.22×10^{-4} A for RN0172), showing the advantage of smaller dark current level pertaining to the QDIPs based on DWELL designs. Moreover, the

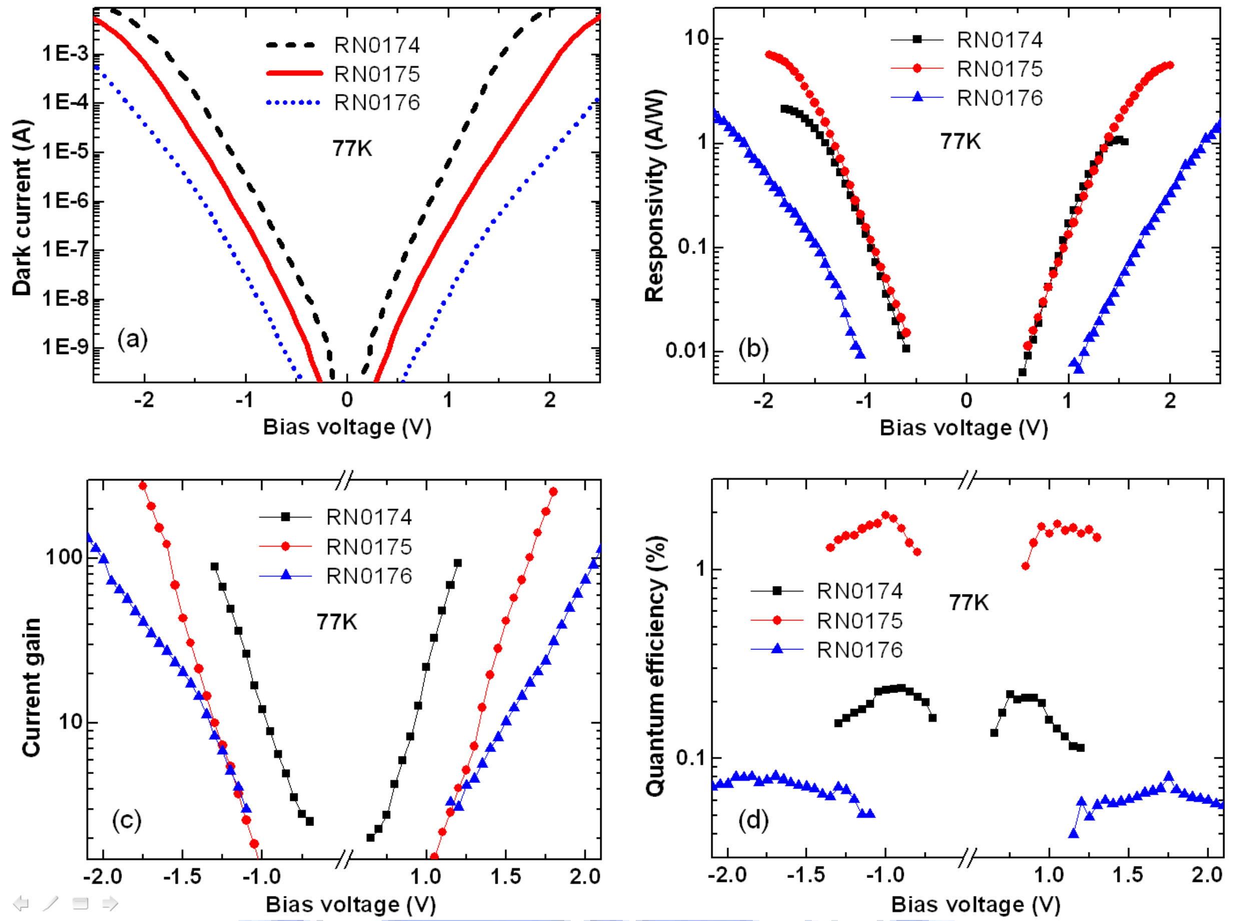

Fig. 5.8 Comparison of the voltage dependence of (a) the dark current, (b) the peak responsivity, (c) the current gain and (d) the quantum efficiency for the three samples at 77K.

inserted thin AlGaAs layers also contribute to the dark current suppression. Compared with RN0176, the dark current in RN0174 increases for about 100 times with the ground state elevation of ~60 meV. In principle, the dark current should increase for more than 8800 times if we consider pure thermal excitation (~ $\exp(\Delta E/kT)$). However, due to the high barrier of AlGaAs layers, the increase of the dark current is much less than expected. This reduces the drawback of the higher ground state energy.

The photocurrent measured for the three samples showed an inter-relationship similar to the dark current result. RN0174 revealed the highest photocurrent while RN0176 showed the lowest photocurrent. However, such a sequence relation changed when referring to the peak responsivity of the photocurrent spectrum due to the significant difference in the values of the

integral term in equation 2.1. RN0174 had a particularly broad photocurrent spectrum so its (peak) responsivity suffered even if its photocurrent was obviously larger than the other two. The comparison of the responsivity curves is shown in Fig. 5.8(b). The responsivity turned out to be very similar for the two CE-DWELL detectors in the bias range from -1.2V to 1.3V, which then surmounted that in the conventional DWELL detector by over one order of magnitude. At -1.1V and 77K, the responsivity for the two CE-DWELL samples are 0.242 A/W (RN0174) and 0.284 A/W (RN0175) while it is only 0.011 A/W for the conventional sample (RN0176).

To further probe the origin of the large elevation in responsivity for the two detectors with thin AlGaAs layers, the current gain and the quantum efficiency (QE) were separated from the responsivity and compared in Fig. 5.8(c) and Fig. 5.8(d) respectively. The data with very low bias voltage is absent due to the limit of noise measurement. It is clearly seen that the current gain for RN0174 is higher than the other samples while RN0176, which has the conventional DWELL structure, shows the lowest current gain. The result is ascribed to the following: in DWELL structures, the InGaAs QWs effectively capture the carriers and reduce the current gain. As parts of the InGaAs well layer is replaced by the AlGaAs and GaAs barrier layers in RN0174, the transit time through the QW is shorter and the current gain is enhanced. Although it might be expected that the inserted AlGaAs wide bandgap layer could deteriorate the carrier transport in RN0175, the barrier is thin enough so that such a gain reduction balances the reduced InGaAs thickness and similar current gain was achieved for RN0175 and RN0176 in the bias region between -1.3V and 1.25V. The difference in responsivity for RN0175 and RN0176 is thus primarily attributed to the difference of QE. Comparing with the QE of the DWELL sample (RN0176), the QE of the CE-DWELL sample (RN0175) is much higher over the measured bias range and increases faster with the applied voltage (Fig. 5.8(d)). The highest QE in CE-DWELL is around 2% at -1V, which is clearly superior to that in DWELL (0.08% at -1.7V).

The calculated excited state wavefunctions of the QDs in the conventional DWELL and the CE-DWELL structures are shown respectively in Fig. 5.9(a) and Fig. 5.9(b), represented by the contour plots. In the conventional DWELL (Fig. 5.9(a)), the electronic excited state wavefunction extends out a lot to the $In_{0.15}Ga_{0.85}As$ QW region. With the introduced InGaAs QW, the absorption strength associated with the B-B transition becomes weaker due to the decreased dipole element. On the other hand, in the CE-DWELL (Fig. 5.9(b)) the wavefunction spreading is apparently restrained due to the inserted thin AlGaAs layer. Such a wide bandgap layer confines the excited state wavefunction to be more localized and therefore enhances the absorption strength due to better wavefunction coupling. In addition, the excited state energy in the CE-DWELL sample (RN0175) is about 41 meV higher than that in the DWELL sample (see Fig. 5.7). The escape probability of the photo-excited carriers is thus higher and as a result the operation voltage needed for maximal QE is lower for the CE-DWELL sample. Such a bias point occurs even earlier for RN0174 (Fig. 5.8(d)), for its photo-excited carriers have even higher escape probability. For RN0174, which has also a confinement enhanced structure, the promotion in QE is however not as large as that for RN0175 (Fig. 5.8(d)). This result is readily understood because the absorption strength of the ground state electrons is shared by different transition paths in RN0174 so that each absorption peak becomes weaker. The highest QE in such a multi-color QDIP with λ_p at 8.3μm is around 0.24% at -0.9V, still higher than that of the

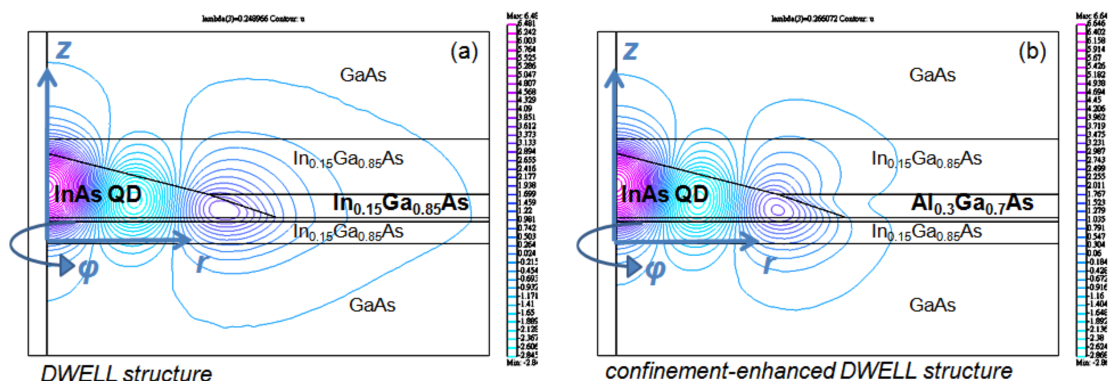

Fig. 5.9 Contour plots for the excited state wavefunctions calculated for (a) the conventional DWELL structure and (b) the CE-DWELL structure.

conventional DWELL sample by a factor of three, showing the advantage of employing the confinement enhancing layers.

The measured noise current as a function of bias voltage and the specific detectivity obtained in turn were then compared for the three samples in Fig. 5.10(a) and (b) respectively. As shown in Fig. 5.10(a), the two CE-DWELL samples (RN0174 and RN0175) reveal higher noise current than the DWELL sample (RN0176), with the sequence arranged the same as in the case of the dark current (Fig. 5.8(a)). This is expected since the device with higher dark current usually generates larger noise current. Comparing RN0175 with RN0176, although the CE-DWELL detectors have higher noise level, the large increase in the QE overcomes this drawback and makes their overall performance far superior to that of the conventional ones. As Fig. 5.10 (b) shows, at 77K, the highest detectivity measured for the CE-DWELL detector (RN0175) is $1x10^{10}$ cm $Hz^{0.5}$/W (at -0.9V), which is ten times higher than that in the DWELL detectors ($1x10^{9}$ cm $Hz^{0.5}$/W at -1.2V measured for RN0176). As for RN0174, which also has thin AlGaAs CE-layers on QDs however without InGaAs layers underneath QDs, the highest detectivity at 77K was measured to be $1.15x10^{9}$ cm $Hz^{0.5}$/W (at -0.75V), similar to that in the conventional DWELL detectors. Despite the inserted confinement enhancing layers, little improvement in the overall performance was achieved in this case. Comparing the device characteristics carefully for RN0174 and RN0176, the outperformance of responsivity in

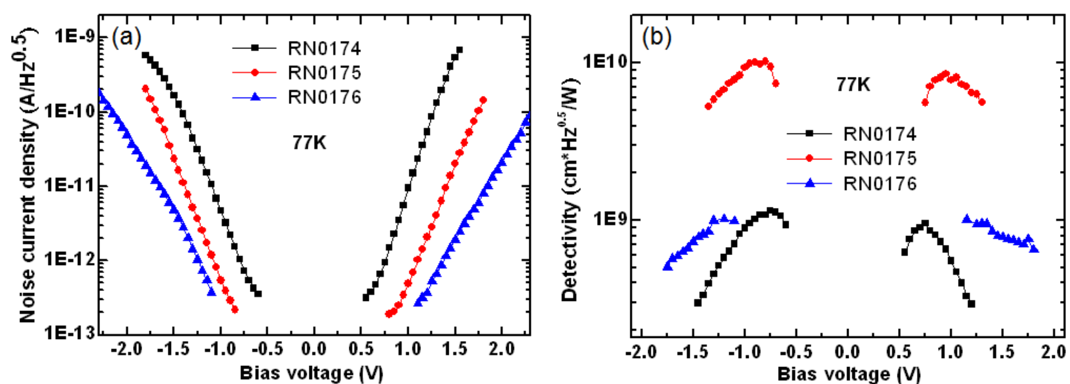

Fig. 5.10 Comparison of the voltage dependence of (a) the noise current density at 1 kHz and (b) the specific detectivity for the three samples at 77K.

RN0174 is found primarily from a much higher current gain but rarely from the QE (see Fig. 5.8(b), (c), and (d)). The GaAs barrier layer instead of the InGaAs well layer positioned underneath QDs greatly increases the current gain. However, such a current gain improvement contributes little to the signal-to-noise ratio because it indicates an improved carrier transport for both the photocarriers and the thermal carriers. The responsivity and the noise level are both raised in RN0174, thus leaving the detectivity scarcely improved.

From the above discussion, it is clear that to increase the QE is more essential than to increase the current gain for advancing the overall performance of QDIPs. The CE-DWELL structure of RN0175, in which the InAs QDs are grown on a 2nm $In_{0.15}Ga_{0.85}As$ layer and covered by 2.5nm $Al_{0.3}Ga_{0.7}As$/4.5nm $In_{0.15}Ga_{0.85}As$ structure, demonstrates the highest TE/TM response ratio, the highest quantum efficiency, and also the highest detectivity so is the most promising QD confinement scheme for high performance QDIPs. The inserted AlGaAs wide bandgap layer in the DWELL structure greatly enhances the confinement of the electronic states and thereby largely enhances the device performance.

Finally, it was also noticed that the asymmetric confinement barriers surrounding QDs generated the bias tunable detection in RN0174 as shown in Fig. 5.11. As the inset shows, the barrier materials covering the QD tips are InGaAs while that adjoining the QD bottoms are GaAs. With such an asymmetry in the vertical direction, the spectrum at positive bias reveals a very different shape from that at negative bias. As shown in Fig. 5.11, the difference lies in the long wavelength portion of the spectrum, which belongs to the B-B transitions of the QDs. At positive bias, the photoelectrons are extracted upward through the InGaAs well layer and then to the GaAs barrier. With the help of the InGaAs well layer, the escape probability of the photoelectrons greatly increases so that the B-B transition with a longer wavelength (of around 10 μm) can dominate the spectrum due to higher oscillator strength. While at negative bias, the photoelectrons must escape directly to the GaAs barrier layer underneath QDs with a reduced probability. Thus, the 10 μm signal is fully suppressed and the transition peaks with shorter

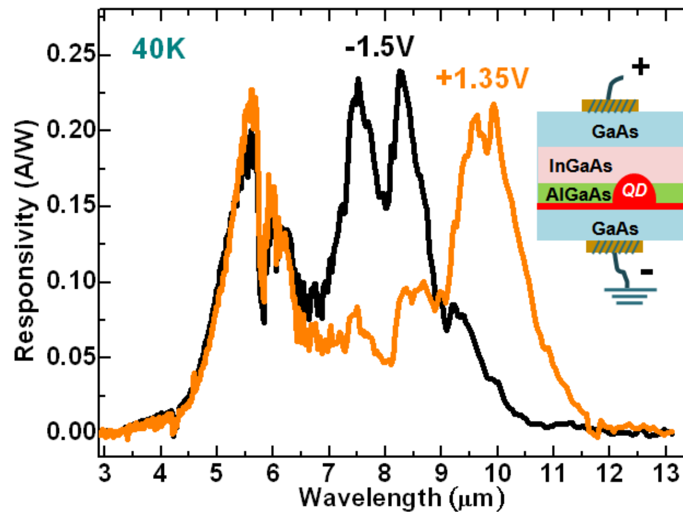

Fig. 5.11 Responsivity spectra at different bias polarities of the asymmetric CE-DWELL QDIPs.

wavelengths (at 7.6 μm and 8.3 μm), because of a relatively higher escape probability for carriers, dominate the spectrum. As for the other samples discussed in this chapter, the spectral shapes under different bias polarities were relatively similar, which was attributed to the relatively symmetric QD barriers. The asymmetric confinement scheme for QDs provides the bias tunable detection for QDIPs.

5.4 Summary

We investigated several QD confinement schemes for QDIPs by examining the polarization-dependent photocurrent spectroscopy. Both the peak wavelength and the TE-to-TM response ratio were manipulated by putting different barrier schemes on QDs. In this way, we demonstrated that the TE/TM ratio could be increased either by enhancing the lateral confinement or by weakening the vertical confinement for QDs. Compared with the simple InAs QD structure, the InAs/InGaAs DWELL structure enabled the detection wavelength tuning to the LWIR band for QDIPs. Also, the TE/TM response ratio was greatly increased, which was attributed to the vertical confinement reduction for the QDs that were sandwiched by InGaAs layers. On the other hand, the structure with the QDs covered by a thin AlGaAs layer also revealed an enhanced TE/TM ratio over the simple QD structure due to the enhanced

lateral confinement of QDs. Combining the above two schemes, we designed a modified DWELL structure for QDIPs. A thin AlGaAs layer was inserted on top of the QDs in the DWELL structure as a confinement enhancing layer. This novel design simultaneously improved the lateral confinement and weakened the vertical confinement for the inherently flat shape self-assembled dots, making the QDs' wavefunctions more localized and steeper. The sample with such a confinement enhanced DWELL (CE-DWELL) structure showed highest TE mode sensitivity. Besides, the advantage of the LWIR (8-12 μm) detection capability was also preserved. Most importantly, the enhanced confinement effect greatly increased both the absorption quantum efficiency and the escape probability of photocarriers, while the carrier transport was almost maintained. At 77K, the maximum quantum efficiency was increased by about 25 times and the peak detectivity was increased by about ten times with a lower bias voltage under normal incidence configuration. Our results demonstrate that the CE-DWELL structure is a very promising approach toward the realization of high performance QDIPs with LWIR detection. In addition, the thin InGaAs layer underneath QDs in the CE-DWELL structure was also confirmed to play a significant role on the device characteristics and is preferred for high performance single-color detectors. For the sample without such InGaAs layers which mediate between QD layers and the underneath GaAs barrier layers, multi-color detection was achieved, and the peak responsivity was also maintained due to the greatly promoted carrier transport. However, the dark current also increased significantly and therefore the overall performance was degraded.

Chapter 6

Confinement-enhanced Quantum Dots-in-a-well Infrared Photodetectors

In this chapter, $InAs/Al_xGa_{1-x}As/In_{0.15}Ga_{0.85}As$ confinement-enhanced dots-in-a-well (CE-DWELL) structures are studied in detail for QDIPs. The $Al_xGa_{1-x}As$ layer inserted above the InAs QDs effectively enhances the confinement of QD states in the $In_{0.15}Ga_{0.85}As$ DWELL structure and therefore upgrades the device performance. With the CE-DWELL design, we have demonstrated the LWIR QDIPs with operating temperature over 200K. Moreover, the thickness and Al content of the AlGaAs insertion layers influence much not only the absorption property but also the transport property of the CE-DWELL QDIPs. The device with thinner $Al_{0.3}Ga_{0.7}As$ layers possesses stronger normal-incident absorption and higher responsivity, while the device with thicker $Al_{0.3}Ga_{0.7}As$ layers possesses better suppression of the dark current and is more suitable for the high temperature operations. Furthermore, compared with the $Al_{0.2}Ga_{0.8}As$ CE-layer, the $Al_{0.3}Ga_{0.7}As$ CE-layer provides stronger barrier confinement and causes less In-Ga intermixing for the InAs QDs and thereby generates better performance of the device. With appropriate device parameters of CE-DWELL, it is possible to achieve high quantum efficiency, high operating temperature, and long-wavelength detection at the same time.

6.1 Introduction

As mentioned, LWIR detectors are essential to the thermal radiation detection of room temperature objects. With such long detection wavelengths, traditional high quality detectors require low operating temperature which is undesirable from commercial point of view. QDIPs utilizing intersubband transitions inside QDs are widely known to be of great potential for the thermal imaging with high operating temperature. The three dimensional carrier confinement of the QD induces the phonon bottleneck which suppresses the interaction between electrons and phonons [6.1] and thereby enables the high temperature operation of QDIPs. With low defect S-K growth mode QDs, several encouraging results have been demonstrated with operation temperatures over 200K [6.2-6.3] and even up to room temperature [6.4-6.5]. However, the detection wavelengths of these devices are out of the LWIR atmospheric transmission window.

In order to fit the detection band into the LWIR window, many efforts have been focused on the dots-in-a-well (DWELL) structure [6.6-6.10]. The additional quantum well relaxes the limitation due to the QD formation process and provides the possibility to tailor the detection wavelength. More than that, the QDIPs made with the DWELL structures have an additional advantage of lower dark current due to the lower ground state energy. In particular, 640×512 large format LWIR DWELL QDIP focal plane arrays have been demonstrated recently [6.11]. Nevertheless, conventional DWELL QDIPs suffer from their inherently lower quantum efficiency. This is a primary drawback since the poor quantum efficiency of QDIPs has always been a concern during the development of the device. With the introduced InGaAs quantum well, the excited state wavefunction spreads out to the well region so that the oscillation strength of the infrared response is reduced. Besides, the photoexcited electrons in the DWELL QDIPs have lower energy relative to the GaAs barrier, making the extraction of photoelectrons more difficult.

In order to solve these problems, in the last chapter, we have developed a new DWELL structure to enhance both the oscillation strength and the escape probability of the electrons. A

thin $Al_{0.3}Ga_{0.7}As$ layer is inserted on top of the InAs QDs in the DWELL structure to provide better confinement for the excited state wavefunction in the QD region and also elevates the excited state energy. The overall quantum efficiency was therefore enhanced by over 20 times. In this chapter, we further improve such confinement-enhanced DWELL (CE-DWELL) detectors by optimizing the device structure. With our improved CE-DWELL design, LWIR QDIPs with operating temperature over 200K is achieved for the first time.

In the following, the device characteristics of CE-DWELL QDIPs at different temperatures will be discussed in detail first. Then, two samples with different thicknesses of the $Al_{0.3}Ga_{0.7}As$ CE-layers will be compared at different temperatures to study the device performance. Thick AlGaAs layers can elevate the dark current activation energy so that the device, although unfavorable for low temperature operations, shows much better performance at higher temperatures. Finally, the samples with $Al_{0.2}Ga_{0.8}As$ and with $Al_{0.3}Ga_{0.7}As$ CE-layers will be also compared. $Al_{0.3}Ga_{0.7}As$ CE-layers give more concentrated electron wavefunctions so that the device reveals higher quantum efficiency and thereby higher detectivity.

6.2 Detailed Device Characterization for CE-DWELL QDIPs

The CE-DWELL sample (RN0157) investigated in this section has the structure as shown in Fig. 6.1(a). Compared with the samples described in chapter 5, thicker GaAs barrier layers were purposely grown. The thicker GaAs barriers can provide longer acceleration path for conductive carriers to enhance the current gain and thereby the responsivity [6.3]. Besides, the strain energy accumulated in the active region due to In(Ga)As layers is reduced which is favorable for a better epitaxial quality. 2.4 MLs of InAs QDs (510°C, 0.1 μm/hr) were deposited on a 2 nm $In_{0.15}Ga_{0.85}As$ layer and covered by 2nm $Al_{0.3}Ga_{0.7}As$/4nm $In_{0.15}Ga_{0.85}As$ structure to comprise the CE-DWELL unit. δ-doped Si layers with a concentration of $2x10^{10}$ cm^{-2} were used to provide a doping density ~$1e^{-}$/dot. Fig. 6.1(b) shows the 3-D AFM image of

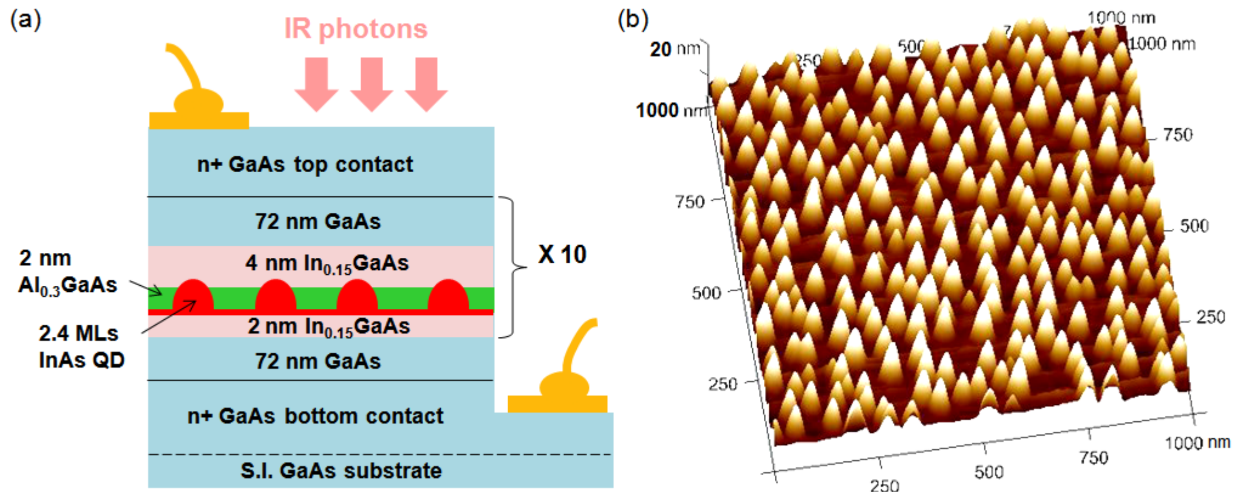

Fig. 6.1 (a) The schematic diagram of the CE-DWELL QDIP and (b) the 3-D AFM image of the sample.

the sample. The QD density is determined to be about $2.6\text{x}10^{10}$ cm^{-2}, which is slightly higher than for the previous sample due to the increased InAs MLs. The measured uncapped dot size is about 13-17 nm for the height and about 40-55 nm for the base length.

Figure 6.2(a) shows the 77K PL spectra of the sample with two different excitation powers. The low power spectrum reveals a single peak with FWHM of 51meV, showing a well controlled QD distribution for the sample. The high power spectrum, because of state filling, additionally generates four well-resolved excited-state peaks as well as a 2-D state peak. With such a confined-state distribution, LWIR photocurrent response is achieved as shown in Fig. 6.2(b). A strong response peak at 8.2 μm with the responsivity reaching 0.33 A/W is obtained at

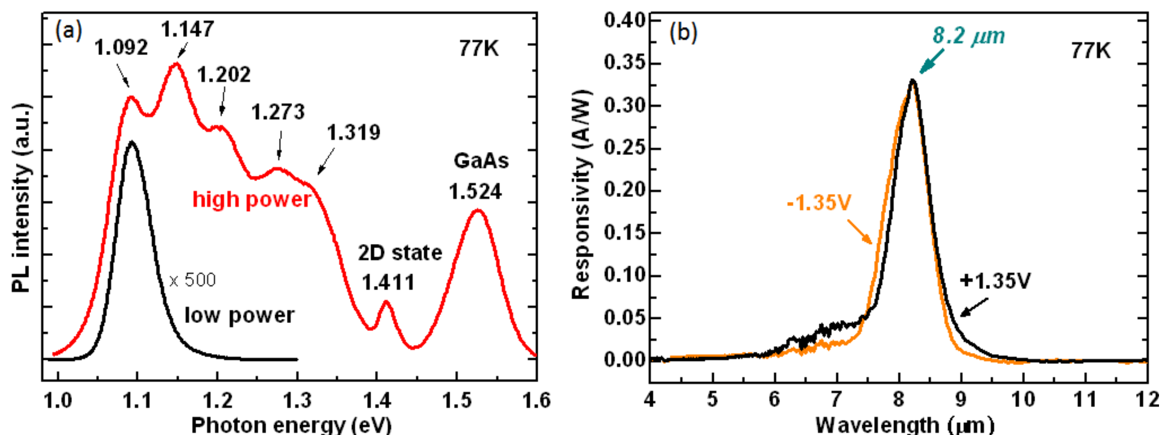

Fig. 6.2 (a) The PL spectra with different excitation powers and (b) the photocurrent spectra of the sample.

±1.35V and 77K. Given that $\Delta E_c : \Delta E_v \fallingdotseq 2:1$, the response peak corresponds to the transition between the ground state (1.092eV) and the 4th excited state (1.319eV) of the QDs (see Fig. 6.2(a)). The narrow relative bandwidth ($\Delta\lambda/\lambda_p$) of 10% also agrees with this B-B type transition. The nearly unchanged spectral shape under different bias polarities suggests that the QDs' confinement barrier scheme is basically symmetric along z-direction.

Not only for different bias conditions, the photocurrent spectra have similar shapes also for different temperatures, as shown in Fig. 6.3. However, the situation is quite different for the

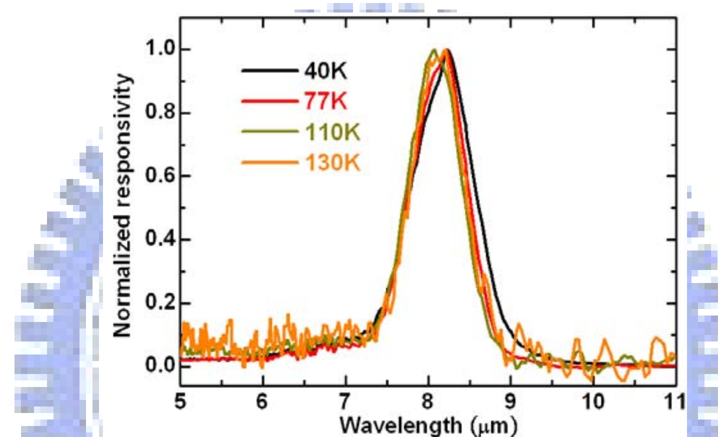

Fig. 6.3 Photocurrent spectra of the sample at different temperatures.

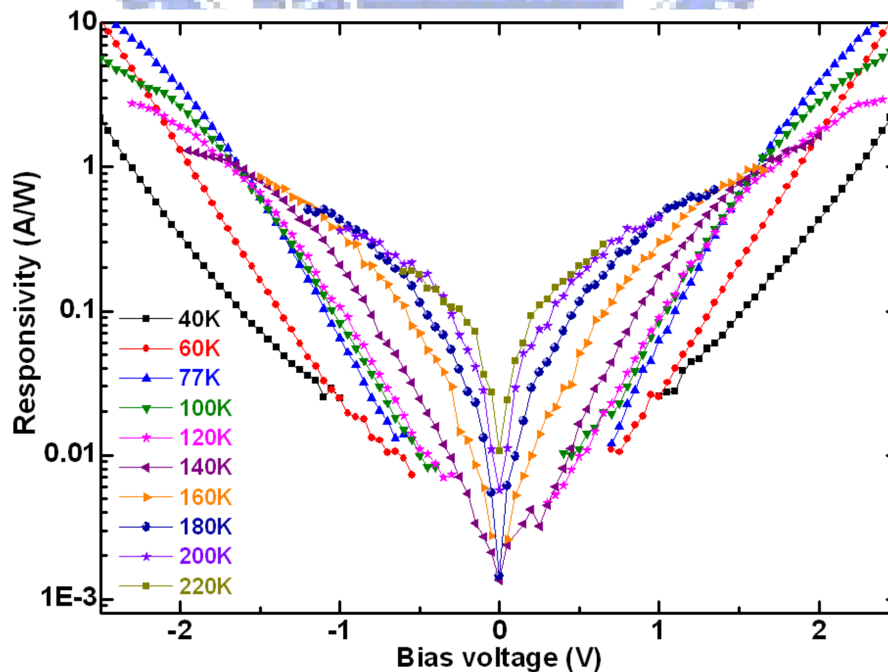

Fig. 6.4 Voltage dependence of responsivity of the sample at different temperatures.

absolute responsivity. Fig. 6.4 shows the responsivity of the sample at different biases and temperatures. The responsivity increases exponentially with voltage. As the temperature rises, the responsivity also increases dramatically from 60K to 180K and saturates after 180K (for the bias range within ±1V). Such dependence pertaining to QDIPs is quite different from what has been observed in QWIPs. In QWIPs, the responsivity keeps almost constant at different device temperatures and changes linearly with the bias voltage for B-C type devices.

In order to investigate the temperature dependence of the responsivity, the current gain and the quantum efficiency (QE) were separated from the responsivity and shown in Fig. 6.5(a) and Fig. 6.5(b) respectively. The data at lower biases with lower temperatures is not available due to the limit of noise measurement. Obviously, the current gain has a similar trend as the responsivity does. The current gain increases more than 50 times from 120K to 200K. One major difference is that the gain increases without saturation even at 220K. This shows the increase of responsivity is primarily due to the increased current gain. The increasing dark current with the temperature injects more carriers inside the QDs. The repulsive potential of the extra carriers suppresses the carrier capture process and therefore the current gain is enhanced [6.12]. On the other hand, in Fig. 6.5(b), the peak QE decreases by an order of magnitude with the increase of temperature from 77K to 220K. For such device with B-B type transitions, the

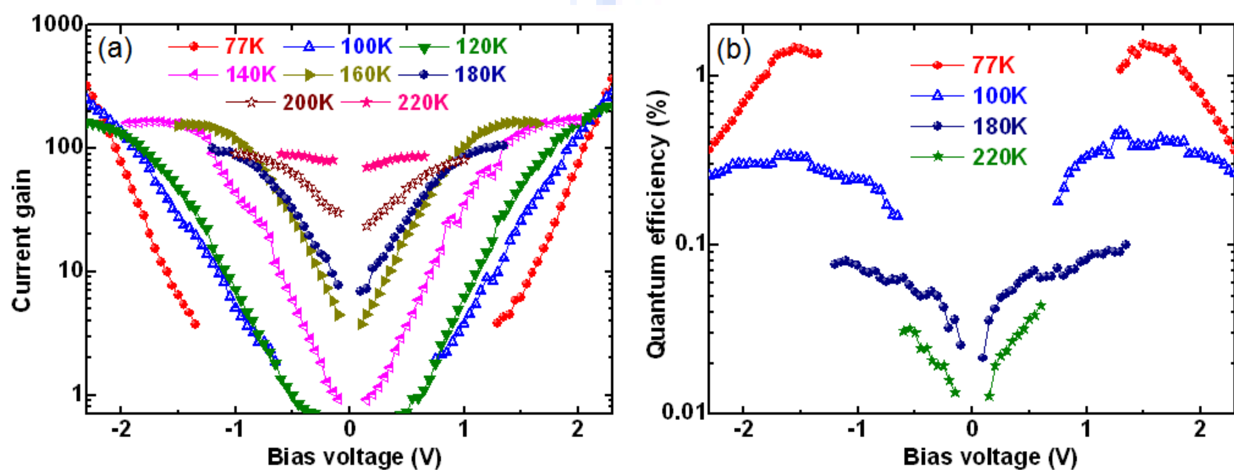

Fig. 6.5 Voltage dependence of (a) current gain and (b) quantum efficiency of the sample at different temperatures.

photoexcited carriers need additional energy to escape from potential trap before being trapped back to the ground state. At higher temperatures, however, it was found the excited electrons are more likely to be trapped in the QDs than to contribute to the photocurrent, for the relaxation rate increases faster with temperature than the escape rate [6.13]. Besides, at higher temperatures, the thermal distribution of carriers will depopulate the ground state electrons for absorption and reduce the QE. The opposite temperature dependent behaviors for the gain and the QE show that the high responsivity in QDIPs at elevated temperature originates from the excellent current gain. By the way, the current gain of this sample (3.7 at -15 kV/cm at 77K) is higher than that of the sample RN0175 (1.2 at -15 kV/cm at 77K), showing the advantage of thicker GaAs barrier for QDIPs.

Figure 6.6 shows the detectivity of the sample at different temperatures. Again, the data at lower biases with lower temperatures is absent due to the limit of our measurement system. At low temperatures, the detectivity decreases rapidly with the bias voltage. As the temperature rises, such voltage dependence gradually becomes weaker. This property is favored since the device provides wider bias range at high temperatures. At 77K, the highest detectivity is 3.6×10^{10} $cmHz^{0.5}/W$ at 1.4V. This shows the superior performance of the CE-DWELL structure. When the temperature is higher than 200K, the device still has the detectivity higher than $\sim 10^{7}$ $cmHz^{0.5}/W$. In the following, this sample will be compared with another sample with thicker

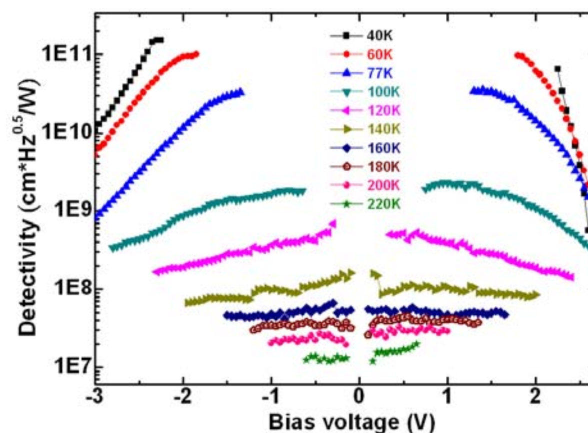

Fig. 6.6 Voltage dependence of specific detectivity of the sample at different temperatures.

AlGaAs layers in the CE-DWELL structures to study the device performance.

6.3 Comparison between the CE-DWELL detectors with thin and thick $Al_{0.3}Ga_{0.7}As$ CE-layers

The two samples compared in this section were grown with different CE-DWELL structures as shown in Fig. 6.7. While the thiner AlGaAs layer was thin enough to only cover the QD side walls, the thicker AlGaAs layer was grown to virtually cover the entire QD. Fig. 6.8 shows the TEM image of the test sample with 3 nm AlGaAs layer deposited on the InAs QDs. It confirms the coverage condition of RN0158 as shown in Fig. 6.7. The two different thicknesses of the AlGaAs layers also provide different degrees of confinement enhancement for the DWELL structure. Fig. 6.9 shows the PL spectra of the two samples at 77K. The ground state energy of the thick AlGaAs sample is 27 meV higher than that of the thin AlGaAs sample due to the better quantum confinement from the thicker AlGaAs layer. Such difference in

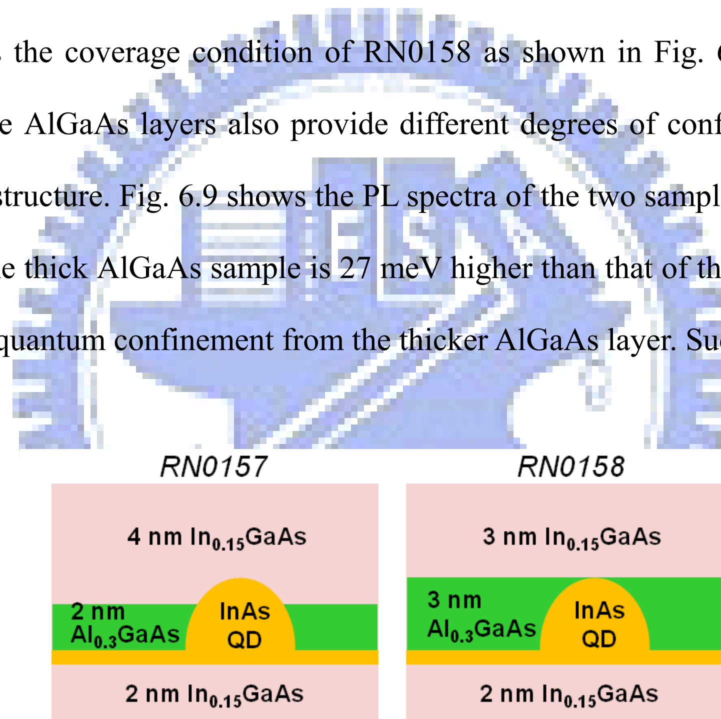

Fig. 6.7 Schematic diagram of the CE-DWELL structures with thin and thick AlGaAs CE-layers.

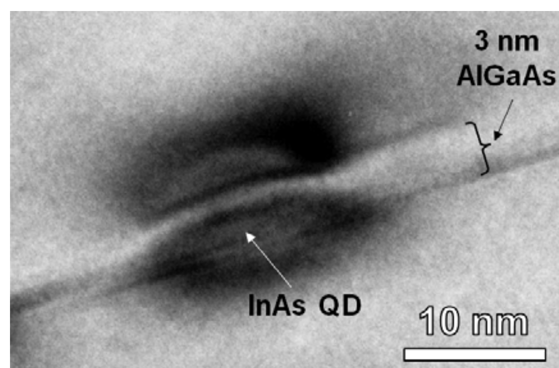

Fig. 6.8 Cross-sectional TEM image of the sample with 3 nm AlGaAs layer on the QDs.

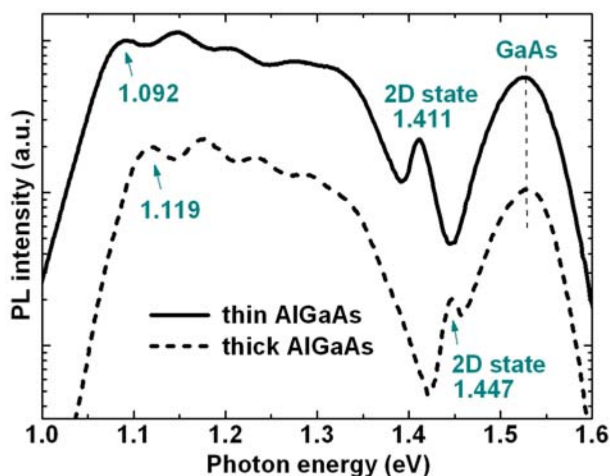

Fig. 6.9 High power PL spectra of the two samples at 77K.

confinement effect is even pronounced for the 2-D like electronic state in the structure because of a more extended wavefunction. The 2-D state has the emission energy 36 meV higher for the thick AlGaAs sample than for the thin AlGaAs sample.

Fig. 6.10 shows the photocurrent spectra of the thin AlGaAs sample and the thick AlGaAs sample as well as the bias dependent responsivity curves at 77K and 200K. Both CE-DWELL samples reveal suitable response band for LWIR detection. The response peak of the thin AlGaAs sample is at 8.2 μm, while that of the thick AlGaAs sample is slightly shorter, at about 8 μm. The thicker AlGaAs layer in the CE-DWELL structure pushed the response peak toward short wavelength as expected. Both of the spectra show small relative bandwidths ($\Delta\lambda/\lambda_p$) of about 10% with the B-B type transitions. It should be mentioned that, in the thick AlGaAs sample, the QD fully covered by the AlGaAs layer breaks the symmetry of the QD confinement in DWELL structure along z-direction. Fig. 6.11 shows the photocurrent spectra of the thick AlGaAs sample under different bias polarities. Different from the case for the thin AlGaAs sample (see Fig. 6.2(b)), the photocurrent spectrum of the thick AlGaAs sample shows different shapes for the positive and negative bias conditions. The single peak structure at negative bias split into two peaks when the bias polarity changed to be positive. Comparing the responsivity of the two samples (Fig. 6.10), the thin AlGaAs sample shows higher reponsivity

at both temperatures. At 200K, it reaches 0.37 A/W at 0.8V. Although there is a stronger confinement effect in the sample with thicker AlGaAs layers, the responsivity instead degraded. However, its responsivity (37 mA/W at -1.6V at 77K) is still higher than that of the sample without AlGaAs layers (23 mA/W for RN0176 under the same electric field), showing the advantage of the confinement-enhanced DWELL structure.

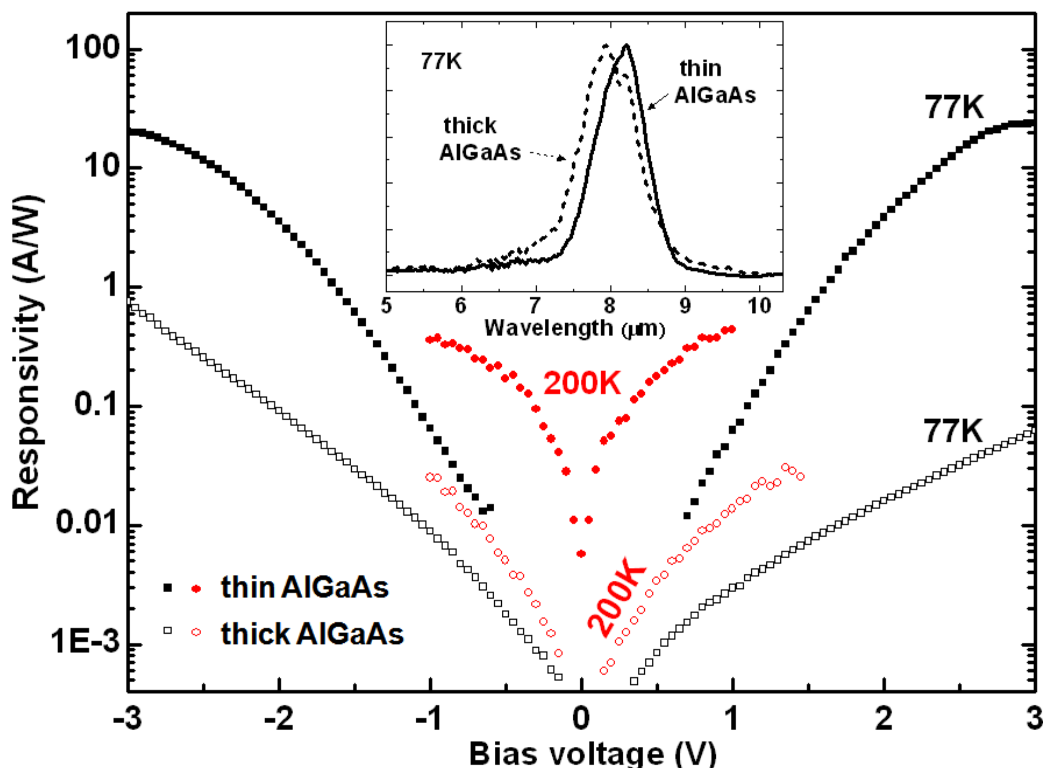

Fig. 6.10 The voltage dependence of the peak responsivity of the two samples at 77K and 200K. The inset shows the responsivity spectra of the two samples at -1.35V and 77K.

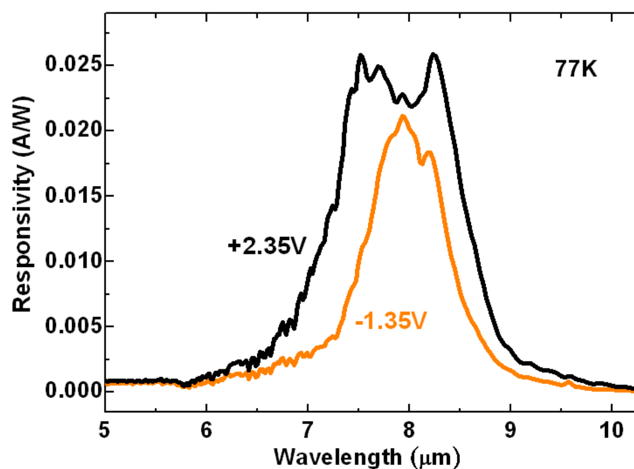

Fig. 6.11 The photocurrent spectra of the thick AlGaAs sample under positive bias and negative bias at 77K.

To understand the origin of the inferior responsivity in the thick AlGaAs device, the comparison of current gain for the two samples at 77K and 200K is shown in Fig. 6.12. Clear degradation of current gain is shown in the thick AlGaAs sample due to the thicker AlGaAs layers. Furthermore, the two samples show distinct gain behaviors. The current gain of the thick AlGaAs sample possesses a clear asymmetry between the positive bias and the negative bias. Because of thicker AlGaAs layers used, the QDs in the thick AlGaAs sample are virtually covered. When positively biased, the photo-generated electrons have to overcome the potential barrier of AlGaAs and pass through the InGaAs well. The capture probability of the excited carriers into the adjacent InGaAs well is high when the bias is low. Higher positive voltages are needed to reach the same current gain as that in the reverse bias. On the other hand, in the thin AlGaAs sample, because of thinner AlGaAs layers, the current gain is more symmetric under different bias polarities and it has a much higher gain than that of the thick AlGaAs sample under the same positive bias. The current gain difference of the two samples also depends on the device temperature. At higher temperatures, because of the additional thermal energy, the capture probability of electrons decreases in both bias polarities. The gain increases in both samples and the asymmetry reduces in the thick AlGaAs sample.

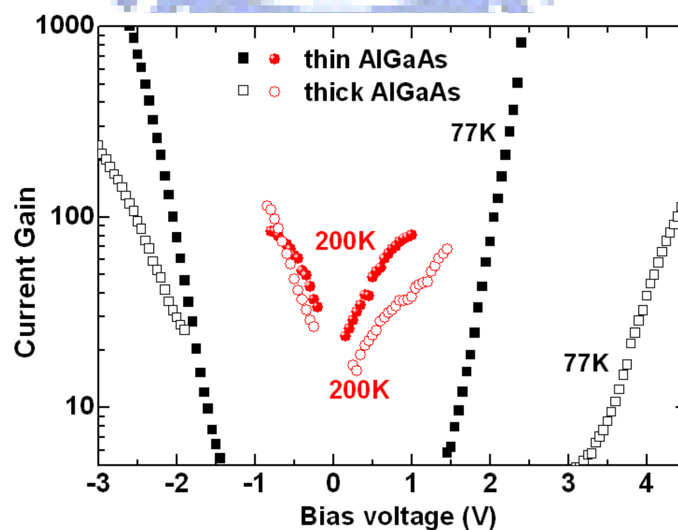

Fig. 6.12 The current gain curves of the two samples at 77K and 200K.

The decrease of responsivity in the thick AlGaAs sample cannot be only explained by the gain degradation. In fact, the QE also degraded for the thick AlGaAs sample. To further investigate the QE, the polarization-dependent photo-response of our devices was measured using the 45° edge coupling scheme. The results are shown in Fig. 6.13(a) and (b) for the two samples. The spectra changed differently for the two samples as the polarizer angle varied from 0 degree (induce mixed TM and TE response) to 90 degree (induce pure TE response). For the thin AlGaAs sample, the TE response is ~49% of the TM response. While for the thick AlGaAs sample, the TE to TM response ratio is only ~28%. A stronger absorption or higher QE is expected for the thin AlGaAs sample when the radiation is normal to the surface of the devices.

The better normal incident absorption (TE response) for the thin AlGaAs sample comes from a better lateral confinement of carriers in QDs. Because the AlGaAs barrier layer is thin enough to leave the tips of the QDs uncovered, this additional barrier is mainly in the lateral direction. This lateral confinement enhances normal incident absorption as mentioned in chapter 5. For the thick AlGaAs sample, the tips of the QDs are covered by the thick AlGaAs layer. Since the vertical confinement is also enhanced in this case, the advantage from the lateral confinement is reduced. This explains why the QE of the thin AlGaAs sample is better than that of the thick AlGaAs sample under the normal incidence configuration. This also shows the importance of having a proper AlGaAs layer thickness in the devices.

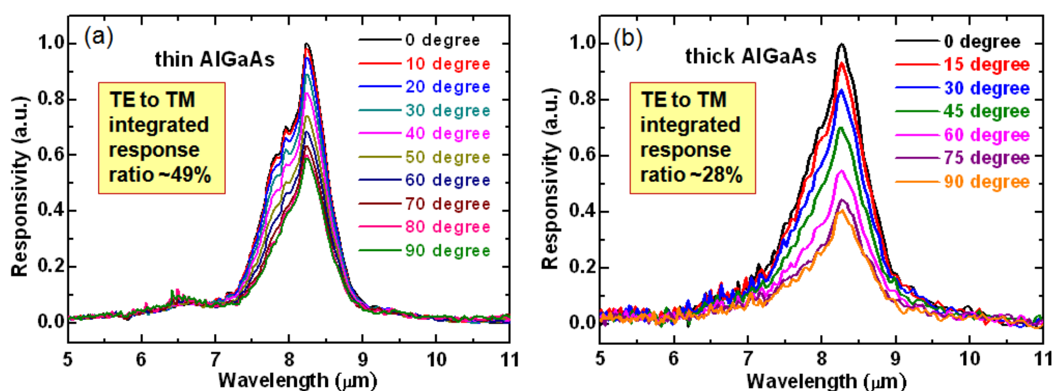

Fig. 6.13 The polarization-dependent photocurrent spectra of (a) the thin AlGaAs sample and (b) the thick AlGaAs sample at 40K under the 45° facet-coupled configuration.

The AlGaAs layer in the thick AlGaAs device, although is too thick from the responsivity point of view, is effective to reduce the dark current. This is especially true at high temperatures and low bias voltages. The dark current density for the thick AlGaAs sample and the thin AlGaAs sample are 1.4×10^{-8} A/cm^2 and 4.1×10^{-6} A/cm^2 respectively at -1V and 77K. The thicker AlGaAs layers effectively block the low energy part of the dark current, so the detectivity of the thick AlGaAs device is not necessarily worse than that of the thin AlGaAs device. Fig. 6.14 shows the specific detectivity of the two samples at different temperatures. At 77K, the highest measured detectivity for the thin AlGaAs sample is 3.6×10^{10} cmHz$^{0.5}$/W at 1.4V. However, as the temperature increases, the thick AlGaAs sample starts to show better performance. At 220K, the highest detectivity measured for the thick AlGaAs sample is 4.85×10^{7} cmHz$^{0.5}$/W at -0.15V, which is about 2.4 times higher than that of the thin AlGaAs sample. When the temperature is further raised to 240K, the detectivity reaches 1.4×10^{7} cmHz$^{0.5}$/W at -0.1V for the thick AlGaAs sample, while for the thin AlGaAs sample the dark current is too high for the measurement.

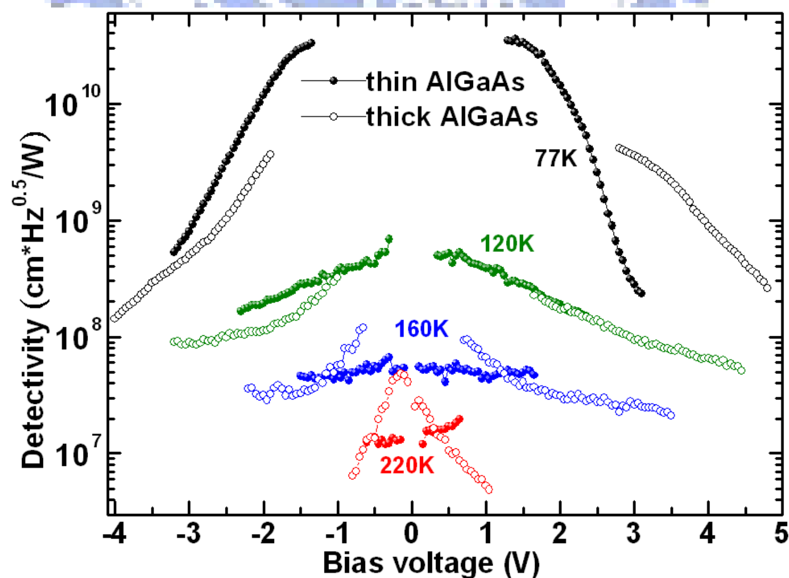

Fig. 6.14 The specific detectivity curves of the two samples at 77K, 120K, 160K and 220K.

The comparison of the two samples shows an important factor for the high temperature

operation. The thin AlGaAs sample is a typical high performance detector at 77K with good carrier collection capability. However, as the temperature increases, the superior carrier transport property induces high dark current which is not acceptable in real applications. On the other hand, although the insertion of the thicker AlGaAs layer in the thick AlGaAs sample degrades the responsivity, the dark current is suppressed even more especially at small biases. As the temperature increases, the thermal energy helps the photocarrier collection and provides a better performance at higher temperatures. This indicates the importance of the current suppression for the high operating temperature devices.

6.4 Comparison between the CE-DWELL detectors with $Al_{0.2}Ga_{0.8}As$ and with $Al_{0.3}Ga_{0.7}As$ CE-layers

In principle, to increase the Al content in AlGaAs layer for the CE-DWELL structure can increase the confinement state energies accordingly. However, the epitaxial process of the QDs makes the issue more complicated. A series of single layer CE-DWELL structure was prepared with different Al content in the AlGaAs layer ranging from 0% to 30%. Fig. 6.15 shows the PL spectra of the samples as well as the PL spectrum of the conventional DWELL structure. Surprisingly, opposite trend of the ground state energy shift is clearly shown in the figure. The sample with the weakest confinement (i.e. the sample with GaAs layer) generates the highest ground state energy. The intermixing effect during the epitaxial process dominates the behavior. As published, strong intermixing of the Ga atoms with InAs QDs is observed when the InAs QDs are covered by the GaAs layer [6.14-6.15]. With the increase of the Ga content in the QD, the ground state energy is thus raised. When the Al content in AlGaAs layer increases, the intermixing effect decreases and the ground state energy is thus lower. When the Al content is around 20%, the decrease of intermixing effect and the increase of the quantum confinement are balanced. No obvious ground state energy shift is observed when the Al content is higher than 20%.

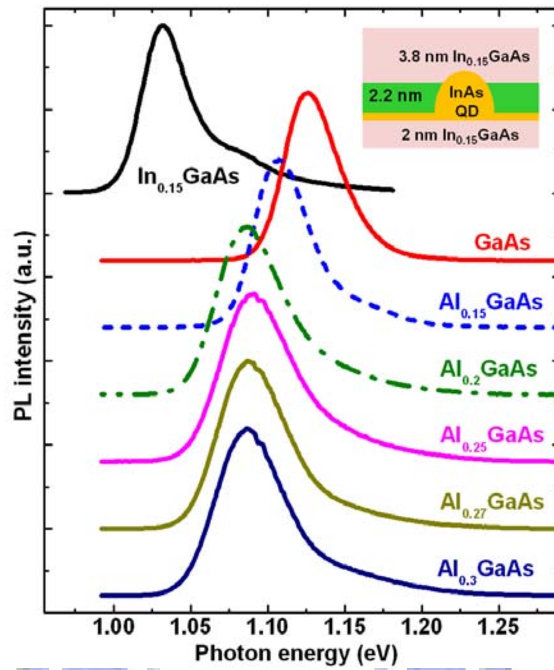

Fig. 6.15 The PL spectra of the samples with different Al content in the AlGaAs confinement enhancing layer. The PL spectrum of the conventional DWELL structure is also included.

However, the device performance can be different even though the state energies are almost the same. In principle, lower Al content (20%) is preferred from the material quality point of view, but higher Al content (30%) is preferred from the wavefunction confinement viewpoint. To find out the better solution, two device samples with $Al_{0.3}Ga_{0.7}As$ (RN0615) and $Al_{0.2}Ga_{0.8}As$ (RN0613) confinement enhancing layers were compared. Fig. 6.16(a) shows the

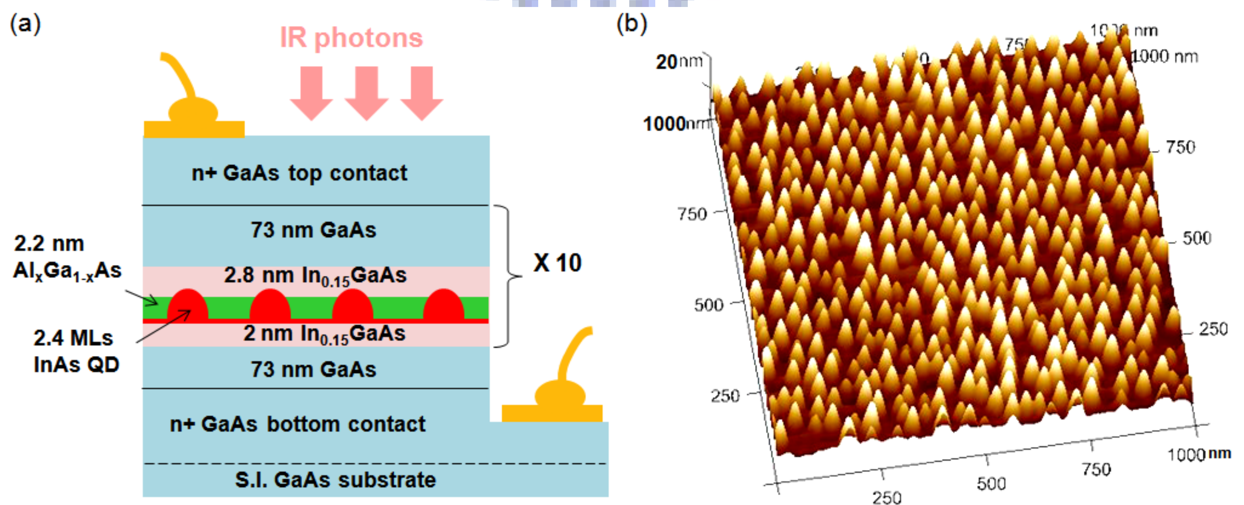

Fig. 6.16 (a) Schematic diagram of the CE-DWELL QDIPs and (b) the 3-D AFM image of the sample RN0615.

sample structure. In the two samples, the thickness of the $In_{0.15}Ga_{0.85}As$ QW above the AlGaAs layer was reduced to 2.8 nm to reduce the strain energy accumulation. Moreover, the growth temperature for QDs was lowered to 495°C to improve the QD density. Fig. 6.16(b) shows the AFM image of the sample. With the reduced growth temperature, the dot density was increased to ~$4x10^{10}$ cm^{-2}, about 1.6 times higher than for the samples in previous sections. The lower growth temperature also caused reduced In-Ga intermixing. Fig. 6.17(a) shows the high power PL spectrum of the sample (both the $Al_{0.3}Ga_{0.7}As$ sample and the $Al_{0.2}Ga_{0.8}As$ sample show very similar results). Compared with the sample in section 6.2 (see Fig. 6.2), the ground state energy for the samples here is lowered by 25 meV due to the reduced intermixing of Ga atoms with InAs QDs. More than that, with the reduced intermixing, the energy separations between QD states are also enlarged and therefore, the infrared response shifts to a shorter wavelength of 7.2 μm as shown in Fig. 6.17(b). Again, the response peak corresponds to the transition between the ground state (1.067eV) and the 4th excited state (1.324eV) of the QDs assuming that $\Delta E_c : \Delta E_v \fallingdotseq 2:1$. With the thin enough AlGaAs layer, the symmetry of the QD confinement barriers along z-direction is also preserved and the spectral shapes under different bias polarities are nearly the same (Fig. 6.17(b)).

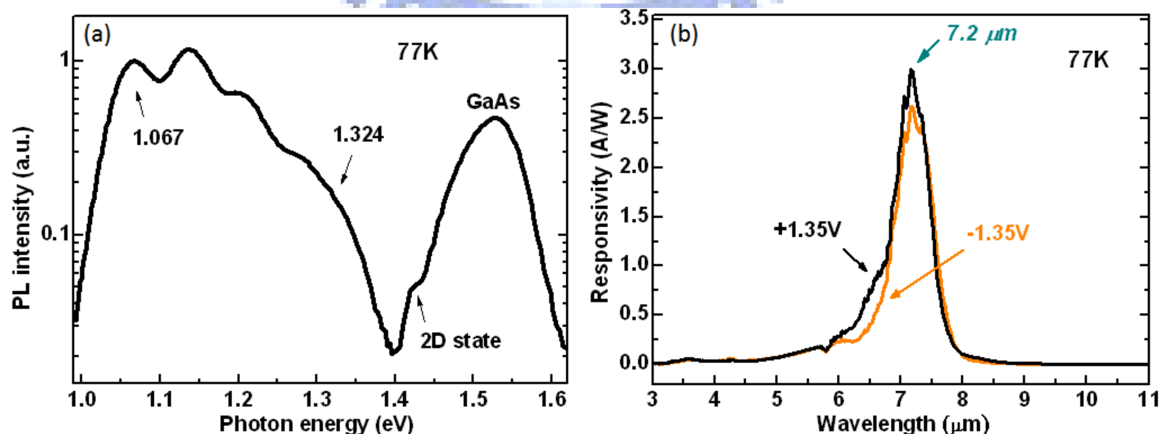

Fig. 6.17 (a) The high power PL spectrum and (b) the photocurrent spectra with different bias polarities of the sample RN0615.

Fig. 6.18 shows the responsivity curves for the two samples at 77K and 140K. It is clear seen the lower barrier of $Al_{0.2}Ga_{0.8}As$ layers does improve the responsivity due to the batter carrier transport property. At 77K and 1V, the responsivity of the $Al_{0.2}Ga_{0.8}As$ sample reaches 1.2 A/W, which is about 2.4 times higher than that of the $Al_{0.3}Ga_{0.7}As$ sample. Fig. 6.19(a) shows their comparison for the QE and the current gain. With the lower effective barrier height, the $Al_{0.2}Ga_{0.8}As$ sample indeed shows higher current gain. However, in the $Al_{0.3}Ga_{0.7}As$ sample, the suppression of the intermixing effect gives a smaller effective QD size and more concentrated electron wavefunctions. The QE is thus higher for the sample with $Al_{0.3}Ga_{0.7}As$ layers. The result also suggests that the material quality does not suffer severely for the thin enough AlGaAs layer grown on QDs even with a higher Al content. The highest QE measured

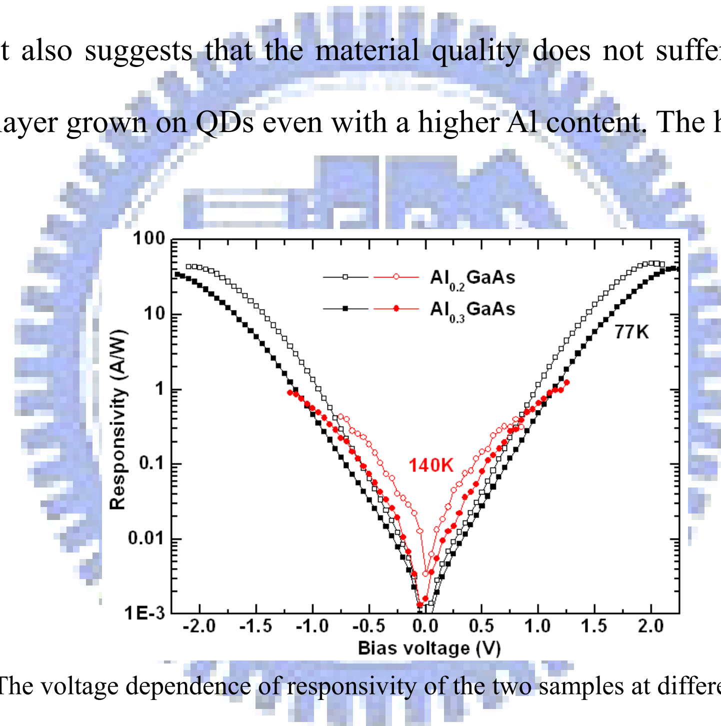

Fig. 6.18 The voltage dependence of responsivity of the two samples at different temperatures.

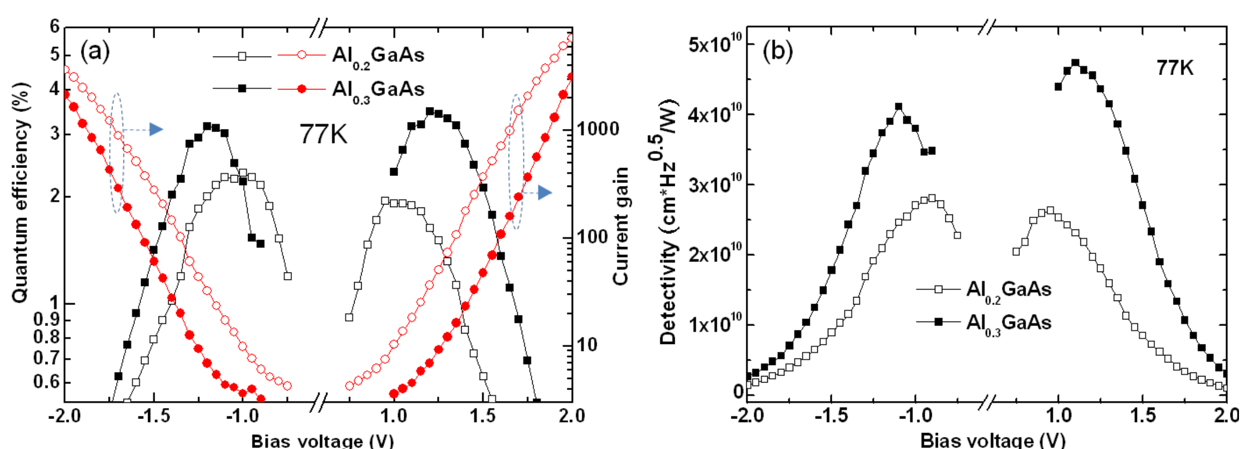

Fig. 6.19 The voltage dependence of (a) quantum efficiency, current gain and (b) detectivity of the two samples.

for the $Al_{0.3}Ga_{0.7}As$ sample is 3.5% at 1.2V and 77K, which is higher than for the previous samples due to the improved QD density. With the higher QE, combined with the lower dark current, the sample with $Al_{0.3}Ga_{0.7}As$ layers also revealed higher detectivity as expected (Fig. 6.19(b)). At 77K, the peak detectivity of the $Al_{0.3}Ga_{0.7}As$ sample is 4.7×10^{10} $cmHz^{0.5}/W$ at 1.1V, which is about 1.7 times higher than that of the $Al_{0.2}Ga_{0.8}As$ sample.

In order to further reduce the dark current and elevate the operation temperature for the device with $Al_{0.3}Ga_{0.7}As$ CE-layers, another sample with an additional 50 nm $Al_{0.25}Ga_{0.75}As$ current blocking layer [6.16] just above the bottom contact layer was also prepared (RN0614). Fig. 6.20 shows the photocurrent spectrum at 140K and the responsivity curves with different temperatures of the sample. With the inserted 50 nm $Al_{0.25}Ga_{0.75}As$ current blocking layer, the device performance at higher temperatures was indeed improved. The photocurrent spectrum measured by FTIR showed a clear signal at around 7.1 μm even at 140K. While for the sample without such blocking layer (RN0615), the spectrum can be measurement with acceptable signal quality up to only ~125K. As expected, the inserted AlGaAs layer in the device however located far from the QDs did not influence the detection wavelength much. The responsivity

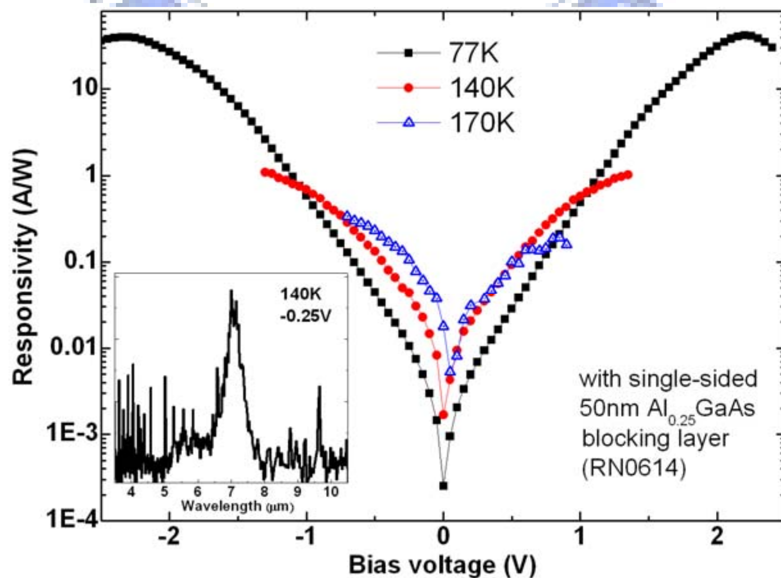

Fig. 6.20 The voltage dependence of responsivity of the sample at 77K, 140K and 170K. The photocurrent spectrum is also included in the insert.

curve can be measured up to 170K with the lock-in technique. At 170K, the responsivity curve reveals a clear asymmetric behavior for different bias polarities showing the effect of the single-sided blocking layer. At positive bias, the carrier replenishment for QDs is injected from the bottom contact and is readily hindered by the 50 nm $Al_{0.25}Ga_{0.75}As$ layer so the photo-response suffers. Fig. 6.21 shows the measured detectiviy for the sample at different temperatures. When the temperature is raised to higher than 160K, the detectivity decreases faster for the positive biases than for the negative biases due to the inferior responsivity under the positive bias condition. At 170K, the peak detectivity at the negative bias is 2.3×10^{7} $cmHz^{0.5}/W$, which is about 2 times higher than for the positive bias. However, the asymmetry in the device characteristics is not clear for the temperature lower than 140K. It is therefore expected that the device performance can be further improved by using a higher barrier current blocking layer. In this way, a more pronounced asymmetric operation condition with a higher operating temperature at the negative bias is expected.

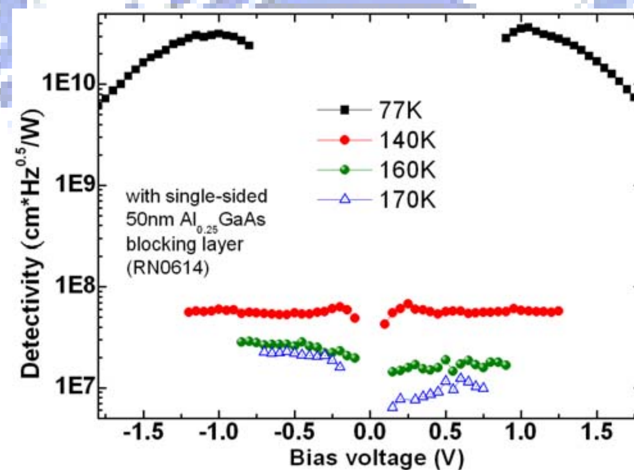

Fig. 6.21 The voltage-dependent specific detectivity of the sample at different temperatures.

6.5 Summary

In summary, we performed the detailed studies on the QDIPs with confinement-enhanced dots-in-a-well (CE-DWELL) structures. A thin AlGaAs layer was inserted on top of the QDs in the DWELL structure to enhance the wavefunction confinement and device performance. With proper device parameters, LWIR QDIPs with operation temperatures higher than 200K and detection wavelength of 8.2 μm were achieved for the first time. Two CE-DWELL structures with different thicknesses of $Al_{0.3}Ga_{0.7}As$ CE-layers were investigated. The device with thin AlGaAs layers showed much higher normal-incident absorption capability and superior 77K device performance. On the other hand, thick AlGaAs layers greatly elevate the dark current activation energy so that the device, although unfavorable for low temperature operations, showed much higher detectivity at high temperatures. To the realization of high temperature operation QDIPs, better suppression of the dark current is the key. Two other CE-DWELL detectors with $Al_{0.3}Ga_{0.7}As$ CE-layers and $Al_{0.2}Ga_{0.8}As$ CE-layers were also compared. Although the state energy distribution was nearly the same due to the balanced intermixing effect and quantum confinement effect, the device performance was very different for the two samples. The $Al_{0.3}Ga_{0.7}As$ layer provided stronger barrier confinement for the QDs and thus resulted in higher quantum efficiency for QDIPs. Although the current gain was sacrificed, the device with $Al_{0.3}Ga_{0.7}As$ layers showed a better overall performance than the device with $Al_{0.2}Ga_{0.8}As$ layers. By employing a proper current blocking layer to suppress the dark current, the device operating temperature can be further elevated.

Chapter 7

InAs/GaAs Quantum Ring Infrared Photodetectors

In this chapter, InAs quantum rings (QRs) are used as the absorption media in infrared photodetectors and the device characteristics are investigated under normal incidence configuration. Compared with QDIPs, quantum ring infrared photodetectors (QRIPs) show wider photocurrent spectra, more stable responsivity with temperature change, and lower dark current activation energy. The wide detection band comes from the transitions from the QR ground states to different excited states. The shallow confinement states generate higher dark current and enhance the carrier flow between the QRs within the same QR layer. This carrier flow partly smoothes over the repulsive potential and makes QRIPs behave similarly to QWIPs instead of QDIPs. With an $Al_{0.27}Ga_{0.73}As$ current blocking layer, the operating temperature of QRIPs is greatly raised.

7.1 Introduction

As mentioned, Infrared detectors based on intraband transitions in III-V materials are expected to be the economical alternatives to the II-VI based interband detectors for the implementation of large format imaging focal plane arrays. With this motivation, quantum well infrared photodetectors (QWIPs) and quantum dot infrared photodetectors (QDIPs), especially for the n-type devices, were widely studied with different spectral ranges in past decades [7.1-7.14]. With the intersubband transitions, the fractional spectral widths ($\Delta\lambda/\lambda$) of the photocurrent spectra are usually smaller than 30% in both QWIPs and QDIPs. However, these two kinds of detectors possess distinct characteristics because of the differing quantum confinement in their structures. In quantum wells (QWs), the electrons are confined within the

potential wells in the vertical direction but are free to move along the wells. As a result, QWIPs are only sensitive to radiations with the electric field polarized perpendicular to the quantum wells [7.2]. The current conductive gain of QWIPs is usually low and quite stable at different temperatures [7.1]. In contrast, with the three-dimensional quantum confinement for the active media, QDIPs exhibit strong in-plane polarized photo-response [7.12-7.14], much higher current gain, and strong temperature dependence of responsivity as discussed in section 6.2. With the advances in nanostructure growth, e.g. the growth of ring-like structures as described in chapter 3, it is expected that new structures with different confinement geometry will generate detectors with different properties. Recently, quantum rings (QRs) were used as the absorption media in infrared detectors and the response spectra showed wide fractional spectral widths ($\Delta\lambda/\lambda$) larger than 60% [7.15]. By exploiting the much shallower bound-state energies of the QR structure (see Fig. 3.14), Dai *et al.* demonstrated that it is easy to extend the detection band into the terahertz regime [7.16]. Quantum ring infrared photodetectors (QRIPs), therefore, provide a new approach for the long-wavelength broad-band infrared detection. However, the detailed characterization for QRIPs and their optimization have not been reported so far and the reported performance is still much worse than those of QWIPs and QDIPs.

In this chapter, the detailed characteristics of InAs/GaAs QRIPs are investigated and compared with those of QWIPs and QDIPs. Although the physical distribution of QRs is discrete and similar to those of QDs, the closely separated shallow bound states of QRs make the device perform differently from QDIPs but rather similarly to QWIPs. With a proper design and the use of an AlGaAs current blocking layer, the performance of QRIPs is greatly enhanced.

7.2 Basic characteristics of the sample

The sample used in this study contained 30 layers of InAs QRs separated by 50 nm GaAs barrier layers as the active region, which was sandwiched between two n^+ GaAs contact

layers. A 75nm $Al_{0.27}Ga_{0.73}As$ layer was added on top of the bottom contact layer as the current blocking layer [7.3]. An additional surface QR layer was also deposited for the AFM measurement. The growth procedure of the QRs began with 2.8 MLs of InAs QDs covered with 2nm of GaAs layer. Twelve second growth interruption was followed for the formation of QRs. Finally, a high growth rate GaAs layer was deposited to minimize the deformation of the as grown ring structures. A Si δ-doped layer with a concentration of 5×10^{9} cm^{-2} was inserted 2 nm under each QR layer. Fig. 7.1(a) shows the AFM image of the surface QRs. QRs with uniform sizes are clearly observed with a density around 1.8×10^{10} cm^{-2}. The average outer and inner diameters are about 60 nm and 15 nm, and the height is around 2~3 nm. The structure of the imbedded QRs was also confirmed with cross-sectional transmission electron microscopy, as shown in Fig. 7.1(b) and (c). The lateral and vertical dimensions of the imbedded QRs are very close to the AFM result obtained from QRs on the surface. The high growth rate of the capping layer effectively preserved the morphology of QRs.

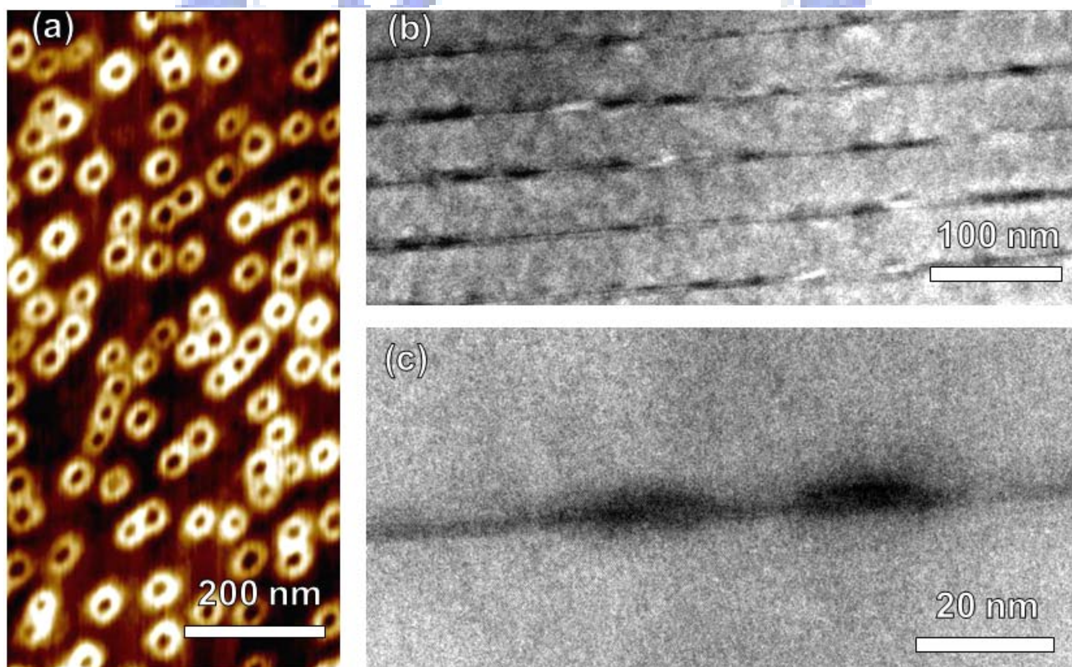

Fig. 7.1 (a) 1×0.5 μm^2 AFM image of the surface QRs. (b)(c) The cross-sectional TEM images of the imbedded QR-layers and a single imbedded QR.

The sample was then examined with the PL spectroscopy to probe the electron energy states in the QRs. Fig. 7.2 shows the 77K PL spectra with two different excitation powers. The ground state energy of the sample is 1.238eV. As mentioned in chapter 3, the ground state energy of the QRs is much higher than that of QDs with the same nominal InAs thickness due to the reduced height of the QRs. The shape of the low power spectrum is very close to a Gaussian function with a full-width-half-maximum (FWHM) of 43 meV, indicating the single size distribution and good uniformity of the QRs. Under high excitation power, four excited states and one wetting layer (WL) state were revealed. The transition energies of these excited states are at 1.290, 1.325, 1.364, and 1.40 eV, respectively. Compared with QDs, the spacing between the energy levels, however, are reduced due to the reduced center thickness and the larger lateral extent of the rings.

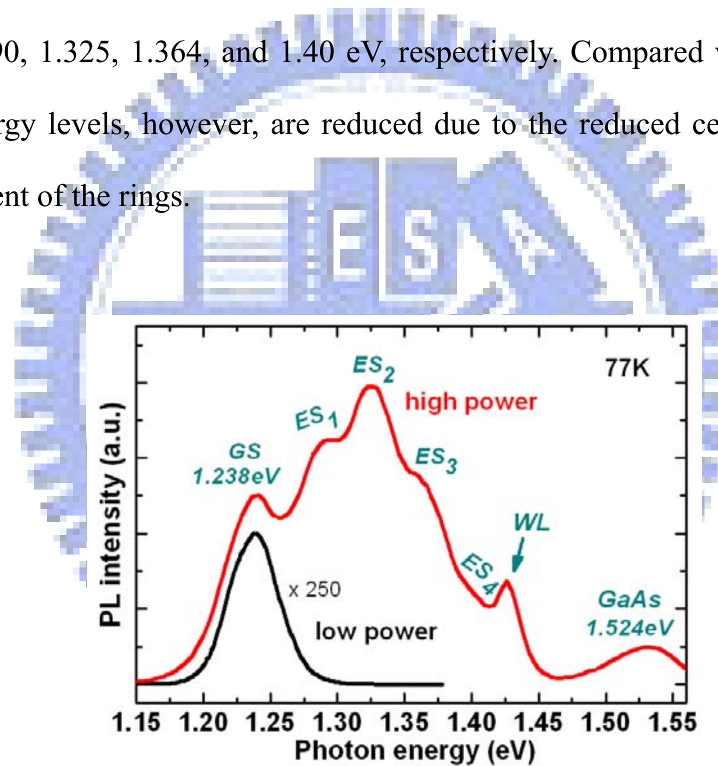

Fig. 7.2 The PL spectra of the sample at 77K with different excitation powers. The excited state peaks are indicated in the high excitation spectrum.

7.3 Investigation of the Device Characteristics

After the device fabrication, the photocurrent spectra were measured by FTIR under normal incidence configuration first. Fig. 7.3 shows the response spectra at 30K and 77K. Although QRIPs are expected to be less sensitive to the normal incident radiation due to the flattened geometry of QRs, the normal incident photocurrent signal is still strong and clear. The

polarization dependent response was further examined with the 45° edge-coupling scheme. The TE (E-field polarized in the QR plane) to TM (E-field polarized in the growth direction) response ratio of the sample was measured to be about 11% as shown in Fig. 7.4. This number, although smaller than that in QDIPs, is still stronger than that in QWIPs (see Fig. 5.4).

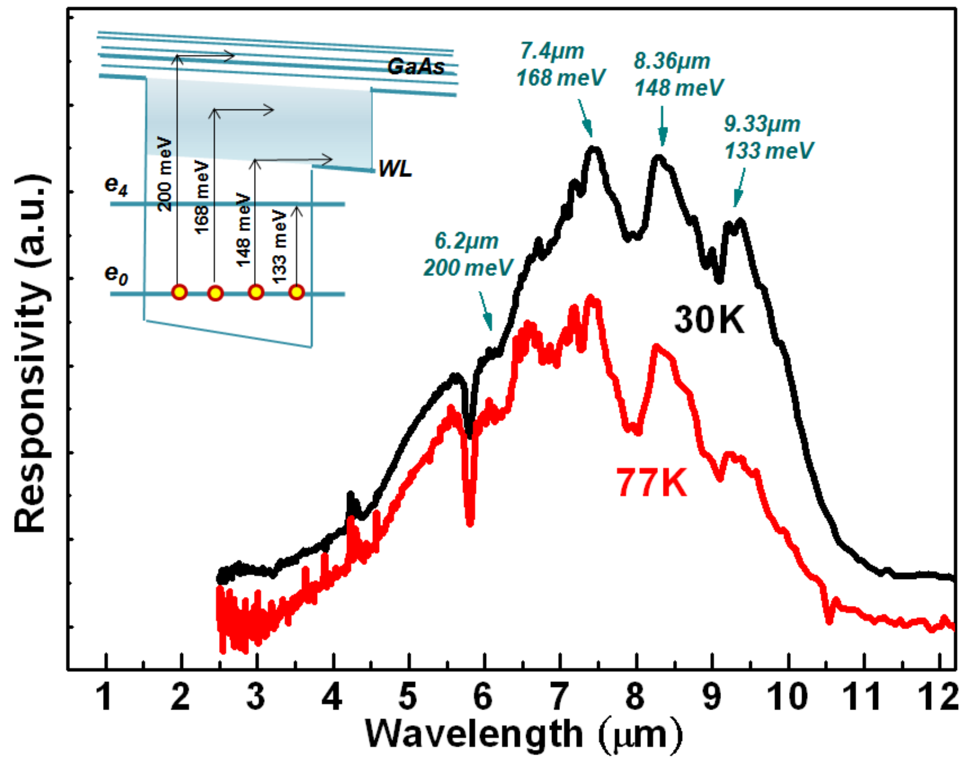

Fig. 7.3 The photocurrent spectra of the sample at 30K and 77K. The insert shows the transitions associated with the response peaks.

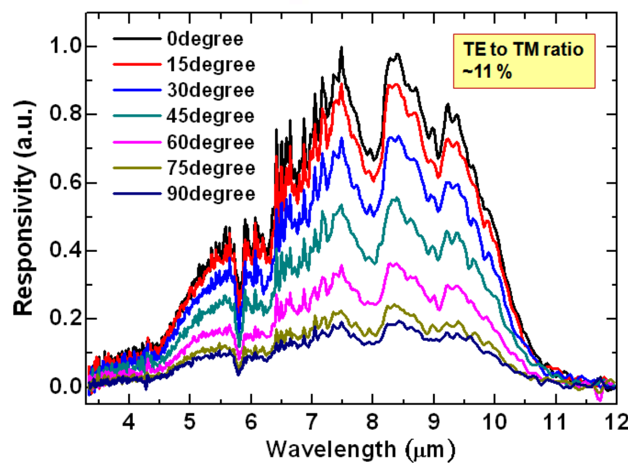

Fig. 7.4 Polarization-dependent photocurrent spectra of the sample at 22K under 45° facet-coupled configuration.

The photocurrent spectrum shows a broadband detection with the center wavelength around 8μm and a bandwidth of 5μm (Δλ/λ~60%). Unlike the single peak usually seen in QWIPs or QDIPs, multiple peaks were seen in the spectrum. From the AFM image and the PL spectrum, the QRs are quite uniform in size, indicating the wide detection band is not from the multi-modal distribution of the QRs. Instead, the multi-peak spectrum is caused by the transitions of electrons from the QR ground state to different excited states including QR bound states, WL states and GaAs continuum states. It is known that the GaAs bandgap at 77K is 1.507eV [7.17], and the WL transition energy determined by the high power PL spectrum is 1.426eV. Assuming a 7:3 ratio for the conduction/valence band discontinuity at the hetero-interface and with a given ground state energy of 1.238eV, any radiation with the photon energy higher than 188 meV will be able to excite electrons in a QR to the GaAs barrier. The broad peak around 6.2μm (200 meV) is thus from the transition from the ground state to the GaAs continuum states. The two response peaks at 7.4 μm and 8.36 μm correspond to the transitions from the ground state to the WL states. Finally, the lowest energy peak at 9.33μm is from the transition to the fourth QR excited state. The above four excitation schemes are also schematically plotted in the insert of Fig. 7.3. It might be suspected that some of the response peaks are from the first excited states to the higher states. However, those transitions will have energy lower than the peaks detected. Furthermore, the doping density used in our sample is much lower than the QR density, and the probability for electrons to populate the excited states is quite low. Finally, given that no obvious change of the response spectra at different bias levels was detected, we conclude that the responsivity peaks are unlikely to be originated from the excited states.

On the other hand, for the QDIPs with the same 2.8ML InAs QDs as in the QRIP sample, only the signal associated with the WL transition was observed (see Fig. 5.2). The quantum states in QRs are weakly confined, and the state energies are closer to the GaAs bandedge when compared with the quantum states in QDs. The ground state electron

wavefunction extends further outside of the QR region and enhances the bound to continuum transitions in QRIPs. Due to the higher states energy with respect to the GaAs bandedge, the escape probability for the transition to the QR fourth excited states is much higher in QRs. The deep bound states in QDs prohibit the generation of photocurrent from such transitions.

It is also evident in Fig. 7.3 that the responsivity spectra at 30K and 77K are slightly different at longer wavelength. The long wavelength peaks (8.36 μm and 9.33 μm) decrease from 30K to 77K while other peaks remain at the same level. As mentioned, the carriers excited to the lower energy states need more energy to escape from potential trap before being trapped back to the ground states. At higher temperatures, it was found the relaxation rate increases so much that the excited electrons are more likely to be trapped in the QRs than to contribute to the photocurrent [7.18]. Due to the lower excited state energy, this effect is more severe for the 9.33 μm peak, and it decays more than the 8.36μm peak from 30K to 77K.

The absolute responsivity was then calibrated by a 1000 ^{o}C blackbody radiation source using the lock-in technique with the chopper frequency set at 1 kHz. Due to the inserted AlGaAs layer, the responsivity is quite weak under positive biases [7.3], so the following discussions are limited to the negative biases only. The peak responsivity at different negative biases and temperatures are plotted in Fig. 7.5. The responsivity is quite stable from 40K to 100K for a wide bias range (-2.8V ~ -0.6V). This phenomenon is different from that in QDIPs, in which the responsivity usually increases over a decade in this temperature range. As discussed in section 6.2, for QDIPs, the dramatic increase in responsivity with temperature is due to the rapid increase in current gain, which is the result of the repulsive coulomb potential caused by the extra carriers inside the QDs. For QRIPs, however, the repopulation of carriers is faster within individual QR layer because of the higher ground state energy. Thus, the current gain and therefore the responsivity are more stable against temperature variation. This temperature stability is similar to that of QWIPs in which carriers flow freely in the QW plane. The fast carrier flow and the large lateral extent of the QRs with higher ground state energy

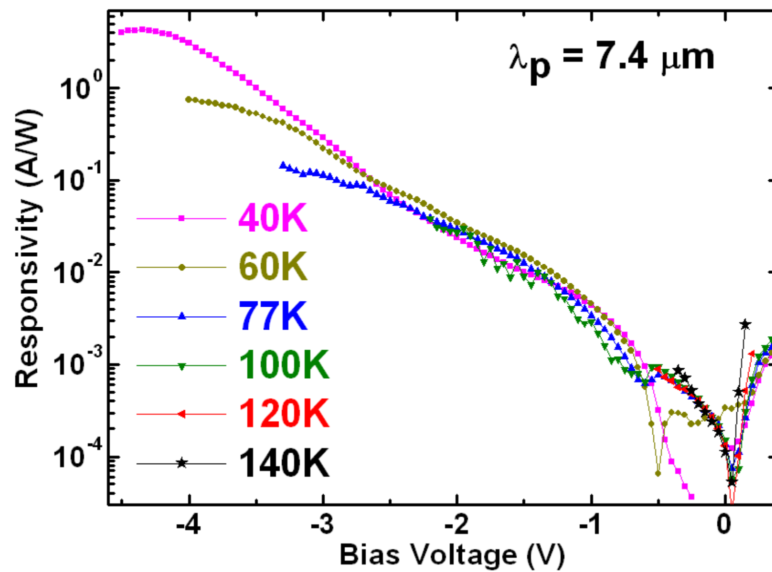

Fig. 7.5 The voltage dependence of the peak responsivity of the sample at different temperatures.

also increase the probability for the conductive free carriers being captured into the QRs. The current gain of our QRIP sample at -1V and 77K is only 0.003, which is much lower than that measured under the same conditions in QDIPs with a similar device structure. The carrier flow within the QR plane and the high capture probability of free carriers make QRIPs behave like QWIPs in the transport characteristics.

To verify the difference of the carrier flow within a QR layer and a QD layer, two samples, each with a single layer of QDs or QRs, were prepared. The same amount of InAs was used in both samples, but the QR sample had an additional partially-capping and annealing process for the ring formation. The carrier flow information could be extracted by examining the temperature dependent PL line width variation [7.19]. The PL spectra of the two samples and their FWHM as functions of temperature are compared in Fig. 7.6. As expected, the ground state energy for the QRs is higher than that of the QDs for more than 100meV. The widths of the PL spectra of the two samples both decreased first and then broadened with the increase of temperature. At extremely low temperatures, the width of the PL signal is from the non-equilibrium and random distribution of carriers in QRs or QDs, and is usually wider. With the increase of temperature, the carrier distribution will be closer to the quasi-equilibrium

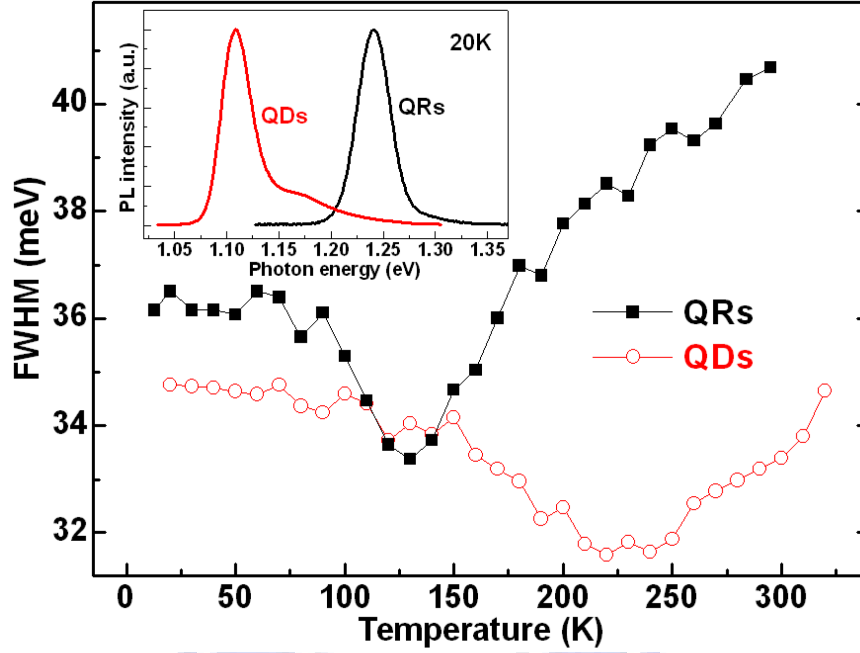

Fig. 7.6 Temperature dependent FWHM of the PL spectra of single-layer QRs (solid symbol) and single-layer QDs (unfilled symbol). The insert shows their spectra at 20K.

condition with a common Fermi level for the whole ensemble. The temperature with minimum spectral width indicates that, above this temperature (T_m), the thermal energy is high enough for carriers to flow freely between the QRs or QDs. For the QD sample, T_m was found to be around 230K. But, for the QR sample, the line width shrank much faster and T_m occurred at 130K. Such a large difference in T_m indicates that electrons within a QR layer can move more freely to repopulate the QRs. The facilitated carrier repopulation in the QR layer makes the current gain and the responsivity in QRIPs insensitive to the temperature change.

The dark current of the device was also measured at different temperatures with a helium dewar. The measured dark current curves and the extracted activation energy (Ea) are shown in Fig. 7.7. The Ea shown here was calculated assuming $I_d \propto T \exp\left(\frac{-E_a}{kT}\right)$ [7.1]. Both the dark current and Ea exhibit two distinct regions in the figure. Ea drops dramatically at a lower bias region but then decreases with a lower slope when the bias is over -0.65V. Accordingly, the dark current curves also show two different increasing rates with biases for the temperatures higher than 60K. By extrapolation, the zero bias Ea could be estimated to be in

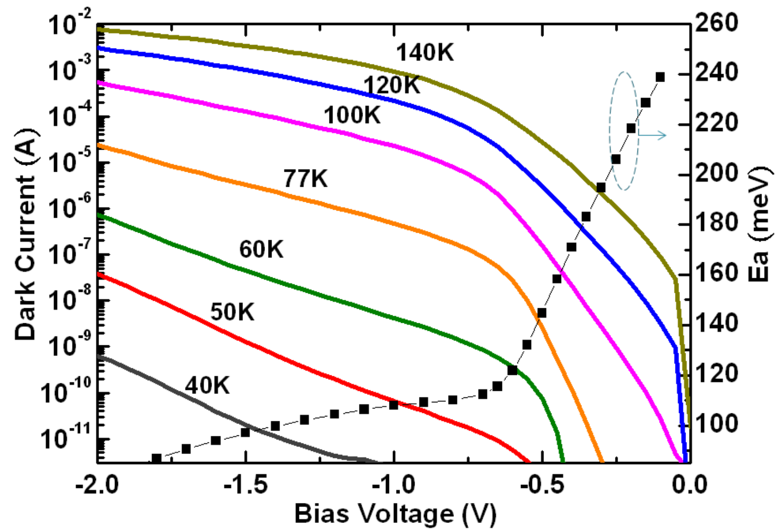

Fig. 7.7 The voltage dependence of the dark current of the sample with different temperatures and the dark current activation energies (Ea) at different bias voltages.

the range of 250~260 meV, which agrees well with the conduction band discontinuity of the $Al_{0.27}Ga_{0.73}As$/GaAs hetero-interface (256 meV [7.17]). It means that the voltage drop is essentially on the $Al_{0.27}Ga_{0.73}As$ layer from 0V to -0.65V and the dark current is limited by the wide bandgap material. When the bias further increases, the applied voltage starts to drop on the active region, and Ea is then dominated by the effective Fermi-level in the QR layer. In this domain, the activation energy at -0.7V was 112 meV, which is close to the reported activation energy for the QRIP without the AlGaAs barrier [7.15]. Such small activation energy in QRIPs prohibits high temperature operation and is the result of the higher ground state energy. Hence, the adoption of a wide bandgap layer in QRIPs is necessary for the operation at elevated temperatures.

The noise current spectra of the device were then measured and the noise current density at 1 kHz was used to calculate the specific detectivity. The result is shown in Fig. 7.8. The detectivity measured at 77K and -1V is 2.8×10^{8} $cmHz^{0.5}/W$. At 140K, the highest detectivity measured for the QRIP was 2.5×10^{7} $cmHz^{0.5}/W$ at -0.1V. In this regime, the dark current was highly suppressed by the AlGaAs layer, so the performance of the QRIP could be

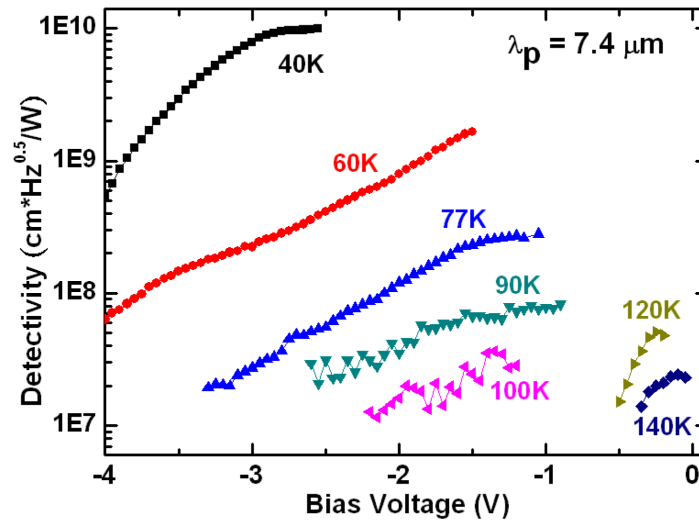

Fig. 7.8 The voltage dependence of specific detectivity of the sample at different temperatures.

measured up to 140K. It should be mentioned that the device performance measured here is based on the normal incident configuration without any grating couplers. The device performance can be enhanced with a properly designed grating coupler.

7.4 Summary

The characteristics of InAs QRIPs were investigated. The thinner InAs thickness and wider extent of the QR structure generated higher but closer electron state energies and weaker wavefunction confinement. This induces the specific features of QRIPs such as wider photocurrent spectra, more stable responsivity with temperature change, and lower dark current activation energy. The broad spectral response comes from the transitions of electrons from the QR ground state to the QR excited bound states, the WL states and the GaAs continuum states. The higher confinement state energy and the extended wavefunction in QRIPs induce better carrier flow within each QR layer as well as lower current gain. Such behaviors makes QRIPs have similar transport properties with QWIPs instead of QDIPs. For high temperature operation of QRIPs, wide bandgap layer should be inserted into the devices to compensate for the inherently small ionization energy of carriers. The performance of LWIR QRIPs was greatly enhanced with an $Al_{0.27}Ga_{0.73}As$ current blocking layer.

Chapter 8

Conclusions and Future Work

8.1 Conclusions of the Present Studies

In this dissertation, comprehensive studies on the self-assembled, zero-dimensional InAs quantum structures and the associated infrared photodetectors are presented. The primary conclusions are summarized as follows:

(1) The growth techniques to manipulate the sheet density and geometry of self-assembled InAs quantum dots (QDs) with fully *in situ* growth control were investigated. A wide range of dot densities from ~1×10^{8} cm^{-2} to ~1.2×10^{11} cm^{-2}, and the control over the geometric change from QDs, through volcano-shaped structures, to quantum rings (QRs), were achieved. The evolution level of the InAs QR formation depends on the thickness of the partial-capping GaAs layer and the annealing condition. A thinner cap layer, because of a larger interface angle, results in a larger driving force for pulling out the InAs materials from the tips of the dots and therefore more matured rings with deeper center craters. The annealing temperature and duration provide the thermal energy and time needed for the migration of InAs. By simulation, we find the formation of the ring-like potential inhibits the wavefunctions from accumulating to the ring center and therefore raises the state energies and also narrows the energy separations. With optimized growth conditions, uniform QRs with a density of 2.6×10^{10} cm^{-2} and strong room temperature PL emission are obtained.

(2) The energy spectra of self-assembled InAs QDs were investigated using the selective excitation PL technique. The dependence of the emission spectra on the excitation energy provides important information about the carrier relaxation mechanism. Three distinct regions can be identified as associated with changes in the excitation energy. At high excitation energies, all QDs are excited and participate in the light emission with the help of the

continuum states. At low excitation energies, the absence of the continuum states is such that the carrier relaxation is restricted to a multi-LO phonon process. At medium energy, the QDs are resonantly excited through discrete electronic states, but the relaxation of the carriers does not need to meet the multi-phonon resonance condition with the help of a continuum tail. For these resonantly excited electron-hole pairs, intra-dot electron-hole scattering provides an efficient channel for the release of energy via the continuous states of either electrons or holes.

(3) Quantum dot infrared photodetectors (QDIPs) with different confinement barrier schemes for InAs QDs were investigated. Compared with the simple QD structure, the InAs/ $In_{0.15}Ga_{0.85}As$ dots-in-a-well (DWELL) structure pushes the detection band to a longer wavelength to meet the 8-12 μm atmospheric transmission window and enhances the TE absorption due to the reduced QD confinement in the vertical direction. By means of inserting a thin AlGaAs layer on top of the InAs QDs in the DWELL structure, we design a new confinement-enhanced DWELL (CE-DWELL) structure which further enhances the TE absorption by about 2 times due to the enhanced lateral confinement of the QDs. More importantly, due to the enhanced oscillator strength and the increased escape probability of photo-excited electrons, the quantum efficiency increases more than 20 times and the detectivity is an order of magnitude higher at 77K. By tailoring the confinement schemes for QDs, one can effectively change the device characteristics of QDIPs to fit different application requirements.

(4) The device parameters of the CE-DWELL QDIPs were further investigated to enhance the device performance. The thickness and Al content of the AlGaAs insertion layers influence much not only the absorption property but also the transport property of the device. The device with thinner $Al_{0.3}Ga_{0.7}As$ layers possesses stronger normal-incident absorption and higher responsivity, while the device with thicker $Al_{0.3}Ga_{0.7}As$ layers possesses better suppression of the dark current and is more suitable for the high temperature operations. Furthermore, compared with the $Al_{0.2}Ga_{0.8}As$ layer, the $Al_{0.3}Ga_{0.7}As$ layer provides stronger

barrier confinement and causes less In-Ga intermixing for the InAs QDs and thereby generates better performance of the device. With appropriate device parameters of CE-DWELL, it is possible to achieve high quantum efficiency, high operating temperature, and 8-12 μm LWIR detection at the same time.

(5) Quantum ring infrared photodetectors (QRIPs) with the broadband, LWIR detection were investigated. The thinner InAs thickness and wider extent of the QR structure generates higher but closer electron state energies and weaker wavefunction confinement. This induces the specific features of QRIPs such as wider photocurrent spectra, more stable responsivity with temperature change, and lower dark current activation energy. The broad spectral response comes from both the bound-to-bound and the bound-to-continuum transitions. The higher confinement state energy and the extended wavefunction in QRIPs induce better carrier capture into and carrier flow within each QR layer and therefore the temperature-insensitive but lower responsivity, similar to the QWIPs. In order to compensate for the inherently smaller ionization energy of carriers in QRs, an $Al_{0.27}Ga_{0.73}As$ high barrier layer is inserted into the QRIPs and the device operating temperature is effectively improved.

8.2 Future Work

In order to successfully accomplish the next generation optoelectronic technologies, epitaxy techniques to *in situ* growth semiconductor zero-dimensional quantum structures should be continuously promoted, especially for improving the uniformity and epitaxial quality of the quantum objects. In our work, the MBE based growth techniques of self-assembled InAs QDs and QRs have been carefully studied. However, the control over the desired size and density should be further improved. QDs with very low density (~10^8 cm^{-2}) and large enough size (dot height ≧ 5nm) are important for the single QD studies and also the precondition for the more advanced single QR studies. As mentioned in section 3.3, the reproducibility of the segmental indium flux growth QDs is unfortunately not good. More efforts to obtain

well-controlled growth conditions for such low-density but large-size QDs are needed. Once such QDs are reproducibly obtainable, ultra-low density quantum rings or quantum volcanos can be readily achieved using the capping/annealing technique described in section 3.4, and then the PL, PL-excitation and magnetic-PL can be performed on a single ring/volcano to study the energy spectra without inhomogeneous broadening. The possible physical changes on electronic states with the geometric change from dots to rings should be very interesting. On the other hand, for high performance QD detectors and QD lasers, high density QDs ($\geqq$ $5x10^{10}$ cm^{-2}) with appropriate dot size and epitaxial quality are definitely required. From our accumulated experience, the growth control for QDs with the density about 2-3 $x10^{10}$ cm^{-2} has been well developed. However, when it comes to the range of $5x10^{10}$ cm^{-2}, the QDs' uniformity and optical quality become hardly controlled. Moreover, severe strain energy accumulation for the growth of multi-layer, high density QDs which are needed for optoelectronic devices would be an issue. More detailed studies on growth control for the optimal QD conditions for QD devices are needed.

For infrared detectors aimed for the LWIR detection, we have developed a promising CE-DWELL structure for high performance QDIPs. It is worthwhile to further optimize the device parameters for CE-DWELL QDIPs. From the application point of view, the way to enhance the quantum efficiency (QE) is essential no matter how it is achieved. Unfortunately, the weakest point of QDIPs is exactly the poor QE. The state-of-the-art QE reported for the QDIPs with LWIR detection band is only about 5% [8.1], much lower than that commonly reached by QWIPs (20~30%). In QWIPs, the average carrier density in one well is $3x10^{11}$ cm^{-2} with 30~50 QWs in the active region. In contrary, the usual QD density is less than $5x10^{10}$ cm^{-2} and increasing the QD layer number is not trivial due to the difficulty in the strained layer epitaxy. For the QDIPs investigated by us previously, the QD density is commonly around $2.5x10^{10}$ cm^{-2} and the stacked layer number is only ten. Although dramatic improvement in QE have been achieved with our CE-DWELL design, there still exists a large space to further push

the QE by increasing both the dot density and the QD layer number. By appropriately lowering the growth temperature and increasing the deposition thickness for QDs, we have increased the dot density to ~$4x10^{10}$ cm^{-2} with good size uniformity and the device QE does increase to 3.5%, as described in section 6.4. However, because of the suppressed In-Ga intermixing, the state energy separations of the QDs were enlarged, making the detection peak shifted to a shorter wavelength of 7.2 μm. The first task should be to tune it back into the LWIR transmission window while keeping the high dot density (not less than $4x10^{10}$ cm^{-2}). The post growth annealing technique to create appropriate intermixing effect for QDs is an approach to reduce their state energy separations and also make the crystal quality better. As for the increase of QD layer number, S. Chakrabarti et al. have ever grown 70-layered devices successfully with the GaAs barrier layers grown at high temperature [8.2], indicating the possibility of achieving large number stacked QDIPs. With careful growth control, at least 40-layered devices should be achievable using our MBE system. Besides, in order to further improve the device operating temperature, a 50-80 nm single-sided AlGaAs current blocking layer with optimized Al content can be used in device to suppress the dark current. The doping profile should be also adjusted to make the electric field distribution in the active region more efficient for the collection of photocarriers. We expect a normal incidence LWIR QDIP with a quantum efficiency of over 15% and a specific detectivity of over $2x10^{11}$ $cmHz^{0.5}/W$ at 77K would be achieved after the aforementioned device optimizations. With the optimized device structure, we also plan to develop the imaging focal plane arrays (FPAs). With the collaboration with Chunghwa Telecom Ltd, we plan to develop 640x480 pixels LWIR QDIP FPAs to demonstrate the advantage of CE-DWELL QDIPs.

Reference

[1.1] P. Bhattacharya. *Semiconductor optoelectronic devices,* Prentice-Hall, Inc., New Jersey (1997).

[1.2] D. Dragoman, M. Dragoman, *Advanced optoelectronic devices,* Springer, New York (1999).

[1.3] N. N. Ledentsov, M. Grundmann, F. Heinrichsdorff, *et al.*, *IEEE J. Sel. Top. Quant.* **6(3),** 439 (2000)

[1.4] Garnett W. Bryant, *Phys. Rev. B,* **37,** 8763 (1988)

[1.5] E. Towe, D. Pan, *IEEE J. Sel. Top. Quant.* **6(3),** 408 (2000)

[1.6] L. C. West and S. J. Eglash, *Appl. Phys. Lett*. **46,** 1156 (1985)

[1.7] B. F. Levine, *J. Appl. Phys.* **74,** R1 (1993)

[1.8] D. Pan, E. Towe, S. Kennerly, *Appl. Phys. Lett*. **73,** 1937 (1998)

[1.9] J. Phillips, *J. Appl. Phys.* **91,** 4590 (2002)

[1.10] S. D. Gunapala, S. V. Bandara, J. K. Liu, *et al.*, *Infrared Physics & Technology* **50,** 217 (2007)

[1.11] S. D. Gunapala, S.V. Bandara, *et al.*, *IEEE J. Quantum Elect.* **43(3),** 230 (2007)

[2.1] E. H. C. Parker, *The Technology and Physics of Molecular Beam Epitaxy*, London, England (1985)

[2.2] K. Y. Cheng *Proceedings of the IEEE*, **85(11),** 1694 (1997)

[2.3] C. T. Foxon, *J. Vac. Sci. Technol. B*, **1(2),** 293 (1983)

[2.4] P. A. Zhdan, *Surf. Interface Anal.* **33,** 879 (2002)

[2.5] S. Perkowitz, *Optical Characterization of Semiconductors: Infrared, Raman, and Photoluminescence Spectroscopy*, Academic Press, New York (1993)

[2.6] D. B. Williams and C. B. Carter, *Transmission electron microscopy*, Springer (1996)

[2.7] J. D. Vincent, *Fundamentals of Infrared Detector Operation and Testing*, New York, John Wiley (1990)

[2.8] C. Y. Chen and C. H. Kuan, *IEEE Transactions on Instrumentation and Measurement*, **49(1),** 77 (2000)

[2.9] W. A. Beck, *Appl. Phys. Lett.* **63,** 3589 (1993)

[2.10] B. Xing, H. C. Liu, P. H. Wilson, *et al.*, *J. Appl. Phys.* **76,** 1889 (1994)

[2.11] H. Schneider, *Appl. Phys. Lett.* **82,** 4376 (2003)

[3.1] K. Kash, A. Scherer, J. M. Worlock, *et al.*, *Appl. Phys. Lett.,* **49,** 1043 (1986)

[3.2] L. Goldstein, F. Glas, J. Y. Marzin, *et al.*, *Appl. Phys. Lett.,* **47,** 1099 (1985)

[3.3] W. Seifert, N. Carlsson, M. Miller, *et al.*, *Prog. Crystal Growth and Charact.*, **33,** 423 (1996)

[3.4] C. W. Snyder, B. G. Orr, D. Kessler, L. M. Sander, *Phys. Rev. Lett.*, **66,** 3032 (1991)

[3.5] D. Leonard, M. Krishnamurthy, C. M. Reaves, *et al.*, *Appl. Phys. Lett.*, **63,** 3203 (1993)

[3.6] D. Leonard, M. Krishnamurthy, S. Fafard, *et al.*, *J. Vac. Sci. Technol. B,* **12(2),** 1063 (1994)

[3.7] P. Chen, Q. Xie, A. Madhukar, *et al.*, *J. Vac. Sci. Technol. B*, **12(4),** 2568 (1994)

[3.8] D. Leonard, K. Pond, P. M. Petroff, *Phys. Rev. B,* **50,** 11687 (1994)

[3.9] Q. Xie, P. Chen, A. Kalburge, *et al.*, *J. Cryst. Growth,* **150,** 357 (1995)

[3.10] G. S. Solomon, J. A. Trezza, J. S. Harris, Jr., *Appl. Phys. Lett.*, **66,** 991 (1995)

[3.11] G. S. Solomon, J. A. Trezza, J. S. Harris, Jr., *Appl. Phys. Lett.*, **66,** 3161 (1995)

[3.12] J. M. Garcia, G. M. Ribeiro, K. Schmidt, *et al.*, *Appl. Phys. Lett.*, **71,** 2014 (1997)

[3.13] L. Chu, M. Arzberger, G. Bohm, G. Abstreiter, *J. Appl. Phys.*, **85,** 2355 (1999)

[3.14] S. Fafard, Z. R. Wasilewski, C. N. Allen, *et al.*, *Phys. Rev. B*, **59,** 15368 (1999)

[3.15] I. Mukhametzhanov, Z. Wei, R. Heitz, A. Madhukar, *Appl. Phys. Lett.*, **75,** 85 (1999)

[3.16] K. Nishi, H. Saito, S. Sugou, J. S. Lee, *Appl. Phys. Lett.*, **74,** 1111 (1999)

[3.17] P. Ballet, J. B. Smathers. H. Yang, *et al.*, *J. Appl. Phys.,* **90,** 481 (2001)

[3.18] R. Songmuang, S. Kiravittaya, M. Sawadsaringkarn, *et al.*, *J. Cryst. Growth*, **251,** 166 (2003)

[3.19] C. Santori, M. Pelton, G. Solomon, *et al.*, *Phys. Rev. Lett.*, **86,** 1502 (2001)

[3.20] N. N. Ledentsov, M. Grundmann, F. Heinrichsdorff, *et al.*, *IEEE J. Sel. Top. Quant.* **6(3),** 439 (2000)

[3.21] T. E. Vandervelde, M. C. Lenz, *et al.*, *IEEE J. Sel. Top. Quant*. **14(4),** 1150 (2008)

[3.22] L. Wendler, V. M. Fomin, A. A. Krokhin, *Phys. Rev. B,* **50,** 4642 (1994)

[3.23] A. Lorke, R. J. Luyken, A. O. Govorov, *et al.*, *Phys. Rev. Lett.,* **84,** 2223 (2000)

[3.24] A. Fuhrer, S. Luscher, T. Ihn, *et al.*, *Nature,* **413,** 822 (2001)

[3.25] M. Grochol, F. Grosse, R. Zimmermann, *Phys. Rev. B,* **74,** 115416 (2006)

[3.26] V. M. Fomin, V. N. Gladilin, S. N. Klimin, *et al.*, *Phys. Rev. B*, **76,** 235320 (2007)

[3.27] N. A. J. M. Kleemans, I. M. A. Bominaar-Silkens, V. M. Fomin, *et al.*, *Phys. Rev. Lett.,* **99,** 146808 (2007)

[3.28] A. Lorke, R. J. Luyken, J. M. Garcia, *et al.*, *Jpn. J. Appl. Phys., part 1* **40,** 1857 (2001)

[3.29] R. Blossey, A. Lorke, *Phys. Rev. E,* **65,** 021603 (2002)

[3.30] A. Lorke, R. Blossey, J. M. Garcia, *et al.*, *Mater. Sci. Eng. B,* **88,** 225 (2002)

[3.31] D. Granados, J. M. Garcia, *Appl. Phys. Lett.,* **82,** 2401 (2003)

[3.32] D. Granados, J. M. Garcia, *J. Cryst. Growth,* **251,** 213 (2003)

[3.33] J. Cui, Q. He, X. M. Jiang, *et al.*, *Appl. Phys. Lett.*, **83,** 2907 (2003)

[3.34] T. Raz, D. Ritter, G. Bahir, *Appl. Phys. Lett.*, **82,** 1706 (2003)

[3.35] B. C. Lee, C. P. Lee, *Nanotechnol.,* **15,** 848 (2004)

[3.36] D. Granados, J. M. Garcia, T. Ben, S. I. Molina, *Appl. Phys. Lett.*, **86,** 071918 (2005)

[3.37] K. Potschke, L. Muller-Kirsch, R. Heitz, *et al.*, *Physica E*, **21,** 606 (2004)

[3.38] S. I. Jung, H. Y. Yeo, I. Yun, *et al.*, *Physica E*, **33,** 280 (2006)

[3.39] Albert-Laszlo Barabasi, *Appl. Phys. Lett.*, **70,** 2565 (1997)

[3.40] D. J. Bottomley, *J. Vac. Sci. Technol. B,* **17(2),** 259 (1999)

[3.41] A. Rosenauer, D. Gerthsen, D. Van Dyck, *et al.*, *Phys. Rev. B,* **64,** 245334 (2001)

[3.42] M. Bissiri, G. B. H. von Högersthal, M. Capizzi, *et al.*, *Phys. Rev. B,* **64,** 245337 (2001)

[3.43] I. Filikhin, B. Vlahovic, E. Deyneka, *J. Vac. Sci. Technol. A,* **24(4),** 1249 (2006)

[3.44] C. E. Pryor, M. E. Pistol, *Phys. Rev. B,* **72,** 205311 (2005)

[3.45] S. Raymond, S. Studenikin, A. Sachrajda, *et al.*, *Phys. Rev. Lett.*, **92,** 187402 (2004)

[4.1] T. Inoshita, H. Sakaki *Phys. Rev. B,* **56,** R4355 (1997)

[4.2] O. Verzelen, R. Ferreira, G. Bastard *Phys. Rev. B,* **62,** R4809 (2000)

[4.3] S. Hameau, J. N. Isaia, Y. Guldner, *et al.*, *Phys. Rev. B,* **65,** 085316 (2002)

[4.4] V. Preisler, T. Grange, R. Ferreira, *et al.*, *Phys. Rev. B*, **73,** 075320 (2006)

[4.5] B. Ohnesorge, M. Albrecht, J. Oshinowo, *et al.*, *Phys. Rev. B,* **54,** 11532 (1996)

[4.6] S. Fafard, D. Leonard, J. L. Merz, P. M. Petroff, *Appl. Phys. Lett*. **65,** 1388 (1994)

[4.7] Q. Xie, P. Chen, A. Kalburge, *et al.*, *J. Crys. Growth,* **150,** 357 (1995)

[4.8] K. H. Schmidt, G. M. Ribeiro, M. Oestreich, *et al.*, *Phys. Rev. B*, **54,** 11346 (1996)

[4.9] R. Heitz, O. Stier, I. Mukhametzhanov, *et al.*, *Phys. Rev. B*, **62,** 11017 (2000)

[4.10] M. Bissiri, G. Baldassarri Höger von Högersthal, M. Capizzi, *et al.*, *Phys. Rev. B,* **64,** 245337 (2001)

[4.11] S. Fafard, R. Leon, D. Leonard, *et al.*, *Phys. Rev. B,* **52,** 5752 (1995)

[4.12] M. J. Steer, D. J. Mowbray, W. R. Tribe, *et al.*, *Phys. Rev. B*, **54,** 17738 (1996)

[4.13] R. Heitz, M. Grundmann, N. N. Ledentsov, *et al.*, *Appl. Phys. Lett*. **68,** 361 (1996)

[4.14] R. Heitz, M. Veit, N. N. Ledentsov, *et al.*, *Phys. Rev. B*, **56,** 10435 (1997)

[4.15] R. Heitz, M. Veit, A. Kalburge, *et al.*, *Physica E,* **2,** 578 (1998)

[4.16] H. Benisty, C. M. Sotomayor-Torres, C. Weisbuch, *Phys. Rev. B,* **44,** 10945 (1991)

[4.17] R. Heitz, H. Born, F. Guffarth, *et al.*, *Phys. Rev. B,* **64,** 241305 (2001)

[4.18] U. Bockelmann, T. Egeler, *Phys. Rev. B*, **46,** 15574 (1992)

[4.19] T. Inoshita, H. Sakaki, *Phys. Rev. B,* **46,** 7260 (1992)

[4.20] Y. Toda, O. Moriwaki, M. Nishioka, Y. Arakawa, *Phys. Rev. Lett.* **82,** 4114 (1999)

[4.21] A. Vasanelli, R. Ferreira, G. Bastard, *Phys. Rev. Lett.* **89,** 216804 (2002)

[4.22] Al. L. Efros, V. A. Kharchenko, M. Rosen, *Solid State Commun.* **93,** 281 (1995)

[4.23] Yu. A. Pusep, G. Zanelatto, S. W. da Silva, *et al.*, *Phys. Rev. B,* **58,** R1770 (1998)

[5.1] B. F. Levine, *J. Appl. Phys.* **74,** R1 (1993)

[5.2] D. Pan, E. Towe, S. Kennerly, *Appl. Phys. Lett.* **73,** 1937 (1998)

[5.3] A. D. Stiff, S. Krishna, P. Bhattacharya, S. W. Kennerly, *IEEE J. Quantum Elect.* **37(11),** 1412 (2001)

[5.4] Z. Ye, J. C. Campbell, Z. Chen, *et al.*, *IEEE J. Quantum Elect.* **38(9),** 1234 (2002)

[5.5] S. Raghavan, D. Forman, P. Hill, *et al.*, *J. Appl. Phys.* **96,** 1036 (2004)

[5.6] S. J. Xu, S. J. Chua, T. Mei, *et al.*, *Appl. Phys. Lett.* **73,** 3153 (1998)

[5.7] N. Horighuchi, T. Futatsugi, Y. Nakata, *et al.*, *Jpn. J. Appl. Phys.* **38,** 2559 (1999)

[5.8] S. Sauvage, P. Boucaud, T. Brunhes, *et al.*, *Appl. Phys. Lett.* **78,** 2327 (2001)

[5.9] H. C. Liu, *Opto-Electron. Rev.* **11(1),** 1 (2003)

[5.10] D. Pal, L. Chen, E. Towe, *Appl. Phys. Lett.* **83,** 4634 (2003)

[5.11] S. D. Chen, Y. Y. Chen, S. C. Lee, *Appl. Phys. Lett.* **86,** 253104 (2005)

[5.12] A. Weber, O. G. Lafaye, F. H. Julien, *et al.*, *Appl. Phys. Lett.* **74,** 413 (1999)

[5.13] S. E. Schacham, G. Bahir, E. Finkman, *et al.*, *Infrared Physics & Technology,* **44,** 509 (2003)

[5.14] S. Y. Wang, S. D. Lin, H. W. Wu, C. P. Lee, *Infrared Physics & Technology,* **42,** 473 (2001)

[5.15] G. Ariyawansa, A. G. U. Perera, G. S. Raghavan, *et al.*, *IEEE Photon. Tech. Lett.* **17(5),** 1064 (2005)

[5.16] E. T. Kim, Z. Chen, A. Madhukar, *Appl. Phys. Lett.* **79,** 3341 (2001)

[5.17] E. T. Kim, A. Madhukar, Z. Ye, J. C. Campbell, *Appl. Phys. Lett.* **84,** 3277 (2004)

[5.18] X. Lu, J. Vaillancourt, M. J. Meisner, *Semicond. Sci. Technol.* **22,** 993 (2007)

[5.19] X. Lu, J. Vaillancourt, M. J. Meisner, *et al.*, *J. Phys. D: Appl. Phys.* **40,** 5878 (2007)

[5.20] R. S. Attaluri, J. Shao, K. T. Posani, *et al.*, *J. Vac. Sci. Technol. B,* **25(4),** 1186 (2007)

[5.21] R. V. Shenoi, R. S. Attaluri, *et al.*, *J. Vac. Sci. Technol. B,* **26(3),** 1136 (2008)

[5.22] S. Krishna, S. D. Gunapala, S. V. Bandara, *et al.*, *Proceedings of the IEEE* **95(9),** 1838 (2007)

[5.23] T. E. Vandervelde, M. C. Lenz, E. Varley, *et al.*, *IEEE J. Sel. Top. Quant*. **14(4),** 1150 (2008)

[5.24] Z. Y. Zhang, B. Xu, P, Jin, *et al.*, *J. Appl. Phys*. **92,** 511 (2002)

[5.25] Z. Ye, J. C. Campbell, Z. Chen, *et al.*, *J. Appl. Phys*. **92,** 4141 (2002)

[6.1] J. Urayama, T. B. Norris, J. Singh, P. Bhattacharya, *Phys. Rev. Lett*. **86,** 4930 (2001)

[6.2] L. Jiang, S. S. Li, N. T. Yeh, *et al.*, *Appl. Phys. Lett.* **82,** 1986 (2003)

[6.3] S. Chakrabarti, A. D. Stiff-Roberts, P. Bhattacharya, *et al.*, *IEEE Photon. Tech. Lett.* **16(5),** 1361 (2004)

[6.4] P. Bhattacharya, X. H. Su, S. Chakrabarti, *et al.*, *Appl. Phys. Lett.* **86,** 191106 (2005)

[6.5] H. Lim, S. Tsao, W. Zhang, M. Razeghia, *Appl. Phys. Lett.* **90,** 131112 (2007)

[6.6] E. T. Kim, Z. Chen, A. Madhukar, *Appl. Phys. Lett.* **79,** 3341 (2001)

[6.7] S. Raghavan, D. Forman, P. Hill, *et al.*, *J. Appl. Phys.* **96,** 1036 (2004)

[6.8] X. Lu, J. Vaillancourt, M. J. Meisner, A. Stintz, *J. Phys. D* **40,** 5878 (2007)

[6.9] R. S. Attaluri, J. Shao, K. T. Posani, *et al.*, *J. Vac. Sci. Technol. B* **25,** 1186 (2007)

[6.10] R. V. Shenoi, R. S. Attaluri, A. Siroya, *et al.*, *J. Vac. Sci. Technol. B* **26,** 1136 (2008)

[6.11] S. D. Gunapala, S.V. Bandara, *et al.*, *IEEE J. Quantum Elect.* **43(3),** 230 (2007)

[6.12] V. Ryzhii, I. Khmyrova, V. Mitin, *et al.*, *Appl. Phys. Lett.* **78,** 3523 (2001)

[6.13] H. Lim, W. Zhang, S. Tsao, *et al.*, *Phys. Rev. B* **72,** 085332 (2005)

[6.14] Z. Y. Zhang, B. Xu, P, Jin, *et al.*, *J. Appl. Phys.* **92,** 511 (2002)

[6.15] L. Ouattara, A. Mikkelsen, E. Lundgren *et al.*, *J. Appl. Phys.* **100,** 044320 (2006)

[6.16] A. D. Stiff, S. Krishna, *et al.*, *IEEE J. Quantum Elect.* **37(11),** 1412 (2001)

[7.1] B. F. Levine, *J. Appl. Phys.* **74,** R1 (1993)

[7.2] H. C. Liu, M. Buchanan, Z. R. Wasilewski, *Appl. Phys. Lett.* **72,** 1682 (1998)

[7.3] A. D. Stiff, S. Krishna, *et al.*, *IEEE J. Quantum Elect.* **37(11),** 1412 (2001)

[7.4] H. Lim, S. Tsao, W. Zhang, M. Razeghia, *Appl. Phys. Lett.* **90,** 131112 (2007)

[7.5] S. Chakrabarti, A. D. Stiff-Roberts, P. Bhattacharya, *et al.*, *IEEE Photon. Tech. Lett.* **16(5),** 1361 (2004)

[7.6] S. Y. Wang, S. C. Chen, S. D. Lin, C. J. Lin, C. P. Lee, *Infrared Physics & Technology* **44,** 527 (2003)

[7.7] S. Y. Wang, S. D. Lin, H. W. Wu, C. P. Lee, *Infrared Physics & Technology* **42,** 473 (2001)

[7.8] P. Aivaliotis, L. R. Wilson, E. A. Zibik, *et al.*, *Appl. Phys. Lett.* **91,** 013503 (2007)

[7.9] X. Lu, J. Vaillancourt, M. J. Meisner, *Semicond. Sci. Technol.* **22,** 993 (2007)

[7.10] E. T. Kim, A. Madhukar, Z. Ye, J. C. Campbell, *Appl. Phys. Lett.* **84,** 3277 (2004)

[7.11] D. Pan, E. Towe, S. Kennerly, *Appl. Phys. Lett.* **73,** 1937 (1998)

[7.12] D. Pal, L. Chen, E. Towe, *Appl. Phys. Lett.* **83,** 4634 (2003)

[7.13] L. Chu, A. Zrenner, G. Bohm, G. Abstreiter, *Appl. Phys. Lett.* **75,** 3599 (1999)

[7.14] S. D. Chen, Y. Y. Chen, S. C. Lee, *Appl. Phys. Lett.* **86,** 253104 (2005)

[7.15] J. H. Dai, Y. L. Lin, S. C. Lee, *IEEE Photon. Tech. Lett.* **19,** 1511 (2007)

[7.16] J. H. Dai, J. H. Lee, Y. L. Lin, S. C. Lee, *Jpn. J. Appl. Phys.* **47,** 2924 (2008)

[7.17] I. Vurgaftman, J. R. Meyer, L. R. Ram-Mohan, *J. Appl. Phys.* **89,** 5815 (2001)

[7.18] H. Lim, W. Zhang, S. Tsao, *et al.*, *Phys. Rev. B* **72,** 085332 (2005)

[7.19] C. Lobo, R. Leon, S. Marcinkevicius, *et al.*, *Phys. Rev. B* **60,** 16647 (1999)

[8.1] S. D. Gunapala, S.V. Bandara, *et al.*, *IEEE J. Quantum Elect.* **43(3),** 230 (2007)

[8.2] S. Chakrabarti, A. D. Stiff-Roberts, P. Bhattacharya, *et al.*, *IEEE Photon. Tech. Lett.* **16(5),** 1361 (2004)

Vita

Name : Hong-Shi Ling (凌鴻緒)

Date of birth : December 08, 1979

Place of birth : Kaohsiung, Taiwan, ROC

Sex : Male

Educationn :

Nation Chiao Tung University Institute of Electronics Engineering	Ph. D.	September, 2004－March, 2009
Nation Chiao Tung University Institute of Electronics Engineering	M. S.	September, 2003－June, 2004
Nation Tsing Hua University Department of Chemical Engineering	B. S.	September, 1998－June, 2003

Title of Ph. D. Dissertation :

Studies of Self-assembled InAs Quantum Dots/Rings and their Infrared Photodetectors

Publication List

[1] **H. S. Ling** and C. P. Lee, "Evolution of self-assembled InAs quantum ring formation" J. Appl. Phys. **102**, 024314 (2007)

[2] **H. S. Ling**, C. P. Lee, S. Y. Wang, M. C. Lo "Energy dependent carrier relaxation in self-assembled InAs/GaAs quantum dots" Phys. Stat. Sol. (c) **5(9),** 2709 (2008)

[3] **H. S. Ling**, S. Y. Wang, C. P. Lee, M. C. Lo, "High quantum efficiency dots-in-a-well quantum dot infrared photodetectors with AlGaAs confinement enhancing layer" Appl. Phys. Lett. **92,** 193506 (2008)

[4] **H. S. Ling**, C. P. Lee, M. C. Lo, "Energy-dependent carrier relaxation in self- assembled InAs quantum dots" J. Appl. Phys. **103**, 124311 (2008)

[5] **H. S. Ling**, S. Y. Wang, C. P. Lee, M. C. Lo, "Long-Wavelength Quantum-Dot Infrared Photodetectors With Operating Temperature Over 200K" IEEE Photon. Tech. Lett. **21(2),** 118 (2009)

[6] **H. S. Ling**, S. Y. Wang, C. P. Lee, M. C. Lo, "Characteristics of In(Ga)As Quantum ring infrared photodetectors" J. Appl. Phys. **105**, 034504 (2009)

[7] **H. S. Ling**, S. Y. Wang, C. P. Lee, M. C. Lo, "Confinement-enhanced dots-in-a-well QDIPs with operating temperature over 200K" submitted to Infrared Physics & Technology

[8] S. Y. Wang, **H. S. Ling**, M. C. Lo, C. P. Lee, "Detection wavelength and device performance tuning of InAs QDIPs with thin AlGaAs layers" submitted to Infrared Physics & Technology

[9] S. Y. Wang, M. C. Lo, H. Y. Hsiao, **H. S. Ling**, C. P. Lee, "Temperature dependent responsivity of quantum dot infrared photodetectors" Infrared Physics & Technology **50,** 166 (2007)

[10] M. C. Lo, S. Y. Wang, **H. S. Ling**, C. P. Lee, "Vertical coupled quantum dot infrared photodetectors" submitted to Appl. Phys. Lett.

[11] **H. S. Ling**, S. D. Lin, S. Y. Wang, M. C. Lo, C. P. Lee, "Selective Excitation Photoluminescence of Ultra-small Self-assembled InAs Quantum Dots" Trends in Nanotechnology 2006 International Conference, Grenoble, France (Sept. 04-08, 2006)